

# Design and Development of Dual Tuned $^{19}\text{F}$ and $^1\text{H}$ RF Birdcage Coils for Small Animal MRI at 3T

by

**Gowtham Gajawada**

A thesis submitted to the Faculty of Graduate Studies  
in partial fulfillment of the requirements for the degree of  
Masters of Science in Electrical and Computer Engineering

Department of Engineering  
Lakehead University

September 2015

## Abstract

Conventional proton ( $^1\text{H}$ ) magnetic resonance imaging (MRI) is generally insensitive to the lung due to the low tissue density and other complicating factors. On the other hand, inhaled inert fluorinated gas MRI is a promising technique for functional lung imaging, since it can visualize the distribution of the inhaled gas. To better understand and develop this novel technique, a vast number of pre-clinical animal experiments are required for validating and optimizing the radio frequency (RF) coils that are used to acquire MRI data. The simplest approach would be to use single-tuned coils (i.e. RF coils each tuned to a single resonance frequency), such that a  $^1\text{H}$  coil is used to obtain anatomical information, while a separate  $^{19}\text{F}$  coil is used to obtain functional lung information. Unfortunately, this approach also requires image registration (i.e. co-alignment of separate images) in order to combine the information from the  $^{19}\text{F}$  and  $^1\text{H}$  coils. The purpose of this thesis is to eliminate the need for image registration by developing an optimized  $^1\text{H}/^{19}\text{F}$  dual-tuned coil for rodent lung imaging and disease model investigation.

Our initial design was a coil-inside-coil (CIC) approach with geometric decoupling of the  $^1\text{H}$  and  $^{19}\text{F}$  resonators. Using the CIC approach, two independent coils are positioned concentrically with each other. The inner coil is then rotated until the position inducing the minimum voltage level is found. This method is restricted to linear mode RF coils because geometrical decoupling cannot be performed in quadrature mode due to reflection of RF power resulting in a poor signal to noise ratio (SNR).

Our next approach was to construct a single birdcage coil dual-tuned to  $^1\text{H}$ - $^{19}\text{F}$  frequencies. This was done by taking the advantage of the fact that birdcage coils inherently have two orthogonal channels that are electrically invisible to each other. Because the  $^1\text{H}$  and  $^{19}\text{F}$  nuclei have close resonant frequencies at 3T (127.74 MHz and 120.15 MHz), each channel can be tuned to be on resonance for one frequency. The coupling between the two channels was quantitatively measured and compared to geometrically decoupled coils demonstrating the differences in decoupling performances. The advantage of this coil is that it assures identical  $B_1$  field profiles for the two nuclei, and slightly increased the filling factor for  $^1\text{H}$

resulting in improved SNRs. On the other hand, the disadvantage is that because  $^1\text{H}$  and  $^{19}\text{F}$  channels are orthogonal to each other, neither can be built to operate in a quadrature mode.

In our final approach, a switch-tuned quadrature coil was built which can be switched to resonate at either the  $^1\text{H}$  or  $^{19}\text{F}$  frequencies. PIN diodes are used to actively control the switching between the two frequencies. This method enables the combination of the benefits afforded by using a quadrature coil (i.e. factor of  $\sqrt{2}$  increase in SNR) and those of the dual tuned coil (i.e. the ability to switch frequencies on the fly without having to physically change coils and move samples, animals or patients from their anatomically localized positions). Using this switch-tuned coil, quantitative lung ventilation imaging can take place investigating various new imaging pulse sequences and disease models.  $B_1$  field mapping,  $B_1$  homogeneity and the uniform distribution of the currents on both fluorine and proton channels were measured.

## **Acknowledgements**

I would first like to thank my co-supervisor Dr. Mitchell Albert for introducing me into the world of RF field and MRI. Thanks for being a great mentor throughout this journey. I would also thank my supervisor Dr. Laura Curiel for her continuing support and help though out my thesis.

I would also take this opportunity to thank Mr. Ralph Hashoian (Clinical MR Solutions) for being a mentor throughout my training. This journey wouldn't have been completed without your valuable suggestions in coil engineering.

I would reserve my words to thank Tao Li for his support though out my MSc and had a great time sharing information regarding coil engineering.

I would also thank Dr. Albert's lab members for your help with experiments and with MRI. Marcus J Couch, Alexei Ouriadov, Peter Smylie, Jennifer A. Plata all made a significant contribution to this thesis.

I would also thank Dr. Matthew Fox for training me to perform the animal preparation, and I shared a great time with him at the lab.

# Table of Contents

<b>Abstract</b> .....	<b>ii</b>
<b>Acknowledgements</b> .....	<b>iv</b>
<b>Table of Contents</b> .....	<b>v</b>
<b>List of Figures</b> .....	<b>viii</b>
<b>List of Tables</b> .....	<b>xi</b>
<b>List of Symbols</b> .....	<b>xii</b>
<b>List of Abbreviations</b> .....	<b>xiii</b>
<b>Chapter 1: Motivation and Scope</b> .....	<b>1</b>
<b>1.1 Background</b> .....	<b>1</b>
1.2 Proposal and Motivation .....	2
1.3 Scope of the Thesis.....	3
<b>Chapter 2: Background and Literature Review</b> .....	<b>5</b>
2.1 Background .....	5
2.2 Introduction to NMR .....	5
2.3 Spin Angular Momentum.....	6
2.4 Bulk Magnetization .....	7
2.5 Nuclear Magnetic Resonance .....	8
2.5.1 $T_1$ Relaxation .....	11
2.5.2 $T_2$ relaxation.....	12
2.5.3 Bloch Equations.....	13
2.6 Magnetic Resonance Imaging.....	14
2.6.1 Slice selection.....	14
2.6.2 K-space.....	15
2.7 Birdcage Coils .....	16
2.7.1 Basic Birdcage Coil Design .....	16
2.7.2 Birdcage Builder .....	18
2.8 Generation of RF Fields and Signal Reception .....	21
2.9 Resonance Circuits and Impedance Matching.....	22
2.10 Signal to Noise Ratio (SNR).....	23
2.11 Q Factor .....	24
2.12 Literature Review .....	24

<b>Chapter 3: A Linear <math>^{19}\text{F}</math> -<math>^1\text{H}</math> Double Birdcage Coil (Coil Inside Coil)</b> .....	<b>29</b>
3.1 Introduction.....	29
3.2 $^1\text{H}$ and $^{19}\text{F}$ Birdcage Coil Construction and Tuning .....	29
3.3 Decoupling and Coil Isolation .....	32
3.4 Discussion .....	32
<b>Chapter 4: A <math>^{19}\text{F}</math>-<math>^1\text{H}</math> Linear Dual Tuned Birdcage Coil</b> .....	<b>34</b>
4.1 Introduction.....	34
4.2 $^{19}\text{F}$ and $^1\text{H}$ Coil Construction .....	34
4.3 Impedance Matching .....	36
4.4 Results .....	39
4.4.1 Phantom Spectroscopic Scan Results.....	40
4.4.2 Phantom Imaging Scan Results .....	42
4.4.3 $B_1$ Field Mapping and Field Homogeneity .....	44
4.4.4 Animal <i>in vivo</i> Results.....	48
4.5 Discussion .....	49
<b>Chapter 5: A <math>^{19}\text{F}</math>-<math>^1\text{H}</math> Quadrature Dual Switch Tuned Birdcage Coil</b> .....	<b>50</b>
5.1 Introduction.....	50
5.2 Coil Construction and Switching Circuit .....	50
5.2.1 Coil Construction .....	50
5.2.2 Switching Circuit .....	54
5.3 Quadrature Mode .....	56
5.4 Impedance Matching .....	57
5.5 Results .....	59
5.5.1 Phantom Spectroscopic Scan Results.....	60
5.5.2 Phantom Imaging Scan Results .....	62
5.5.3 $B_1$ Field Mapping and Field Homogeneity .....	63
5.5.4 Comparison Between Linear Dual Tuned and Quadrature Dual Tuned .....	68
5.6 Discussion .....	70
<b>Chapter 6: Discussions</b> .....	<b>71</b>
6.1 Summary .....	71
6.2 Future Work.....	72
6.3 Conclusions.....	73
<b>References</b> .....	<b>75</b>

**Appendix: Animal Care Committee Approval .....81**

## List of Figures

Figure 2.1: Precession of the magnetization vector in static magnetic field along z-axis.

Figure 2.2: Precession of magnetization with longitudinal field  $B_0$  in rotating field.

Figure 2.3:  $T_1$  relaxation.

Figure 2.4:  $T_2$  relaxation.

Figure 2.5: The slice selection in cylindrical object, with a linear magnetic field gradient along the z-axis.

Figure 2.6: Birdcage coils in A) High Pass mode B) Low Pass mode C) Band Pass Mode.

Figure 2.7: Equivalent Circuits for birdcage coils in A) High Pass mode B) Low Pass mode C) Band Pass mode.

Figure 2.8: (a) Coil specifications are defined to build a birdcage coil.

(b) Calculated capacitance and position of the capacitors to be placed on the end ring.

(c) Calculated self-inductance and effective inductance of the coil.

Figure 2.9: Resonant equivalent circuit of a simple loop coil.

Figure 3.1: Illustration of the double birdcage coil.

Figure 3.2: Schematic of the double birdcage coil.

Figure 3.3: (a) Front view of the constructed  $^1\text{H}$ - $^{19}\text{F}$  double birdcage coil.

(b) Top view of the constructed  $^1\text{H}$ - $^{19}\text{F}$  double birdcage coil.

Figure 3.4: (a)  $S_{11}$  response for  $^{19}\text{F}$  achieved.

(b)  $S_{11}$  response for  $^1\text{H}$  achieved.

Figure 4.1: Structure of the linear dual tuned

Figure 4.2: (a) Top View (b) Front View of a  $^{19}\text{F}$  -  $^1\text{H}$  birdcage coil.

Figure 4.3: Schematic of an L-C Balun.

Figure 4.4: Schematic of a linear dual tuned birdcage coil with  $^{19}\text{F}$  and  $^1\text{H}$  channels.

Figure 4.5: (a) Smith chart represents the  $S_{11}$  and the log map represents  $S_{21}$  response for  $^1\text{H}$  at

127.74 MHz (b) Smith chart represents  $S_{11}$  and the log map  $S_{21}$  response for  $^{19}\text{F}$  at 120.15 MHz.

Figure 4.6: Two syringe phantoms filled with sulfur hexafluoride ( $\text{SF}_6$ ) and mineral oil.

Figure 4.7: The  $^{19}\text{F}$  coil calibration, showing the signal response as a function of increasing power, where the 90-degree RF pulse yields the highest possible signal.

Figure 4.8: (a) FID signal (b) Spectrum response of the coil.

Figure 4.9: (a)  $^1\text{H}$  Coronal image with Mineral oil, (b)  $^1\text{H}$  Transverse image with Mineral oil.  
(c)  $^{19}\text{F}$  Coronal image with  $\text{SF}_6$ , (d)  $^{19}\text{F}$  Transverse image with  $\text{SF}_6$ .

Figure 5.10.1: The normalized  $B_1$  for  $^{19}\text{F}$ .

Figure 4.10.2: (a)  $B_1$  map with the area of  $15 \times 15 \times 30 \text{mm}$  for  $^{19}\text{F}$ .  
(b) Histogram of the  $B_1$  of coil generated by (a).  
(c)  $B_1$  field graph for  $^{19}\text{F}$ .

Figure 5.10.3: Normalized  $B_1$  map for  $^1\text{H}$ .

Figure 5.10.4: (a)  $B_1$  map with the area of  $16 \times 16 \times 20 \text{mm}$  of  $^1\text{H}$ .  
(b) Histogram of the  $B_1$  of coil generated by (a).  
(c)  $B_1$  field graph for  $^1\text{H}$ .

Figure 5.11 : (a) First row of images represents the coronal images on  $^1\text{H}$   
and second row represents coronal images of  $^{19}\text{F}$ .  
(b) First row of images represents the transverse images on  
 $^1\text{H}$  and second row represents transverse images of  $^{19}\text{F}$ .

Figure 6.1: Structure of the quadrature coil.

Figure 6.2: Illustration circuit of the coil with the  $^{19}\text{F}$  circuits (Circuit 1,  
Circuit 2, Circuit 3, Circuit 4).

Figure 6.3: (a) Top view and (b) front view of  $^1\text{H}$ - $^{19}\text{F}$  constructed quadrature  
dual tuned birdcage coil.

Figure 6.4: Switching circuit used to switch from  $^1\text{H}$  to  $^{19}\text{F}$

Figure 6.5: (a)  $S_{21}$  response switching to  $^{19}\text{F}$  from  $^1\text{H}$  when diodes are at ON state.  
(b)  $S_{21}$  response for  $^1\text{H}$  when diodes are at OFF state.

Figure 6.6: (a) linear mode where  $B_1$  field pointing in one direction (b) Quadrature mode where  
 $B_1$  field rotating in the same direction.

Figure 6.7: Schematic of dual switch tuned birdcage coil with  $^1\text{H}$  and  $^{19}\text{F}$  channels

Figure 6.4: (a) Channel-1,  $S_{11}$  response for  $^1\text{H}$ .  
(b) Channel-2,  $S_{11}$  response for  $^1\text{H}$ .

Figure 6.4: (a) Channel-1,  $S_{11}$  response for  $^{19}\text{F}$ .  
(b) Channel-2,  $S_{11}$  response for  $^{19}\text{F}$ .

Figure 6.5: Two syringe phantoms filled with sulfur hexafluoride ( $\text{SF}_6$ ) and mineral oil.

Figure 6.6: The  $^{19}\text{F}$  coil calibration, showing the signal response as a function of increasing power,  
where the 90-degree RF pulse yields the highest possible signal.

Figure 6.7: Spectroscopic results for  $^{19}\text{F}$  using  $\text{SF}_6$ .

Figure 6.8: (a)  $^1\text{H}$  Coronal image with Mineral oil.

- (b)  $^1\text{H}$  Transverse image with Mineral oil.
- (c)  $^{19}\text{F}$  Coronal image with  $\text{SF}_6$ .
- (d)  $^{19}\text{F}$  Transverse image with  $\text{SF}_6$ .

Figure 6.9.1:  $B_1$  field map for  $^{19}\text{F}$

Figure 6.9.2: (a)  $B_1$  map with the area of 18x18x30mm of  $^{19}\text{F}$ .

- (b) Histogram of the  $B_1$  of coil generated by (a).
- (c)  $B_1$  field graph for  $^{19}\text{F}$ .

Figure 6.9.3: Normalized  $B_1$  map for  $^1\text{H}$ .

Figure 6.9.4: (a)  $B_1$  map with the area of 16x16x30 of  $^1\text{H}$ .

- (b) Histogram of the  $B_1$  of coil generated by (a).
- (c)  $B_1$  field graph for  $^1\text{H}$ .

Figure 6.10: (a) Coronal image of  $^1\text{H}$  from linear dual tuned coil.

- (b) Coronal image of  $^1\text{H}$  from quadrature dual tuned coil.

Figure 6.11: (a) Coronal image of  $^1\text{H}$  from quadrature dual tuned coil.

- (b) Coronal image of  $^1\text{H}$  from linear dual tuned coil.

## List of Tables

Table 4.1: Dimensions of the coil showing off resonance tuning.

Table 5.1:  $^{19}\text{F}$  and  $^1\text{H}$  Coil dimensions and materials.

Table 5.2: Measured impedance of  $^1\text{H}$  and  $^{19}\text{F}$ .

Table 5.3: Pulse sequence parameters used for  $^1\text{H}$  and  $^{19}\text{F}$  phantom imaging.

Table 6.1: Coil dimensions and materials.

Table 6.2:  $^{19}\text{F}$  dimensions and materials.

Table 6.3: Impedance for both the channels of  $^1\text{H}$  and  $^{19}\text{F}$ .

Table 6.4: Pulse sequence parameters used for  $^1\text{H}$  and  $^{19}\text{F}$  phantom imaging.

Table 6.5: SNR obtained from linear and quadrature dual tuned coils.

## List of Symbols

Symbol	Meaning
T	Tesla
$^{129}\text{Xe}$	Xenon -129
$^{19}\text{F}$	Fluorine -19
$^3\text{He}$	Helium - 3
$^1\text{H}$	Proton
M	Magnetization
h	Planck constant
l	Quantum number
$\gamma$	Gyromagnetic ratio
$\alpha$	Angle
g	Lande g-factor
e	Charge of an electron
$B_0$	External Static Magnetic Field
$B_1$	Excitation magnetic field
$k_B$	Boltzmann Constant
m	Mass
$T_1$	Longitudinal relaxation time
$T_2$	Transverse relaxation time
E	Electric field
J	Current density
$\Delta f$	3-db bandwidth
$\Gamma$	Reflection constant
Q	Quality factor
$\chi$	Susceptibility
$\eta_f$	Filling Factor
$\mu_0$	Permeability

## List of Abbreviations

<b>Abbreviation</b>	<b>Meaning</b>
NMR	Nuclear magnetic resonance
MRI	Magnetic resonance imaging
RF	Radio frequency
SNR	Signal to noise ratio
ROI	Region of interest
FID	Free induction decay
FOV	Field of view
PFP	Perfluoropropane
SF <sub>6</sub>	Sulfur hexafluoride
TR	Repetition time
TE	Echo time
DAM	Double angle method
SV	Single voxel

# Chapter 1

## Motivation and Scope

### 1.1 Background

MRI was developed using the phenomenon Nuclear Magnetic Resonance (NMR), which has been used for decades to study the molecular structure of chemical compounds. Purcell<sup>[1]</sup> and Bloch<sup>[2]</sup> were the first to discover NMR in 1946. MRI came in to existence in 1973 through the work of Lauterbur<sup>[3]</sup> and Mansfield<sup>[4]</sup> who were the first to use NMR signals and generate images using magnetic field gradients.

MRI is a non-invasive diagnostic imaging technique that generates images containing structural information about regions of interest in the human body. A significant limitation to this imaging tool is that several tissues and organs in the human body resist the conventional MRI technique, such as the lungs. Conventional MRI is only sensitive to hydrogen-1 (referred to as protons or  $^1\text{H}$ ) in water molecules. While imaging human lungs using conventional MRI, the NMR signal in the lung is very low due to the density of lung tissue and presence of air. This results in poor quality images because of inhomogeneous susceptibility and distorted field distribution. There is a clinical demand for better quality images to improve disease diagnosis and treatment monitoring.

In 1994, Albert et al.<sup>[5]</sup> invented a novel lung MRI technique using inhaled hyperpolarized gases ( $^3\text{He}$  and  $^{129}\text{Xe}$ ). The hyperpolarization of these noble gases is achieved using one of two techniques: spin exchange optical pumping (SEOP) with rubidium atoms or metastability exchange optical pumping (MEOP). These techniques help to improve the signal of the noble gases by a factor of up to 100,000 times. This technique proved to be much more effective than the conventional  $^1\text{H}$  imaging for obtaining high quality, informative MRI images of the lungs.

More than 30 years ago, Edwin Heidelberg and Paul Lauterbur<sup>[6]</sup> were the first to demonstrate fluorine-19 ( $^{19}\text{F}$ ) MRI using inert fluorinated gases by imaging tetrafluoromethane ( $\text{CF}_4$ ) in excised rabbit lungs. In 1998, Kuethe et al.<sup>[7]</sup> refined these techniques by imaging sulfur hexafluoride ( $\text{SF}_6$ ) and hexafluoroethane ( $\text{C}_2\text{F}_6$ ) in rat lungs.

In 2013, Couch et al. [8] and Halaweish et al. [9] demonstrated inert fluorinated gas MRI in human lungs using inhaled perfluoropropane ( $C_3F_8$  or PFP). These inert fluorinated gases are inexpensive, non-toxic and abundant. Inhaled inert fluorinated gas MRI is a promising technique for anatomical and functional lung imaging. These gases exhibit very short longitudinal magnetization recovery time ( $T_1$ ) and enable efficient signal averaging and high gyromagnetic ratio that collectively result in an improved signal-to-noise ratio (SNR).

To better understand and develop this novel technique, a vast number of pre-clinical animal experiments are required for validating and optimizing the radio frequency (RF) coils that are used to acquire MRI data [10-13]. The simplest approach would be to use single-tuned coils (i.e. RF coils each tuned to a single resonance frequency), such that a  $^1H$  coil is used to obtain anatomical information, while a separate  $^{19}F$  coil is used to obtain functional lung information. Unfortunately, this approach also requires image registration (i.e. co-alignment of separate images) in order to combine the information from the  $^{19}F$  and  $^1H$  coils. The purpose of this thesis is to eliminate the need for image registration by developing an optimized  $^1H/^{19}F$  dual-tuned coil for rodent lung imaging and disease model investigation.

## 1.2 Proposal and Motivation

In order to develop a robust and optimized dual-tuned  $^{19}F/^1H$  RF coil, the initial approach in this thesis was to use the coil inside coil method [14,15]. An important point to recognize is that decoupling these two frequencies is expected to be difficult since the frequencies of  $^{19}F$  and  $^1H$  are relatively close to each other. In literature studies, geometrical decoupling with one coil inside another coil was generally performed with frequencies that are very far away from each other [14]. In this thesis, poor results from the coil inside coil method were observed (Chapter 4). This result led to the development of additional dual-tuned  $^{19}F/^1H$  coils that used alternative decoupling method and theoretically increase the SNR by a factor of root two.

Later in this thesis (Chapter 5), a linear dual-tuned birdcage coil for  $^{19}\text{F}$  and  $^1\text{H}$  was built and sufficient isolation between the two frequencies was achieved. A major limitation of this design was that it only worked in a linear mode, whereas a quadrature dual-tuned  $^{19}\text{F}$ - $^1\text{H}$  coil should theoretically increase the resulting SNR by a factor of square root two. I concluded that a quadrature dual-tuned  $^{19}\text{F}$ - $^1\text{H}$  birdcage coil could be developed using PIN diodes to perform active switching between the two resonance frequencies<sup>[16,17]</sup>.

The quadrature dual-tuned  $^{19}\text{F}$ - $^1\text{H}$  birdcage coil that was constructed in this thesis (Chapter 6) was a volume coil where transmission and reception was performed through the same coil (i.e. transceiver). On the other hand, birdcage coils described in the literature were generally used for transmission only and a surface coil was used for reception only to achieve a high SNR. The advantage of using a single transceiver coil in this thesis is that the design is simpler than most of the designs reported in the literature. In order to overcome the SNR penalty from using a volume coil instead of a surface coil for reception, this coil was designed to work in quadrature mode, and the coil diameter was optimized to achieve a high filling factor for rat imaging. In addition, a volume coil should theoretically have a better  $B_1$  homogeneity than the surface coil (the sensitivity of the coil is affected by the inhomogeneous  $B_1$  field) reported in the literature, and for this reason  $B_1$  field mapping was performed to confirm that the  $B_1$  field is homogeneous throughout the volume coil.

### **1.3 Scope of the Thesis**

Three sets of radio frequency (RF) birdcage coils were designed and developed for imaging rodents using inert fluorinated gases on a Philips Achieva 3T scanner. Improved sensitivity and power consumption were measured, studied and compared. The  $B_1$  homogeneity for the coils was quantitatively measured.

An introduction to NMR and MRI fundamentals are presented in Chapter 2, along with a brief literature review. It also discusses about the fundamentals of birdcage RF coil design.

Chapter 3 describes the initial approach, which was to build two independent  $^{19}\text{F}$  and  $^1\text{H}$  coils and decouple them geometrically. The resonance frequency and impedance matching with balun circuits are also described.

To overcome the disadvantages of the geometrically decoupling technique, Chapter 4 describes the design and construction of linear dual tuned RF birdcage coil for  $^{19}\text{F}$  and  $^1\text{H}$ . Tuning and impedance matching with balun circuits are performed. A method to quantitatively measure  $B_1$  homogeneity at the center of the coils is also discussed. Both phantom results and *in vivo* results are presented and discussed in this chapter.

A quadrature dual tuned RF birdcage coil for  $^{19}\text{F}$  and  $^1\text{H}$  was designed and constructed for achieving higher SNR and for low power consumption.  $B_1$  field homogeneity of this coil is demonstrated. Phantom results and comparison of linear dual tuned to quadrature dual tuned results are presented and discussed in Chapter 5.

Finally, Chapter 6 summarizes the findings in this work and looks at future developments in some areas of the RF coils.

## Chapter 2

### Background and Literature Review

#### 2.1 Background

Inhaled inert fluorinated gas magnetic resonance imaging (MRI) is a promising technique for anatomical and functional lung imaging <sup>[18]</sup>. Unlike hyperpolarized gas imaging, fluorine-19 (<sup>19</sup>F) MRI of inert fluorinated gases does not require an expensive polarizer to polarize the gas, and the gases are relatively inexpensive and abundant. In order to better understand and develop this novel technique, a vast number of pre-clinical animal experiments are required for validation and optimization of radio frequency (RF) coils that are used to collect MRI data.<sup>[19]</sup> In the simplest case, only one RF coil is required for <sup>19</sup>F lung imaging; however, additional information can be obtained by performing multi-nuclear imaging that involves both <sup>19</sup>F and conventional proton (<sup>1</sup>H) MR imaging. Therefore, conventional <sup>1</sup>H MRI can provide structural lung information, while <sup>19</sup>F MRI can provide functional information regarding ventilation and the distribution of the inhaled gases.

In general, multi-nuclear MRI requires more than one RF coil in order to capture all the desired information. If two separate RF coils are used for <sup>19</sup>F and <sup>1</sup>H imaging, the subject will most likely need to be moved in order to switch the RF coils. In this case, image registration (i.e. co-alignment of separate images) may be required for correct for any shifts or distortions that result from the coil change. Previous work in our laboratory has developed single-tuned coils for <sup>19</sup>F imaging and <sup>1</sup>H imaging. The goal of this study was to develop a <sup>19</sup>F-<sup>1</sup>H dual-tuned coil that can be used to acquire inherently co-registered inert fluorinated gas ventilation images and their conventional <sup>1</sup>H analogues *in vivo*.

#### 2.2 Introduction to NMR

MRI is based on the principles of NMR. MRI is a powerful non-invasive tool used primarily in the medical imaging to produce high quality images of the human anatomy. MRI has a huge reputation because of its flexibility and sensitivity to a broad range of

tissue properties. Since it does not require the exposure of the subject to ionizing radiation, it is generally regarded as safer than other imaging techniques such as X-ray / computed tomography (CT). The applications of MRI continue to expand rapidly and advancements made in imaging techniques and acquisition speeds continue to further enhance and improve MRI images.

### 2.3 Spin Angular Momentum

The property of spin angular momentum was predicted by Dirac. This spin angular momentum is characterized by the spin quantum number  $I$ , such that the total spin angular momentum is  $I\hbar$ . The value of  $I$  is an intrinsic property of the nucleus. For example, the spin quantum number for  $^1\text{H}$  and  $^{19}\text{F}$  nucleus is  $1/2$ . In NMR, it is unpaired nuclear spins that are of importance rather than the paired ones whose effects are nullified because their magnitude gets cancelled. In order to exhibit the property of magnetic resonance the nucleus must have a non-zero value of  $I$ . The magnitude of the spin angular momentum is given by<sup>[20]</sup>:

$$\mu = \gamma\hbar\sqrt{I(I+1)} \quad (2-1)$$

where  $\hbar = h / 2\pi$ , where  $h$  is Planck's constant, and  $\gamma$  is gyromagnetic ratio. Where

$$\gamma = \frac{ge}{2m} \quad (2-2)$$

where,  $g$  - Lande  $g$ -factor

$e$  - the charge of an electron

$m$  - mass of the nucleus.

The spins are placed in an external static magnetic field  $B_0$ , the energy of the nuclei is split into  $2I+1$  states known as Zeeman effect.  $^1\text{H}$  has two energy states where,  $I=\pm 1/2$ :

$$E_{\pm 1/2} = \pm \frac{\gamma}{2} \hbar B_0 \quad (2-3)$$

These two energy states correspond to magnetic moments which are parallel and anti-parallel to  $B_0$ . A transition between these two energy states can happen by absorbing or emitting the energy equal to the energy difference between them.

$$\Delta E = \hbar\omega = |\gamma\hbar B_0| \quad (2-4)$$

$$\omega = \gamma B_0 \quad (2-5)$$

$\omega$  - Larmor frequency

## 2.4 Bulk Magnetization

When a group of spins are placed in a magnetic field, each spin aligns either in parallel or in anti-parallel state to the magnetic field. The number of spins in the parallel state  $N^+$  is higher than spins in anti-parallel state  $N^-$ , which is given by Boltzmann statistics as shown<sup>[21]</sup>,

$$\frac{N^+}{N^-} = \exp\left(\frac{-\Delta E}{k_B T}\right) \quad (2-6)$$

By substituting equation (1-4) we get,

$$\frac{N^+}{N^-} = \exp\left(\frac{\hbar\gamma B_0}{k_B T}\right) \quad (2-7)$$

$$\approx 1 - \frac{\hbar\gamma B_0}{k_B T} \quad \text{where } k_B T \gg \hbar\gamma B_0$$

Difference between the two spins is given by

$$N^+ - N^- = \frac{\hbar\gamma B_0}{2k_B T} \quad (2-8)$$

$\Delta E$  - Energy difference between the spin states

$k_B$  - Boltzmann's constant,  $1.3805 \times 10^{-23}$  J/kelvin

T - Temperature

If we now assume that all the parallel state nuclei have a magnetic moment of  $1/(2 * \hbar * \gamma)$ , then we can write the bulk magnetization of the spins packets as

$$M = N \left( \frac{\hbar \gamma}{2} \right) \left( \frac{\gamma \hbar B_0}{2 k_B T} \right) \quad (2-9)$$

$$M \approx N \left( \frac{\hbar \gamma}{2} \right)^2 \left( \frac{B_0}{k_B T} \right)$$

N - the number of spins

## 2.5 Nuclear Magnetic Resonance

If the spin magnetization vector M is placed in the magnetic field  $B_0$ , M will experience a torque. The equation of motion can be written as <sup>[22]</sup>

$$\frac{dM}{dt} = \gamma M \times B \quad (2-10)$$

If  $B$  is a static (time-independent) field along the  $z$  axis such that  $B = B_0 k$  then equation (1-10) becomes

$$\begin{aligned} \frac{dM_x}{dt} &= \gamma M_y B_0 \\ \frac{dM_y}{dt} &= -\gamma M_x B_0 \\ \frac{dM_z}{dt} &= 0 \end{aligned} \quad (2-11)$$

These differential equations yield the following solutions:

$$\begin{aligned}
M_x(t) &= M_x(0)\cos\omega_0t - M_y(0)\sin\omega_0t \\
M_y(t) &= M_x(0)\sin\omega_0t + M_y(0)\cos\omega_0t \\
M_z(t) &= M_z(0)
\end{aligned}
\tag{2-12}$$

where  $\omega_0 = \gamma B_0$  and i, j, k denote the unit vectors along x, y and z axis.

These equations describe the precession of the magnetization vector about the z axis as shown in Figure 2.1. The angular frequency of the precession is identical to the Larmor frequency.

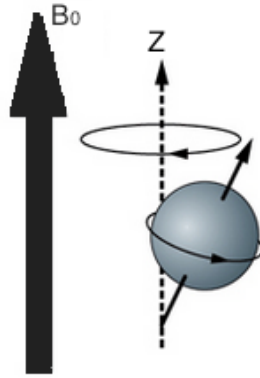


**Figure 2.1: Precession of the magnetization vector in static magnetic field along z-axis.**

Now, in addition to the static  $B_0$  field applied along z, consider a time varying  $B_1$  field applied perpendicularly to  $B_0$  and oscillating at  $\omega_0$ . If only the circularly polarized component of  $B_1$  is rotating in the same direction as the precession, magnetization vector is considered

$$B_1(t) = B_1 \cos\omega_0(t)i - B_1 \sin\omega_0(t)j \tag{2-13}$$

Substituting equation (1-11) in (1-13) gives rise to

$$\begin{aligned}
\frac{dM_y}{dt} &= \gamma[-M_x B_0 + M_z B_1 \cos\omega_0 t] \\
\frac{dM_z}{dt} &= \gamma[-M_x B_1 \sin\omega_0 t - M_y B_1 \cos\omega_0 t]
\end{aligned}
\tag{2-14}$$

if  $M(0) = M_0 k$

$$\begin{aligned}M_x(t) &= M_0 \sin \omega_1 t \sin \omega_0 t \\M_y(t) &= M_0 \sin \omega_1 t \cos \omega_0 t \\M_z(t) &= M_0 \cos \omega_0 t\end{aligned}\tag{2-15}$$

Where  $\omega_1 = \gamma B_1$ . This suggests that by applying an oscillating magnetic field of frequency  $\omega_0$  the magnetization simultaneously precesses about  $B_0$  at  $\omega_0$  and  $B_1$  at  $\omega_1$ , as shown in Figure 2.2.

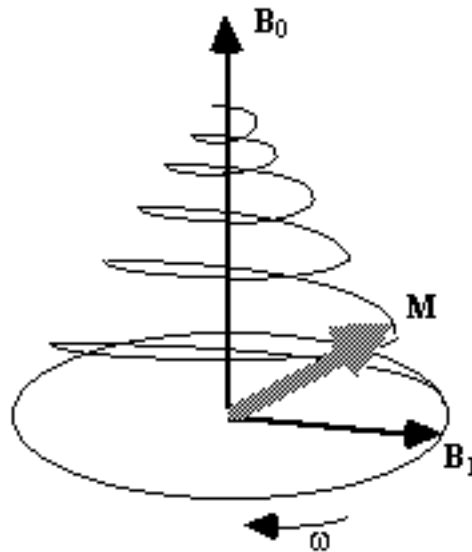


**Figure 2.2: Precession of magnetization with longitudinal field  $B_0$  in rotating field.**

The most common way to carry out an NMR experiment is to apply a short burst of resonant RF field. If the duration of this RF pulse is  $t$ , then the magnetization will rotate by an angle (in radians):

$$\theta = \gamma B_1 t\tag{2-16}$$

$\theta$  - Flip angle

### 2.5.1 T<sub>1</sub> Relaxation

The application of a resonant RF pulse disturbs the spin system, subsequently there must be a process that makes it come back to equilibrium. At equilibrium, if the net magnetization vector  $M_0$  lies along the magnetic field  $B_0$ , then the z-component of the magnetization  $M_z$  equals  $M_0$ .  $M_z$  is referred to as longitudinal magnetization. It is possible to change the net magnetization and saturate the system ( $M_z = 0$ ) by exposing it to energy at a frequency equal to the energy difference between the two spin states. The time constant, which describes how  $M_z$  returns to its equilibrium value is called the spin lattice relaxation time ( $T_1$ ). The equation governing this behavior as a function of the time  $t$  after its displacement is<sup>[3]</sup>:

$$\frac{dM_z}{dt} = -\frac{(M_z - M_0)}{T_1}$$
$$M_z = M_0(1 - e^{-t/T_1}) \quad (2-17)$$

The spin lattice relaxation time ( $T_1$ ) is the time to reduce the difference between the longitudinal magnetization ( $M_z$ ) and its equilibrium value by a factor of  $e$ .  $T_1$  relaxation is shown in the Figure 2.3

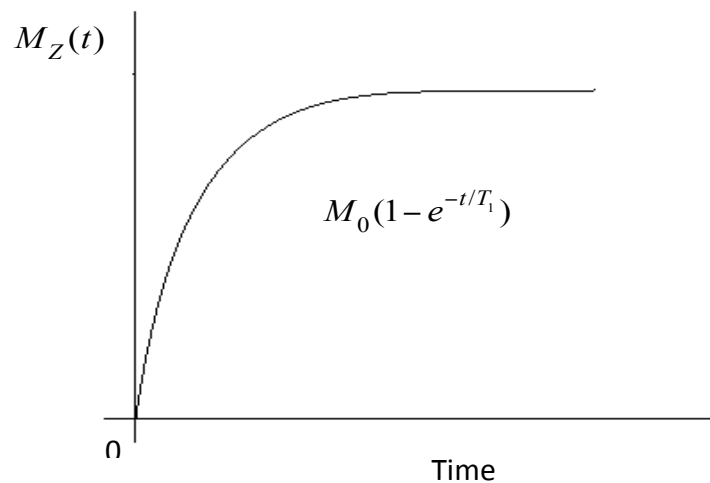


**Figure 2.3: T<sub>1</sub> relaxation.**

## 2.5.2 T<sub>2</sub> relaxation

The net magnetization starts to de-phase because each of the spin packets is experiencing a slightly different magnetic field; rotating at its own Larmor frequency. The time constant which describes the return to equilibrium of the transverse magnetization,  $M_{XY}$ , is called the “spin-spin relaxation” time,  $T_2$ . The net magnetization in the XY plane goes to zero, and the longitudinal magnetization grows until we have  $M_0$  along z.  $T_2$  relaxation is shown in Figure 2.4.

$$\frac{dM_x}{dt} = -\frac{M_x}{T_2}$$

$$\frac{dM_y}{dt} = -\frac{M_y}{T_2}$$

$$M_{XY} = M_{XY} e^{-t/T_2} \quad (2-18)$$

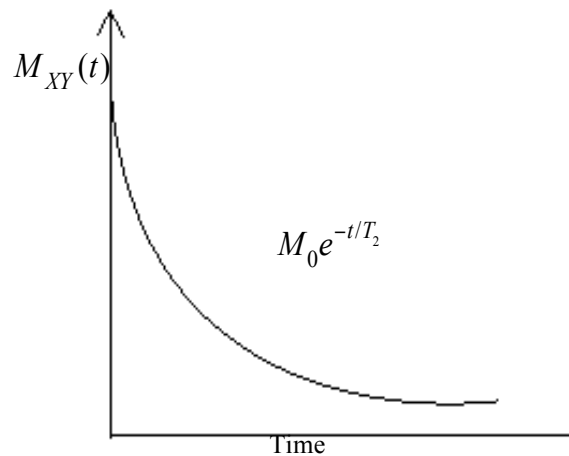


**Figure 2.4: T<sub>2</sub> relaxation.**

Both longitudinal and transverse relaxation occurs simultaneously, but  $T_2$  is always less than or equal to  $T_1$ .

### 2.5.3 Bloch Equations

The  $T_1$  and  $T_2$  relaxation equations (2-17) and (2-18) from the previous sections can be combined with the equations of motion to yield the phenomenological Bloch equations<sup>[23]</sup>:

$$\begin{aligned}\frac{dM_x}{dt} &= \gamma M_y \left( B_0 - \frac{\omega}{\gamma} \right) - \frac{M_x}{T_2} \\ \frac{dM_y}{dt} &= \gamma M_z B_1 - \gamma M_x \left( B_0 - \frac{\omega}{\gamma} \right) - \frac{M_y}{T_2} \\ \frac{dM_z}{dt} &= -\gamma M_y B_1 - \frac{(M_z - M_0)}{T_1}\end{aligned}\tag{2-19}$$

Following the application of a  $\theta_x$  pulse, the magnetization vector has the components

$$\begin{aligned}M_x(0) &= 0 \\ M_y(0) &= M_0 \sin \theta \\ M_z(0) &= M_0 \cos \theta\end{aligned}\tag{2-20}$$

When substituted into Bloch equations, it gives rise to

$$\begin{aligned}M_x(t) &= M_0 \sin \theta \sin(\omega_0 t) \exp\left(\frac{-t}{T_2}\right) \\ M_y(t) &= M_0 \sin \theta \cos(\omega_0 t) \exp\left(\frac{-t}{T_2}\right) \\ M_z(t) &= M_0 \left[ 1 - (1 - \cos \theta) \exp\left(\frac{-t}{T_1}\right) \right]\end{aligned}\tag{2-21}$$

To detect the NMR signal, it is necessary to have an RF coil which is in the transverse plane that is perpendicular to the  $B_0$  field. Also, an emf is induced in to the coil which is proportional to  $M_x$ . Both signals oscillate at the Larmor frequency, but are  $90^\circ$  out of phase with each other. Thus the signal detected in the coil has the form,

$$S(t) = S_0 \exp\left(\frac{-t}{T_2}\right) \cos \omega t \quad (2-22)$$

If  $\omega = \omega_0$ , then the signal is just an exponential decay. However, if  $\omega \neq \omega_0$ , then the signal will oscillate at a frequency  $\Delta f$ . The signal after phase sensitive detection is known as the Free Induction Decay (FID).

## 2.6 Magnetic Resonance Imaging

### 2.6.1 Slice selection

Slice selection is a technique used to isolate a specific slab of magnetization, such that the resulting image only represents the spins in that plane. An RF pulse, which only affects a limited part of the NMR spectrum is applied, in the presence of a linear magnetic field gradient that is perpendicular to the slice that is to be selected. This results in the excitation of only those spins whose Larmor frequency, which is dictated by their position, is within the bandwidth of frequencies that are excited by the applied RF pulse. Figure 2.5 shows a long cylindrical object aligned along the z-axis in a magnetic field gradient which increases linearly with increasing z.

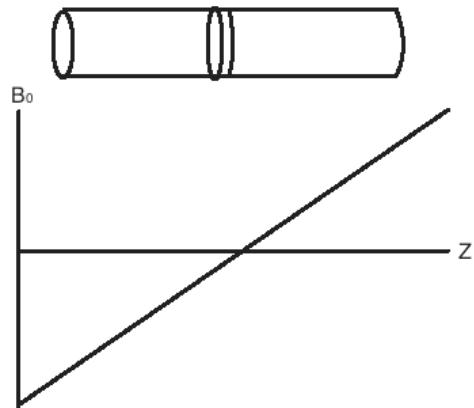


**Figure 2.5: The slice selection in cylindrical object, with a linear magnetic field gradient along the z-axis.**

## 2.6.2 K-space

When acquiring and handling MRI data, the sequence of events plays a very important role. The order at which RF pulses and magnetic field gradients are applied is referred to as a pulse sequence. In essence, magnetic field gradients apply phase to the excited magnetization, and the received signal can be represented by the following equation (in one dimension)<sup>[24]</sup>:

$$s(k) = \int dz \rho(z) \exp^{i2\pi kz} \quad (2-23)$$

Where  $\rho$  is the magnetization density and the spatial frequency,  $k$ , is defined as:

$$k(t) = \gamma \int_0^T G(t) dt \quad (2-24)$$

$G(t)$  - Time dependent gradient magnetic field.

In 2D imaging, phase is applied in two directions, where the  $k_x$ -axis is typically represents the frequency encoding direction, and the  $k_y$ -axis typically represents the phase encoding direction. Various combinations of frequency and phase encoding gradients are then used to acquire a complete k-space data set. Data near the center of k-space contains information about the contrast and large details of the image, while data at the edge of k-space contains the fine details and edge information. In any pulse sequence, data are stored with reference to k-space positions and are then Fourier transformed to reconstruct the final image.

## 2.7 Birdcage Coils

RF coils are used for transmitting the RF pulse to excite the spins at a region of interest in the body as well as receiving the generated MR signal. In the field of MRI, RF coils act as sensor that picks up the signal to be then amplified and processed to generate an MR imaging. There are different ways that we can design RF coils, and they are usually classified by their geometry: surface coils and volume coils etc. Every coil has its own advantages and disadvantages. For example, surface coils produce less homogenous  $B_1$  field but yields higher SNR, whereas the volumes coils, such as saddle coils produces a homogenous magnetic field but yields poor SNR.

It is very important to design RF coils such that they are homogenous but also give acceptable SNR. This can be obtained using birdcage coils where the fields are homogeneous and with a very little SNR penalty compared to surface coils. The basic resistor, inductor and capacitor (RLC) circuits for birdcage coil and impedance matching for birdcage coil are also discussed.

### 2.7.1 Basic Birdcage Coil Design

Hayes *et al.* (1985)<sup>[25]</sup> were the first to design birdcage coils. These are extensively used in the field of MRI because they provide a circular polarized field with high homogeneity. These coils are constructed with multiple parallel conductive segments (rungs) that are parallel to the magnetic field  $B_0$ . The rungs are connected with a pair of end rings. Capacitors can be placed either on the rungs (Low pass) or on the end rings (High pass) or on both (Band pass) as shown in Figures 2.6 and 2.7.  $L_1$  represents the equivalent inductance on the end ring segment,  $C$  is the tuning capacitor, and  $L_2$  is the equivalent inductance on the legs.

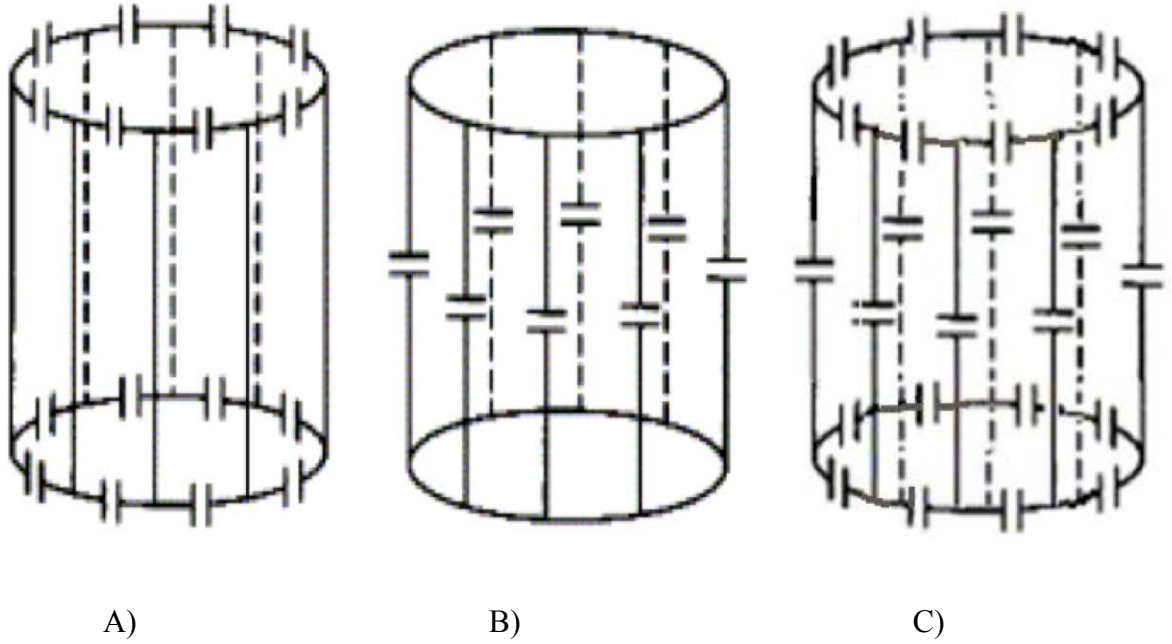


**Figure 2.6: Birdcage coils in A) High Pass mode B) Low Pass mode C) Band Pass Mode <sup>[26]</sup>.**

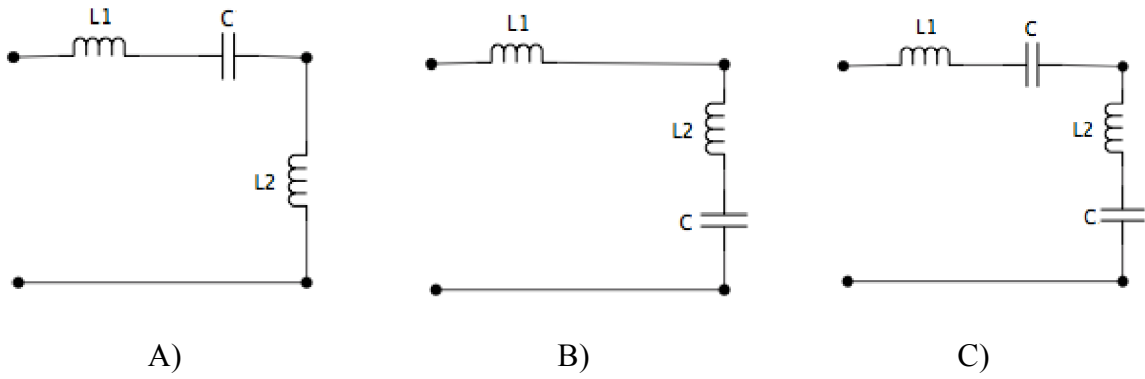


**Figure 2.7: Equivalent Circuits for birdcage coils in A) High Pass mode B) Low Pass mode C) Band Pass mode.**

## 2.7.2 Birdcage Builder

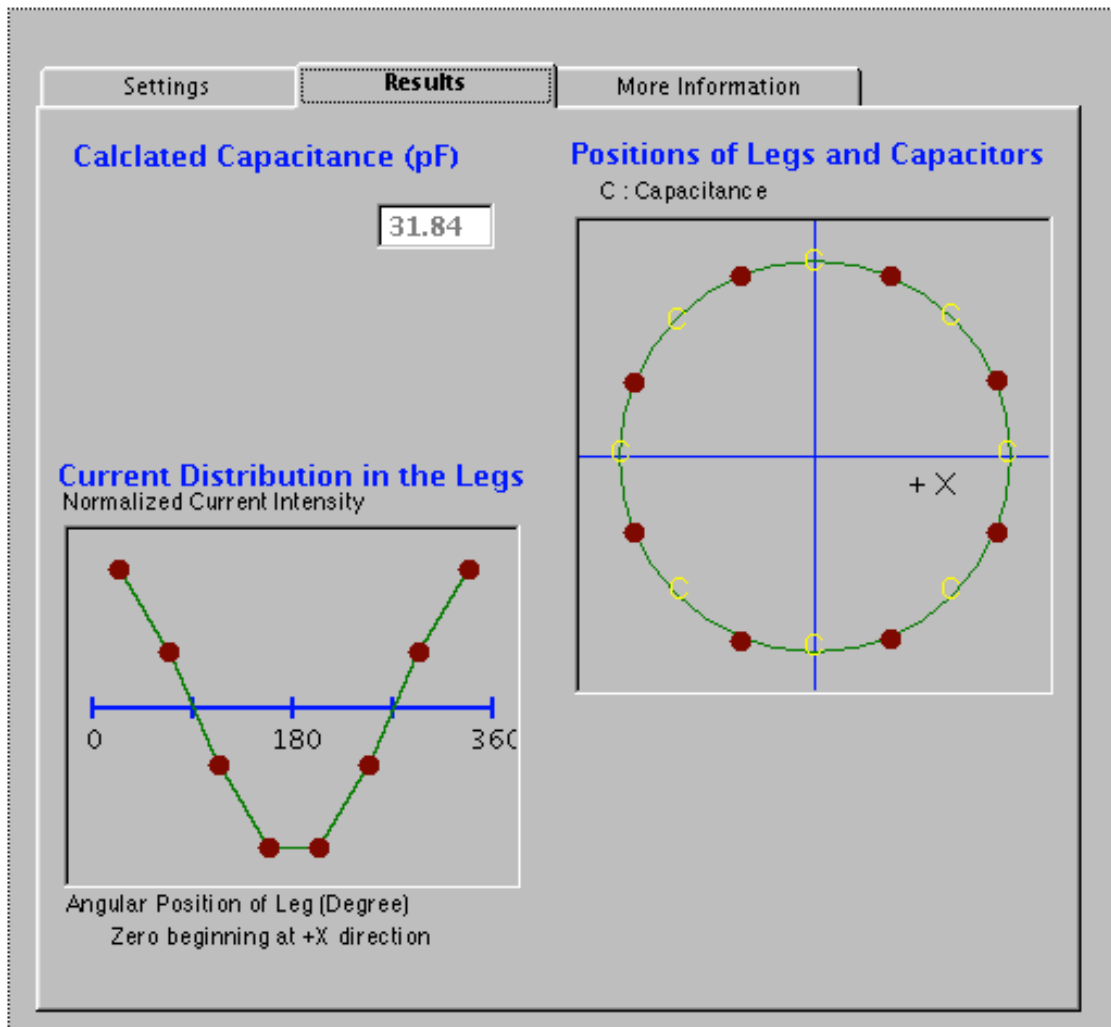
Birdcage builder is a software package that has been widely used all over the world in the field of MRI. It calculates the mutual inductance, effective inductance and capacitance values <sup>[27]</sup> of an RF coil. In this thesis birdcage builder software was used to for calculating the capacitance values based on the geometry of the coil (Figure 2.8).

The screenshot displays the 'Settings' tab of the Birdcage Builder software. The interface is organized into several sections:

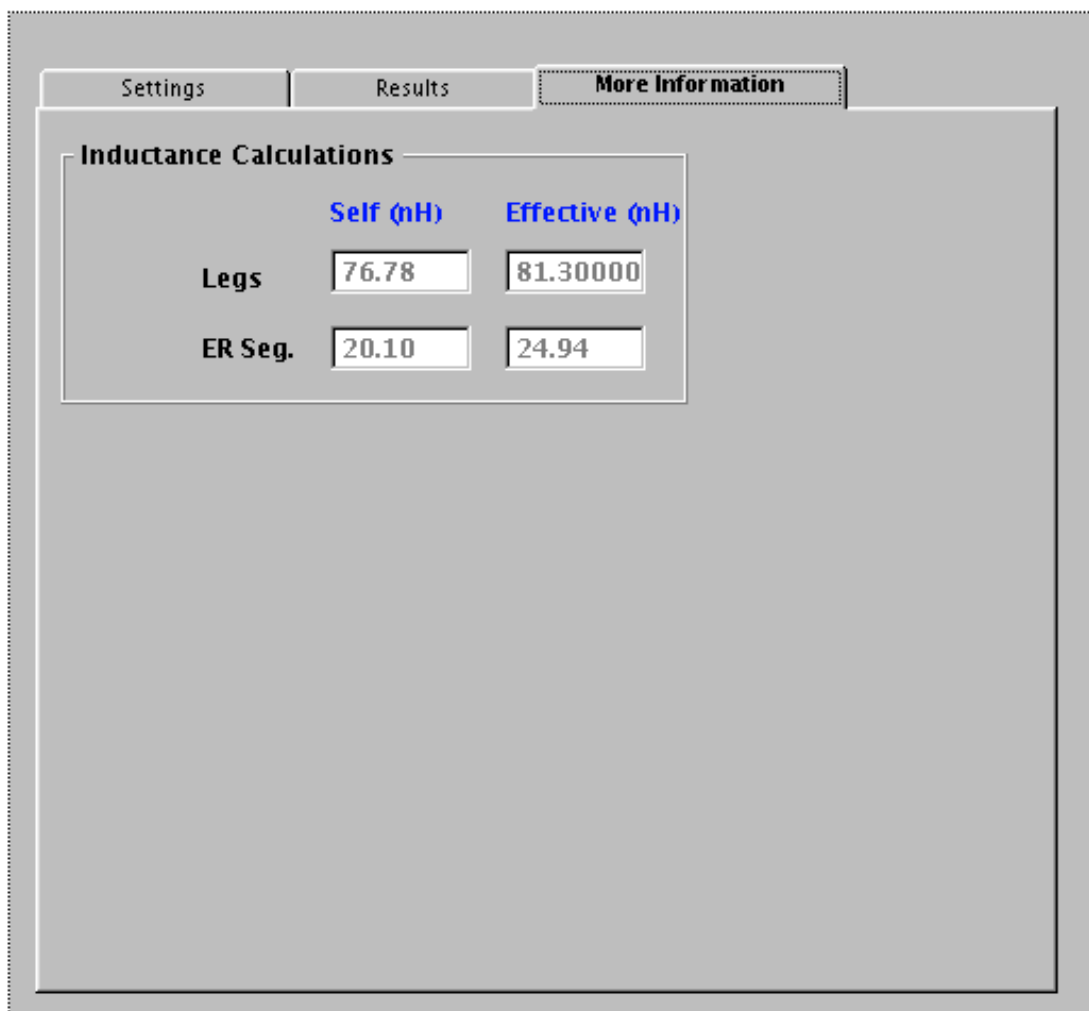
- Configuration:** Includes radio buttons for 'High-Pas' (selected), 'Low-Pass', and 'Band-Pas'.
- Resonant Freq. (MHz):** A dropdown menu showing '27.74'.
- Type of Leg:** Radio buttons for 'Rectangular' (selected) and 'Tubular'.
- Type of ER:** Radio buttons for 'Rectangular' (selected) and 'Tubular'.
- Number of Legs:** A slider control with tick marks at 8, 12, 16, 20, and 24.
- Dimensions:** Input fields for:
  - Leg Length (cm): 9.76
  - Leg Width (cm): 0.63
  - Coil Radius (cm): 4.415
  - RF shield Radius (cm): 0
  - ER Seg. Length (cm): 3.46999
  - ER Seg. Width (cm): 0.63

A 'Calculate' button is located at the bottom center of the settings panel.

(a)



(b)



(c)

**Figure 2.8: (a) Coil specifications are defined to build a birdcage coil.**

**(b) Calculated capacitance and position of the capacitors to be placed on the end ring.**

**(c) Calculated self-inductance and effective inductance of the coil.**

## 2.8 Generation of RF Fields and Signal Reception

In order to excite the spins and produce a signal, the magnetization must be generated using an RF pulse, which consists of a magnetic field  $B_1$  alternating at the Larmor frequency. The RF pulse is produced by a transmit coil, according to Ampere's Law <sup>[28]</sup>:

$$\frac{1}{\mu_0} \oint B \cdot dl = \int_S J \cdot dS \quad (2-25)$$

$J$  - Current Density

$B$  - Magnetic Flux Density

$\mu_0$  - Permeability Constant

$S$  - Surface

Ampere's Law states that the closed path integration of a magnetic field is equal to the current passing through the surface that is enclosed by that path. It is desirable to have a homogeneous  $B_1$  transmission profile, which means that the transmit coil has a uniform magnetic field rotating at the desired Larmor frequency.

After the magnetization has been excited using an RF pulse, the precessing magnetization induces an EMF  $\xi$  in the receive coil according to Faraday's law of induction <sup>[28]</sup>:

$$\xi = -\frac{d}{dt} \int_S B \cdot dS = -\int_V \left( \frac{dM(r)}{dt} \right) B_1(r) \cdot dV \quad (2-26)$$

where  $B$  refers to the magnetic field produced by the precessing magnetization,  $M$ , at a given position,  $r$ . In this context,  $B_1$  is the coil sensitivity, defined as the magnetic field that would be produced by the receive coil per unit current, and  $V$  is the volume of the sample. Sensitivity is determined by the coil design, and it should ideally be homogeneous across the sample that is to be imaged. Since the precessing magnetization is rotating at the Larmor frequency, the voltage induced in the coil,  $S$ , can be expressed in the following way:

$$S = M_0 \omega_0 \int_S \sin \theta \cdot B_1(r) dV \quad (2-27)$$

where  $\theta$  is the flip angle and  $M_0$  is the equilibrium magnetization of the sample. In general, two separate coils are used for transmission and reception as each coil can be designed for optimal performances at the desired Larmor frequencies <sup>[29]</sup> and  $M_0$  can be expressed as:

$$M_0 = \frac{N\gamma^2\hbar^2 B_0}{4k_B T_S} \quad (2-28)$$

$N$  = Number of spins

$\gamma$  = Gyro magnetic ratio

$k_B$  = Boltzmann's constant

$T_S$  = Sample temperature

$\hbar$  = Planck's Constant

By inserting equation (2-27) into (2-28) we can obtain a final expression for the signal induced in the coil <sup>[30]</sup>:

$$S = \left( \frac{n_s \gamma^2 \hbar^2 B_0 B_1}{4k_B T_S} \right) \sin \theta V \quad (2-29)$$

## 2.9 Resonance Circuits and Impedance Matching

The RF coils are designed to achieve resonance at a certain Larmor frequency. The RF coil can be described with a simple RLC circuit <sup>[31]</sup>, as shown in Figure 2.9, where the signal is measured across the capacitor C.

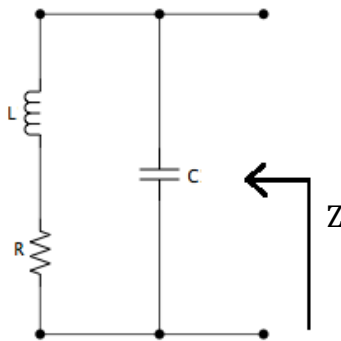


**Figure 2.9: Resonant equivalent circuit of a simple loop coil.**

From the above figure, L is the inductance of the copper tape, R is the resistance of the copper tape and C is the calculated capacitor. The impedance when coupling the coil to a transmission line capacitively is given by the following:

$$Z = \frac{(R + j\omega L) \frac{1}{j\omega C}}{R + j\omega L + \frac{1}{j\omega C}} \quad (2-30)$$

In the field of MRI, the coil transmits the signal to the pre-amplifier and it is important to detect the FID (Field Induction decay) signal from the coil. Impedance matching plays a vital role as signal reflections should be minimized [32,33].

$$\Gamma = \frac{Z_{Coil} - Z_{TL}}{Z_{Coil} + Z_{TL}} \quad (2-31)$$

$\Gamma$  - Reflection coefficient

$Z_{coil}$  is the coil impedance

$Z_{TL}$  is the transmission line impedance.

The reflections would be ideally reduced to zero when  $\Gamma = 0$ , meaning:

$$Z_{TL} = Z_{coil} \quad (2-32)$$

## 2.10 Signal to Noise Ratio (SNR)

The most common way to measure the SNR in the field of MRI is by performing image based measurements during post processing. Regions of interest are selected and SNR is defined as the following:

$$SNR = \frac{S}{\sigma} \quad (2-33)$$

S – Mean signal from the region of interest.

$\sigma$  - Standard deviation of noise.

## 2.11 Q Factor

The Q factor is defined as the energy stored to energy dissipated during one cycle<sup>[32]</sup>. In this thesis, Q factor is calculated in terms of frequency bandwidth according to the following equation

$$Q = \frac{f_0}{\Delta f} \quad (2-34)$$

Where  $f_0$  is the resonance frequency and  $\Delta f$  is range of frequency bandwidth at the half peak power value. Typically the Q factor ranges from 50 to 500<sup>[35]</sup>.

## 2.12 Literature Review

In 2010, Seunghoon et al. developed a dual-tuned RF coil for multi-nuclear sodium-23 (<sup>23</sup>Na) and <sup>1</sup>H MR imaging using a PIN diode.<sup>[32]</sup> At a magnetic field strength of 4 T, the resonance frequency of <sup>23</sup>Na is 45.04 MHz and the <sup>1</sup>H resonance frequency is 170.28 MHz. In this study, Seunghoon et al. compared two different designs for dual-tuned <sup>23</sup>Na-<sup>1</sup>H RF surface coils. Both coils had an identical geometry; however, one coil had a trap circuit (i.e. a circuit which acts as a notch filter that shut down a particular frequency), while the other coil had PIN diodes for the <sup>23</sup>Na and <sup>1</sup>H frequencies, and switching between the two resonant modes was performed by applying voltage across the PIN diodes (PIN diodes are forward biased by applying +10v and reversed biased by applying -100v) .. The dual-tuned coil with PIN diodes was determined to be the optimal case, since the dual tuned coil with the trap circuit showed an increase in coil losses, which affected the optimal tuning and matching for both frequencies. This study used a dual-tuned birdcage coil was used for transmission and a dual-tuned surface coil was used for reception; however the disadvantage of this design is that surface coils are inherently inhomogeneous (i.e. the coil sensitivity varies with spatial position). This situation could potentially be improved by developing more homogenous coils for signal reception.

In 2014, Lim et al. constructed a linear dual-tuned birdcage coil for hyperpolarized carbon ( $^{13}\text{C}$ ) and conventional  $^1\text{H}$  MR imaging.<sup>[36]</sup> At a magnetic field strength of 3 T, the resonance frequency of  $^{13}\text{C}$  is 32.11 MHz, and the  $^1\text{H}$  resonance frequency is 127.74 MHz. In this paper, a band pass birdcage coil was constructed, where a  $^{13}\text{C}$  channel was taken from the legs of the birdcage, and a  $^1\text{H}$  channel was taken from the end ring. PIN diodes were placed on the end ring to isolate the  $^{13}\text{C}$  channel. By supplying a DC voltage across the PIN diodes, a rapid switch between the  $^{13}\text{C}$  and  $^1\text{H}$  frequencies was achieved. A surface coil for  $^{13}\text{C}$  was also built for signal reception. The birdcage coil and surface coil were integrated through a T/R switch.  $^1\text{H}$  imaging was performed using the dual-tuned coil (i.e. both excitation and reception were performed using the same coil), while  $^{13}\text{C}$  imaging was performed using a TORO approach (i.e. transmit only using the dual-tuned coil, and receive only using surface coil). The  $^{13}\text{C}$  receive surface coil allows for a very high SNR at the expense of having an inhomogeneous  $B_1$  field. This design can be further improved by driving the coils quadrature mode. In general, this decoupling approach works well with frequencies that are very far apart from one another, such as  $^{13}\text{C}$  and  $^1\text{H}$ . Therefore, this approach would be very difficult when working with close frequencies such as  $^{19}\text{F}$  and  $^1\text{H}$ .

Wang et al. developed an efficient double-switch birdcage coil tuned to helium-3 ( $^3\text{He}$ ) and  $^1\text{H}$ .<sup>[37]</sup> At a magnetic field strength of 3 T, the  $^3\text{He}$  resonance frequency is 97.32MHz and the  $^1\text{H}$  resonance frequency is 127.74 MHz. In this paper, a conventional 8-rung  $^1\text{H}$  birdcage coil was built. An additional end-ring pair was then added onto the  $^1\text{H}$  birdcage coil using capacitors and diodes. When the diodes are in the “ON” state, the outer end-rings operate together with the inner end-rings and the coil is switched to the  $^3\text{He}$  frequency. When diodes are in the “OFF” state, the coil eliminates the outer end ring and is switched to the  $^1\text{H}$  frequency. All 8 diodes on the same end-ring are powered in series to ensure an equal DC current. Although this dual-tuned coil design worked well for the  $^3\text{He}$  and  $^1\text{H}$  frequencies, this was a complicated design that may not work well for the  $^{19}\text{F}$  and  $^1\text{H}$  frequencies.

In 2010, Aktham Asfour developed a dedicated RF sensor for rat brain MRI using  $^{129}\text{Xe}$  and  $^1\text{H}$ .<sup>[14]</sup> At a magnetic field strength of 2.35 T, the  $^{129}\text{Xe}$  resonance frequency is 27.7

MHz and the  $^1\text{H}$  resonance frequency is 100 MHz. In this paper, two independent linear birdcage coils for  $^{129}\text{Xe}$  and  $^1\text{H}$  were constructed. The  $^{129}\text{Xe}$  coil was built as a high pass birdcage coil and the  $^1\text{H}$  coil was built as a low pass birdcage coil. The diameter of the  $^1\text{H}$  coil was designed to be bigger than the diameter of the  $^{129}\text{Xe}$  coil, so that the  $^{129}\text{Xe}$  coil could be placed inside the  $^1\text{H}$  coil and geometrical decoupling could be performed. A  $^{129}\text{Xe}$  surface coil was constructed for reception and the birdcage coil was used for transmission. The receive-only  $^{129}\text{Xe}$  surface coil was de-coupled from the double-tuned volume coil by an active decoupling circuitry based on the use of PIN diodes. Even in this paper, the frequencies were very far away from each other and a surface coil was used for reception which has inhomogeneous field. This dual-tuned coil design could also be improved upon by building volume coils for transmission and reception and also by driving the coils in quadrature mode.

Previous work in our laboratory performed hyperpolarized  $^{129}\text{Xe}$  and  $^1\text{H}$  MR imaging of the rat lung at 3T using a geometrically decoupled dual-tuned birdcage coil.<sup>[15]</sup> In this work, two independent coils were constructed for  $^{129}\text{Xe}$  and  $^1\text{H}$ , and the two coils were placed one inside the other. Decoupling was performed by rotating the coil geometrically. This coil was used for both transmission and reception of the MRI signals. One disadvantage of hyperpolarized  $^{129}\text{Xe}$  imaging is that the technique requires an expensive polarizer and gases that are enriched with  $^{129}\text{Xe}$  isotopes are very expensive. A potential alternative to hyperpolarized  $^{129}\text{Xe}$  imaging is  $^{19}\text{F}$  MRI of inert fluorinated gases. Since this is a technique that is currently under development, researchers are focusing on developing  $^{19}\text{F}$  imaging techniques in animal models of disease. Performing these studies requires a robust and optimized dual-tuned coil design that can provide a very high SNR for both the  $^{19}\text{F}$  and  $^1\text{H}$  frequencies. The purpose of this thesis is to develop a dual-tuned quadrature  $^{19}\text{F}$  and  $^1\text{H}$  coil for animal studies and to determine the best methods to decouple these two frequencies that are very close to each other.

Hu et al. developed a generalized strategy for designing  $^{19}\text{F}$  and  $^1\text{H}$  dual-tuned MRI coils for small animal imaging at 4.7 T<sup>[16]</sup>. The first coil design in this study was a transmit/receive birdcage coil for whole-body animal imaging. A matching circuit was placed on the birdcage coil, and the S11 response indicated two peaks for  $^1\text{H}$  and  $^{19}\text{F}$ . The

second coil design in this study was an actively-decoupled  $^1\text{H}$  saddle coil that can be used with an actively-decoupled  $^{19}\text{F}$  surface coil. The  $^1\text{H}$  saddle coil was built with PIN diodes and the  $^{19}\text{F}$  surface coil was built and placed inside the saddle coil. Active switching between the two frequencies was performed by supplying voltage across the PIN diodes. In our design, we prefer to have a single peak per coil in order to minimize the amount of power that is required to calibrate the coil and two independent birdcage coils are used as they have a better homogeneity fields.

Alecci et al. presented a practical design for a dual-tuned RF surface coil for interleaved  $^1\text{H}$  and  $^{23}\text{Na}$  rat brain imaging at 4T.<sup>[38]</sup> In this paper, Alecci et al. developed a dual-frequency RF surface coil comprised of a large loop tuned to the  $^1\text{H}$  frequency and a smaller co-planar loop tuned to the  $^{23}\text{Na}$  frequency. The mutual coupling between the two loops was eliminated by the use of a trap circuit inserted in the smaller coil. This independent-loop design was versatile since it enabled a separate optimization of the sensitivity and RF field distributions of the two coils. The disadvantage of this approach is that it uses surface coils that will have an inhomogeneous  $B_1$  field, and this design may not efficiently decouple frequencies that are very close to each other.

Ji et al. designed an eight-channel  $^{19}\text{F}$ - $^1\text{H}$  dual-tuned transceiver RF coil array for molecular imaging of fluorinated drugs in the human knee.<sup>[39]</sup> This study was performed at 7 T, and the  $^{19}\text{F}$ - $^1\text{H}$  RF coil array includes a posterior module with two  $^1\text{H}$  loop elements and two anterior modules, each consisting of one  $^1\text{H}$  and two  $^{19}\text{F}$  elements. The decoupling of neighbor elements is achieved by a shared capacitor. This design may be useful for future human lung imaging using inert fluorinated gas MRI; however, an eight-channel coil array is not feasible for small animal lung imaging.

Klomp et al. developed a dual frequency surface coil for the optimization of localized  $^{19}\text{F}$  magnetic resonance spectroscopy for the detection of fluorinated drugs in the human liver at 1.5 T.<sup>[17]</sup> The hardware was optimized by using circularly polarized coils together with integrated preamplifiers. The electronic scheme of the coil setup included a triple  $\pi$  circuit and a small band quadrature hybrid box. During the  $^1\text{H}$  measurements, the balancing capacitor of both coil elements was made resonant at 63.6 MHz (i.e. the  $^1\text{H}$

frequency) with an inductor in series with a PIN diode. In the future, this approach may be useful for developing human-sized dual-tuned  $^{19}\text{F}$ - $^1\text{H}$  RF coils for inert fluorinated gas MRI. However, small animal surface coils will not have the homogeneity required for imaging.

## Chapter 3

### A Linear $^{19}\text{F}$ - $^1\text{H}$ Double Birdcage Coil (Coil Inside Coil)

#### 3.1 Introduction

Inhaled inert fluorinated gas MRI is a promising technique for anatomical and functional lung imaging<sup>[40]</sup>. To better understand and develop this novel technique, a vast number of pre-clinical animal experiments are required for validation and optimization of radio frequency (RF) coils. Before the advent of dual-tuned coils, multinuclear studies required more than one RF coil to capture all the desired information. Since the subject needs to be moved in order to switch the RF coils, image registration (co-alignment of separate images) may be required for correct image interpretation. The purpose of this study was to develop a linear  $^{19}\text{F}$ - $^1\text{H}$  double birdcage coil using a coil inside coil method and to acquire inherently co-registered inert fluorinated gas ventilation images and conventional proton image analogues *in vivo*.

In this chapter two independent coils are described, where one coil is  $^{19}\text{F}$ -sensitive and the other coil is  $^1\text{H}$ -sensitive. The diameter of  $^1\text{H}$  coil was designed to be larger than the  $^{19}\text{F}$  coil, so that the  $^{19}\text{F}$  coil can be placed inside the  $^1\text{H}$  coil. The basic concept of this coil is geometrical decoupling by placing the coils concentric to each other<sup>[41-43]</sup>.

#### 3.2 $^1\text{H}$ and $^{19}\text{F}$ Birdcage Coil Construction and Tuning

Two linear independent coils were constructed using an acrylic tube and copper tape. Initially two independent coils for  $^1\text{H}$  and  $^{19}\text{F}$  were made to be on resonance. When the coils were placed one inside the other, the frequencies shifted far away from each other due to mutual inductance. The coil was experimentally detuned such that the frequency of  $^1\text{H}$  was 129.5 MHz, and the  $^{19}\text{F}$  coil was then tuned to 115 MHz. The two coils were made with different diameters to implement the double birdcage structure. The  $^{19}\text{F}$  coil was constructed on a smaller acrylic tube with a smaller diameter and the  $^1\text{H}$  coil was constructed on a bigger acrylic tube with a bigger diameter. Theoretically, geometrical

decoupling for double birdcage coils works best when the frequencies are far from each other. For example,  $^{129}\text{Xe}$  has a frequency of 35.33 MHz at 3T, which can be easily decoupled from  $^1\text{H}$  using the geometric technique. In this case, the two frequencies of  $^{19}\text{F}$  and  $^1\text{H}$  are very close to each other and are separated by 7.6 MHz, which will create additional challenges. Dimensions of both coils are shown in the table 3.1. Capacitor values can be obtained by using a birdcage builder <sup>[44]</sup>, which will give the capacitor values. The value of the capacitor will be changed based on the tuning of the coil.

Nuclei	Frequency (MHz)	Coil Diameter (mm)	Leg Length (mm)	Copper Tape Width (mm)	Tuning Capacitors (pf)
$^1\text{H}$	129.5	100.6	109.4	6.3	26
$^{19}\text{F}$	115	63.6	67.3	3.15	57

**Table 3.1 : Dimensions of the coil showing off resonance tuning.**

Figure 3.1 shows the illustration of the coil and Figure 3.2 shows the circuit diagram. Figure 3.3 shows the coil that was constructed, and Figure 3.4 shows  $S_{11}$  on the network analyzer.

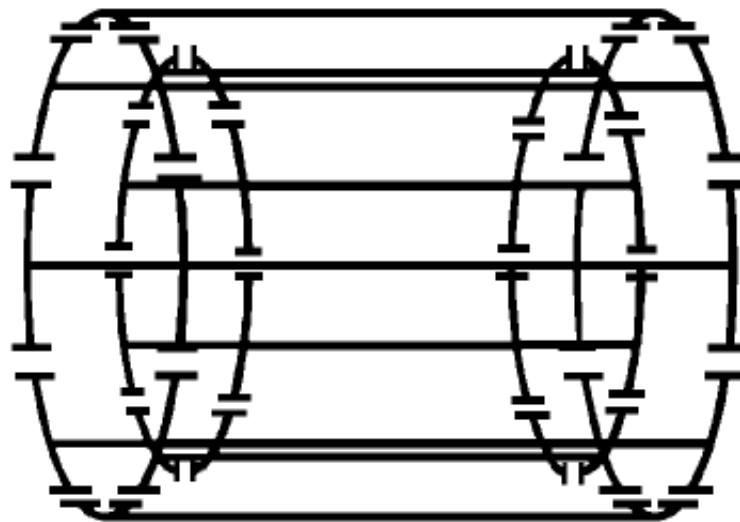


**Figure 3.1 Illustration of the double birdcage coil.**

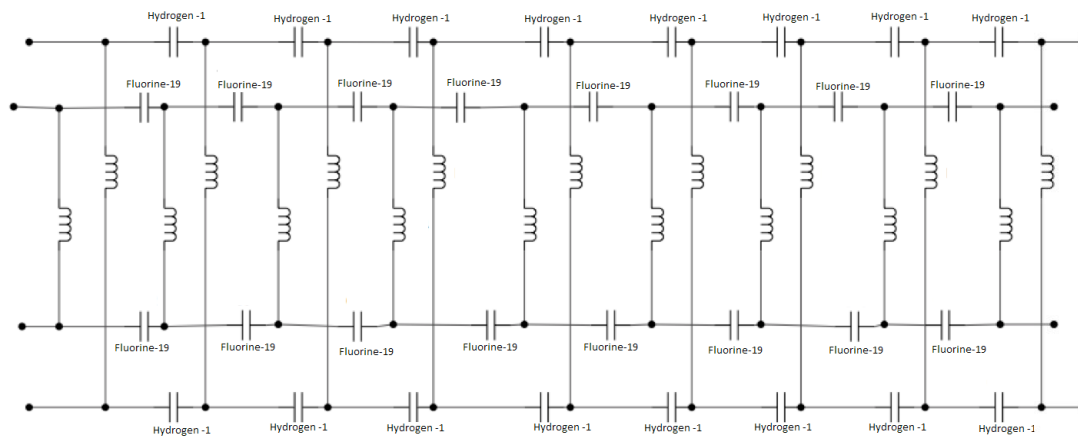
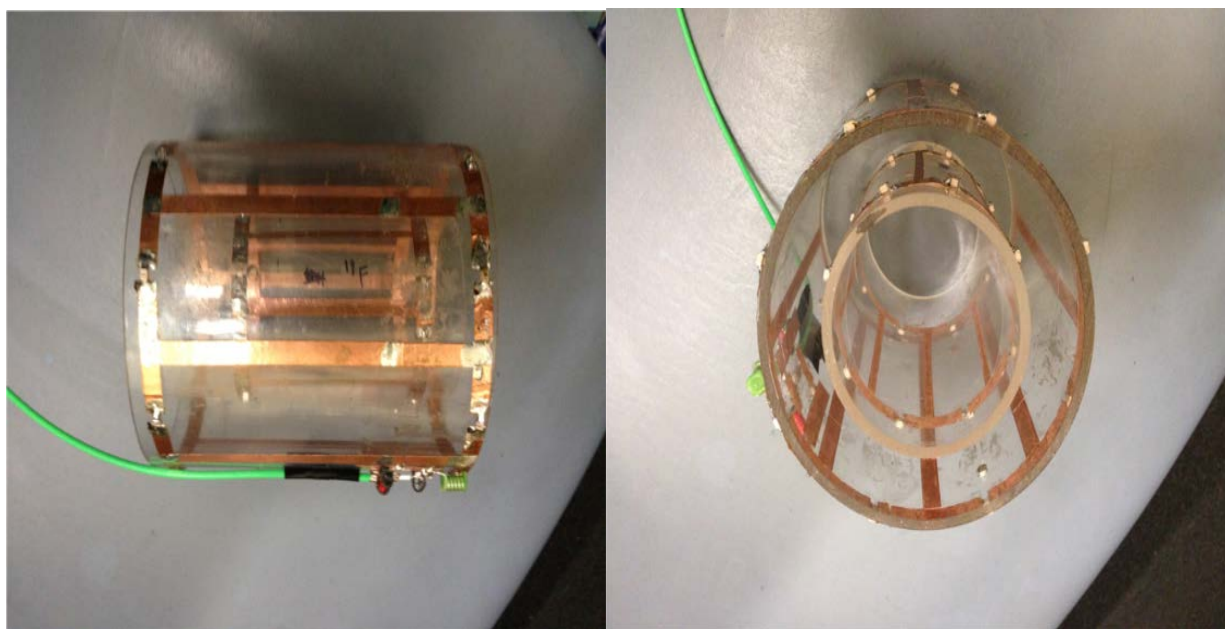


**Figure 3.2: Schematic of the double birdcage coil.**



(a)

(b)

**Figure 3.3: (a) Front view of the constructed  $^1\text{H}$ - $^{19}\text{F}$  double birdcage coil.**

**(b) Top view of the constructed  $^1\text{H}$ - $^{19}\text{F}$  double birdcage coil.**

### 3.3 Decoupling and Coil Isolation

Decoupling and coil isolation was performed by placing one coil inside the other and the  $^{19}\text{F}$  birdcage coil was rotated counter clockwise to the  $^1\text{H}$  coil, starting at the position where the coils are at 12 o'clock and proceeding with a step of  $\pi/8$  degrees. The isolation for both the frequencies was achieved at  $\pi/4$ . But Figure 3.4 shows that both frequencies are away from resonance indicating coupling effect.

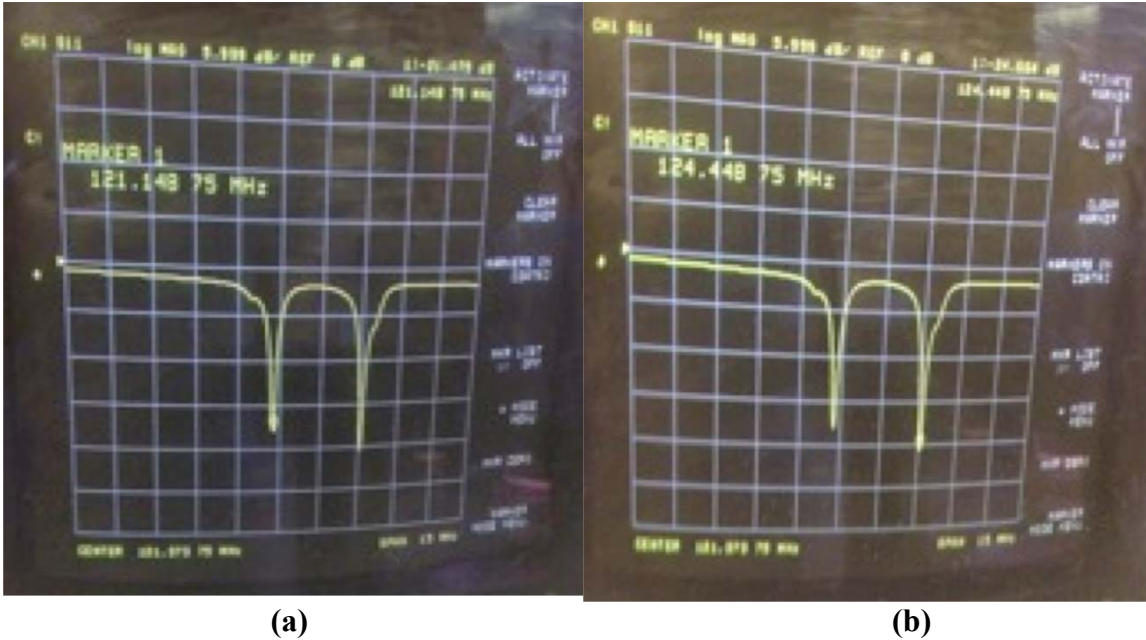


**Figure 3.4:** (a) S11 response for  $^{19}\text{F}$  achieved.  
(b) S11 response for  $^1\text{H}$  achieved.

### 3.4 Discussion

From the chapter, it is proven that the double birdcage coil using the coil inside coil approach is an ineffective method to decouple frequencies that are very close to each other. The closest frequency that can be achieved using the coil inside coil method for frequencies that are close together is tunings of 121.14 MHz for  $^{19}\text{F}$  which is off resonance (120.14MHz) and 124.4MHz for  $^1\text{H}$  (127.74MHz) which off resonance, resulting in high coupling between the two coils. This chapter was presented to show the simplest method that can be used for decoupling two birdcage coils. Although these

results were not ideal, they provide a starting point for testing alternative RF coil designs that might help to resolve the coupling issue when working with two close frequencies i.e.,  $^1\text{H}$  (127.74 MHz at 3T) and  $^{19}\text{F}$  (120.14 MHz at 3T).

## Chapter 4

### A $^{19}\text{F}$ - $^1\text{H}$ Linear Dual Tuned Birdcage Coil

#### 4.1 Introduction

In this chapter, a linear dual tuned  $T_X / R_X$  birdcage coil for rat lung imaging for  $^1\text{H}$  and  $^{19}\text{F}$  is presented. This chapter also discusses, frequency tuning, impedance matching and  $B_1$  field mapping of the coil. *In vivo* rat lung imaging results are also presented.

#### 4.2 $^{19}\text{F}$ and $^1\text{H}$ Coil Construction

An 8-rung birdcage coil was built with copper tape on the surface of a machined acrylic tube. The size was designed to optimize the filling factor for *in vivo* rat lung imaging experiments. The overall diameter of the acrylic tube used was 88.3 mm with an overall length of 97.6 mm. A high pass birdcage coil was made by placing 16 capacitors between the 8 units on the end rings of the coil. The width of the end rings and rungs of the coil were 6.3 mm. The detailed dimensions and materials of the coil are shown in Table 4.1

**Table 4.1:  $^{19}\text{F}$  and  $^1\text{H}$  Coil dimensions and materials.**

Nucleus	Frequency (MHz)	Coil Diameter (mm)	Leg Length (mm)	Copper Tape Width (mm)	Tuning Capacitors (pf)
$^1\text{H}$	127.74	88.3	97.6	6.3	32
$^{19}\text{F}$	120.15	88.3	97.6	6.3	36

The end ring tuning capacitors for  $^{19}\text{F}$  and  $^1\text{H}$  are calculated using birdcage builder software based on the Larmor frequency for a 3T field. The coil was initially built for  $^{19}\text{F}$ . All 16 capacitors (36 pF each as per Table 4.1) are placed on the coil. Two RF pickup probes that are already tuned to 120.15 MHz on a HP 8751A network analyzer were used to check for resonance frequency. Each end on the pickup probes was connected to

network analyzer; the other end of the pickup probes were placed across the birdcage coil checking for resonance through  $S_{21}$  response.

Once the coil was at resonance at 120.15MHz, one capacitor on one unit was changed to 32 pF (as per Table 4.1), tuning it to  $^1\text{H}$  (frequency of  $^1\text{H}$  is 127.74 MHz at 3T). The RF pickup probes were used to check  $^1\text{H}$  resonance frequency. Figure 4.1 represents the structure of the coil and also shows where the  $^{19}\text{F}$  and  $^1\text{H}$  channels are taken. Figure 4.2 shows the coil constructed using the Table 4.1

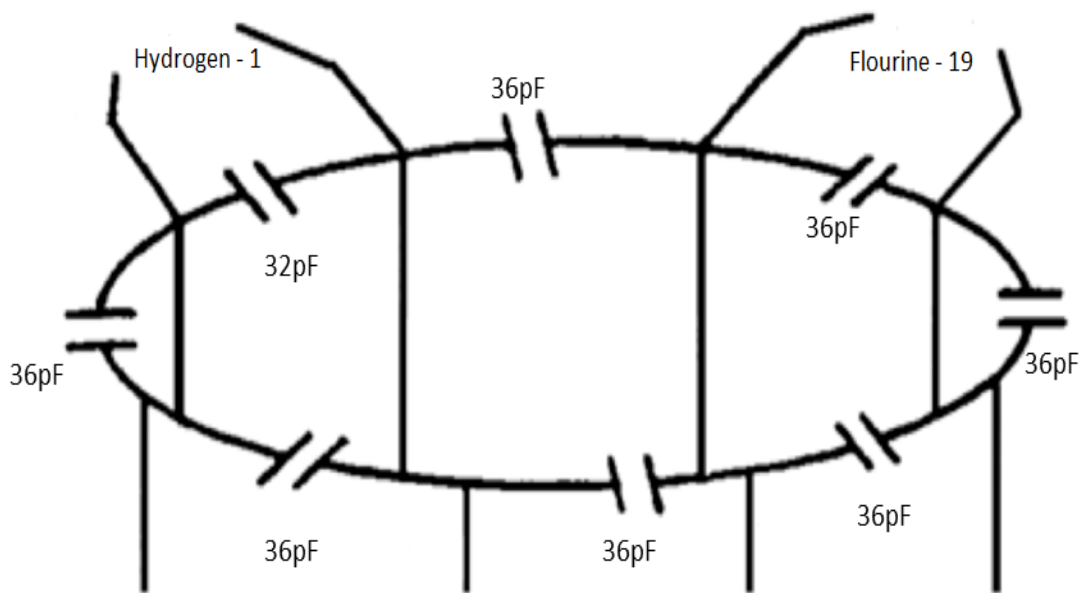


**Figure 4.1: Structure of Linear dual tuned coil.**

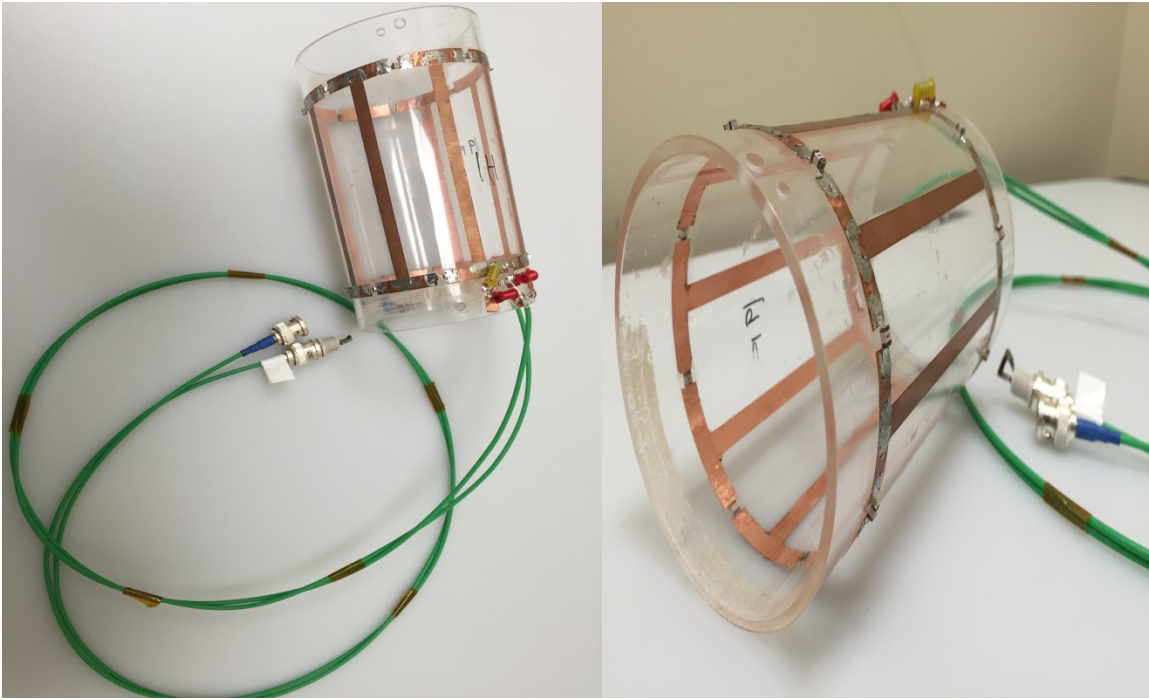


**Figure 4.2: Constructed  $^{19}\text{F}$  -  $^1\text{H}$  birdcage coil**

### **4.3 Impedance Matching**

To minimize power reflection, impedance of the coil at the input/output ports has to be matched. Matching can be performed in many different ways where the input impedance is transformed to a desired value. In this thesis, L-C Balun (Lattice Balun) circuits were used to match the two ports to  $50\Omega$  impedance.

A balanced to unbalanced (Balun) circuit is a coupler that connects symmetric to asymmetric circuits providing a 180 degree phase shift between input and output signals. The schematic figure of a Balun is showed in Figure 4.3.

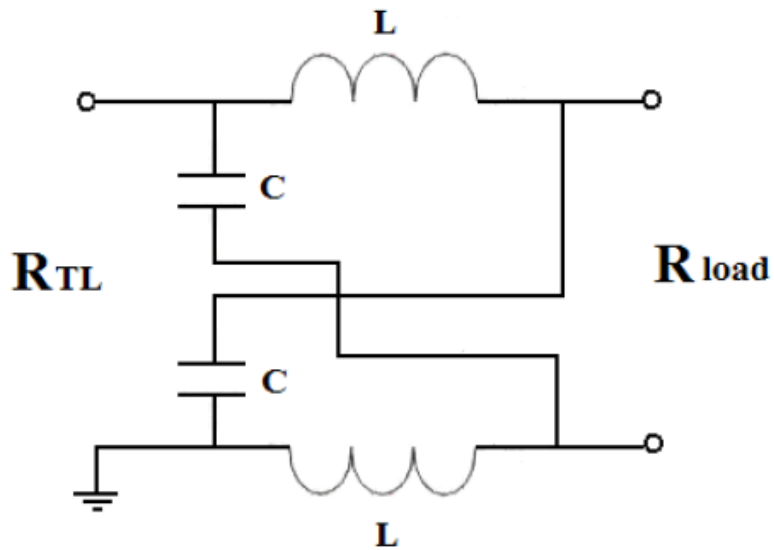


**Figure 4.3 Schematic of an L-C Balun**

$R_{TL}$  – Impedance of a Transmission Line.

$R_{Load}$  - Impedance of a balanced Load.

The components of L and C can be calculated using these equations at a certain frequency  $\omega$ , defining

$$Z_0 = \sqrt{R_{TL} R_{Load}} \quad (4-1)$$

and then

$$L = \frac{Z_0}{\omega} \quad (4-2)$$

$$C = \frac{1}{Z_0 \omega} \quad (4-3)$$

Table 4.2 shows the measured input impedance at each port.

**Table 4.2: Measured impedance for <sup>1</sup>H and <sup>19</sup>F.**

Frequency	<sup>1</sup> H	<sup>19</sup> F
Measured Impedance ( $Z_{in}$ )	564-j40.3	973.6-j36.2

It is important to cancel out the reactance and make it a pure resistive. This was achieved by placing two inductors in series with the load making it pure resistive.

The L and C values for  $^{19}\text{F}$  and  $^1\text{H}$  are calculated using the above equations (4-2) and (4-3) at Larmor frequencies 120.15MHz and 127.74MHz. For  $^{19}\text{F}$ , the L1 was calculated as 209.2 nH and C1 was calculated as 7.4 pF. The L2 (inductor in series with the load) was calculated as 40.3 nH. For  $^1\text{H}$ , L1 was calculated as 292.2 nH and C1 was calculated as 6.0 pF and L2 (inductor in series with the load) was calculated as 36.2 nH. Figure 4.4 represents the  $^{19}\text{F}$  and  $^1\text{H}$  channels taken on the coil.

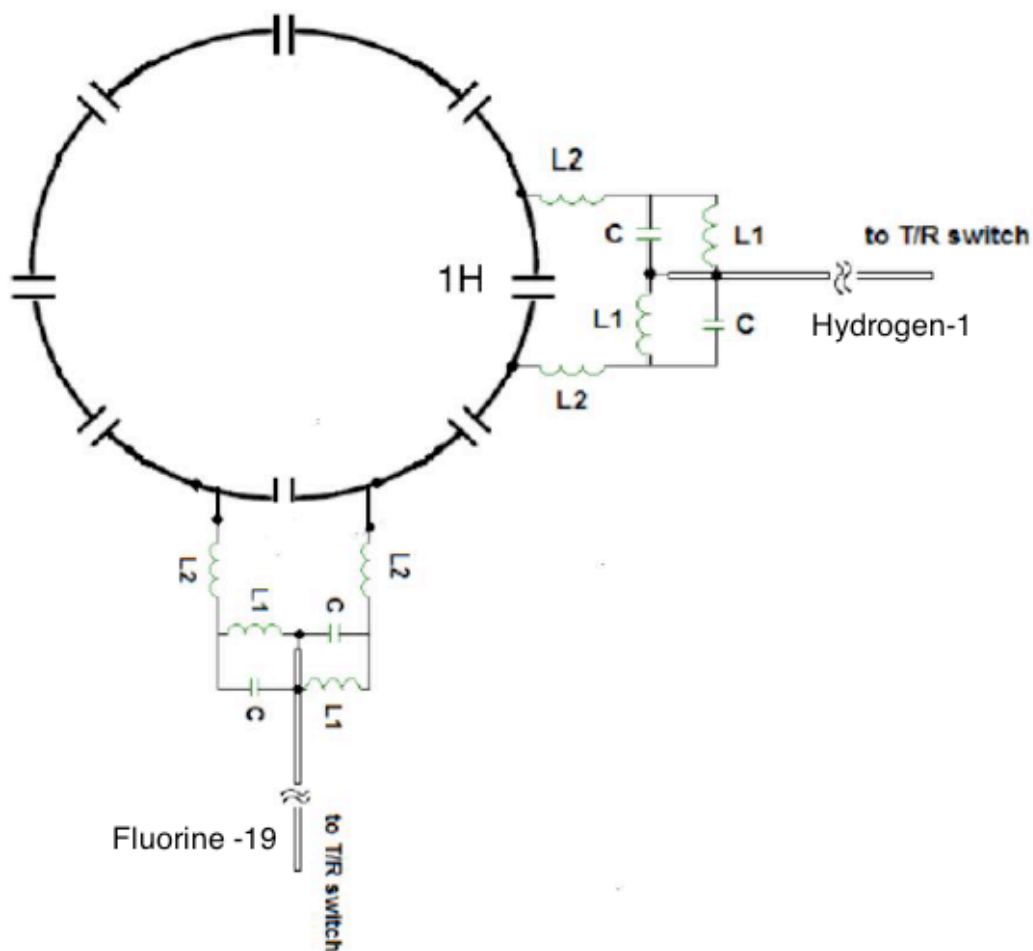


**Figure 4.4 Schematic of a linear dual tuned birdcage coil with  $^{19}\text{F}$  and  $^1\text{H}$  channels.**

The performance of the coil was investigated by connecting the two ports to the network analyzer and  $S_{11}$  measurements were performed to check for resonance. As well,  $S_{21}$  measurements were also performed to investigate the coupling effect. Figure 4.5 shows the  $S_{11}$  and  $S_{21}$  response of the coil.

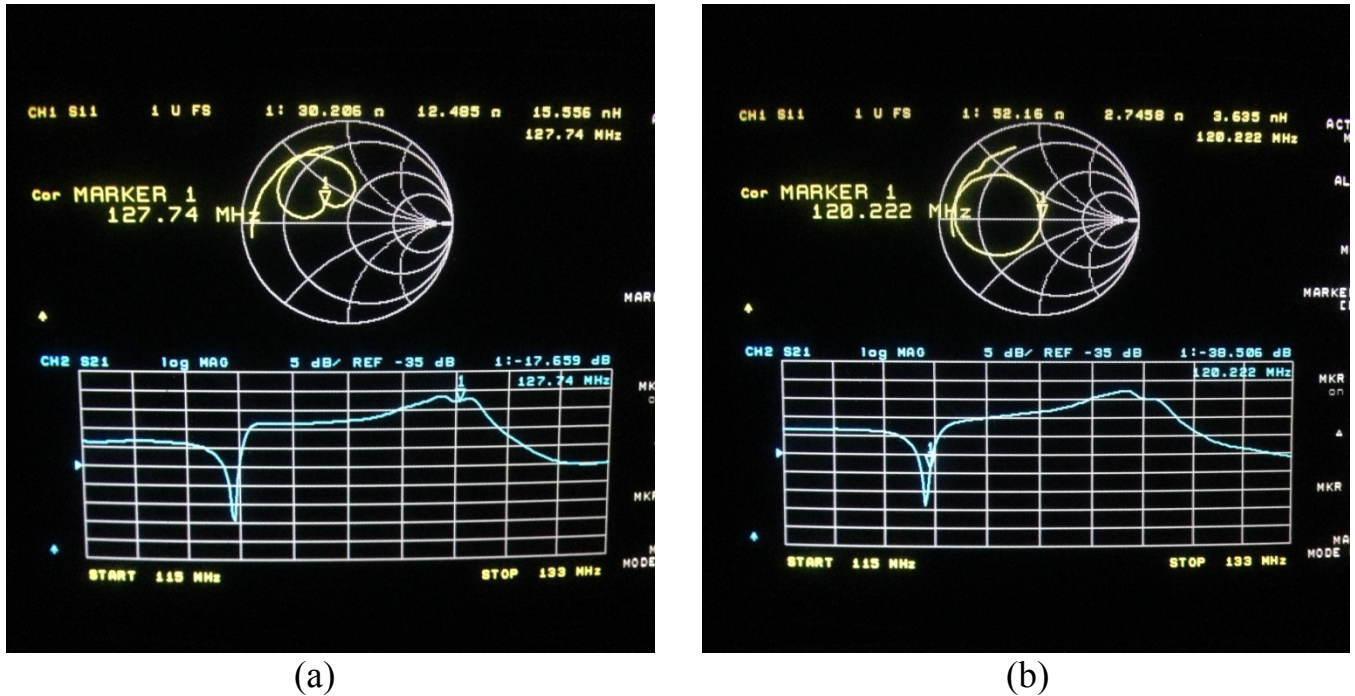


Figure 4.5 : (a) Smith chart represents the  $S_{11}$  and the log map represents  $S_{21}$  response for  $^1\text{H}$  at 127.74 MHz (b) Smith chart represents  $S_{11}$  and the log map  $S_{21}$  response for  $^{19}\text{F}$  at 120.15 MHz.

#### 4.4 Results

An initial bench test was performed to measure the impedance and the Q factor for both the channels. Loaded Q for  $^{19}\text{F}$  and  $^1\text{H}$  was measured as 227 and 181 and unloaded Q for  $^{19}\text{F}$  and  $^1\text{H}$  was measured as 402 and 276 (Refer to equation 2-11). From Figure 4.5 the smith chart shows  $S_{11}$  response and log map shows the  $S_{21}$  response. The  $S_{21}$  from Figure 4.5 shows the isolation,  $^1\text{H}$  and  $^{19}\text{F}$  channels were -17db and -38db respectively.

After the bench test was performed and it was determined that the coil met the basic requirements, it was placed inside a Philips Achieva 3T scanner to check the response of  $S_{11}$ . A fine re-tuning was performed as the magnetic field shifts the resonance frequency. MR spectroscopy and imaging scans were performed using a phantom. The coil was calibrated by performing various multi flip angle spectroscopic scans for getting a 90-degree excitation pulse by adjusting the scanner output power.

#### 4.4.1 Phantom Spectroscopic Scan Results

Two phantoms were made for both nuclei using 30ml and 60ml syringes. The  $^{19}\text{F}$  phantom was prepared by sealing 12ml of sulfur hexafluoride ( $\text{SF}_6$ ) in a 60ml syringe. The  $^1\text{H}$  phantom was prepared by sealing 10ml of mineral oil in a 30ml syringe shown in Figure 4.6. While performing the scans, these syringes were placed inside a hollow foam cylinder. This was then placed in the middle of the coil where the most homogeneous  $B_1$  field was generated.

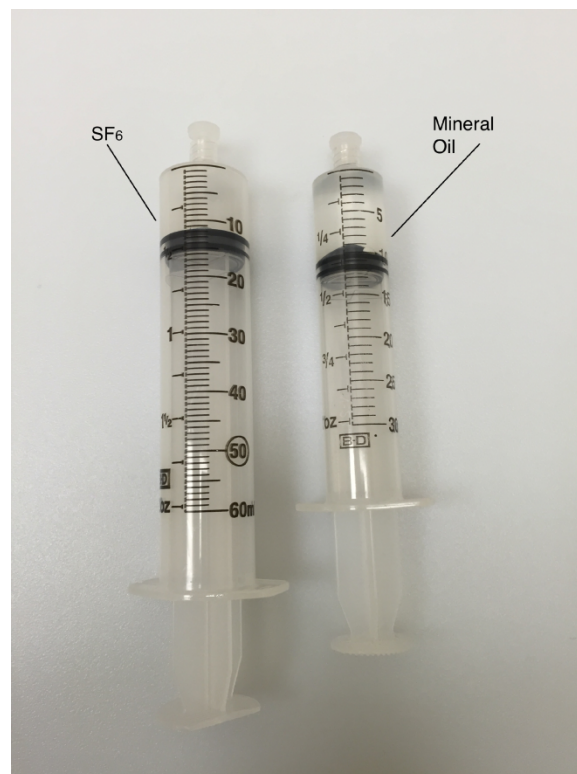


**Figure 4.6: Two syringe phantoms filled with sulfur hexafluoride ( $\text{SF}_6$ ) and mineral oil.**

The coil was connected to a dual frequency gateway (DFG) for the  $^1\text{H}$  phantom test: the end of the  $^{19}\text{F}$  channel was connected to a  $50\ \Omega$  terminal while performing  $^1\text{H}$  scans. The cables were switched, with  $\text{SF}_6$  phantom placed inside the coil and the  $^{19}\text{F}$  channel cable connected directly to the linear transmit/receive switch. A non-selective pulse sequence was performed for a spectroscopic scan using TR of 4 ms and TE of 0.85 ms. Total power of 128 W was required to calibrate the  $^1\text{H}$  and  $^{19}\text{F}$  channels using phantoms. Figure 4.7 shows the coil calibration for  $^{19}\text{F}$ .

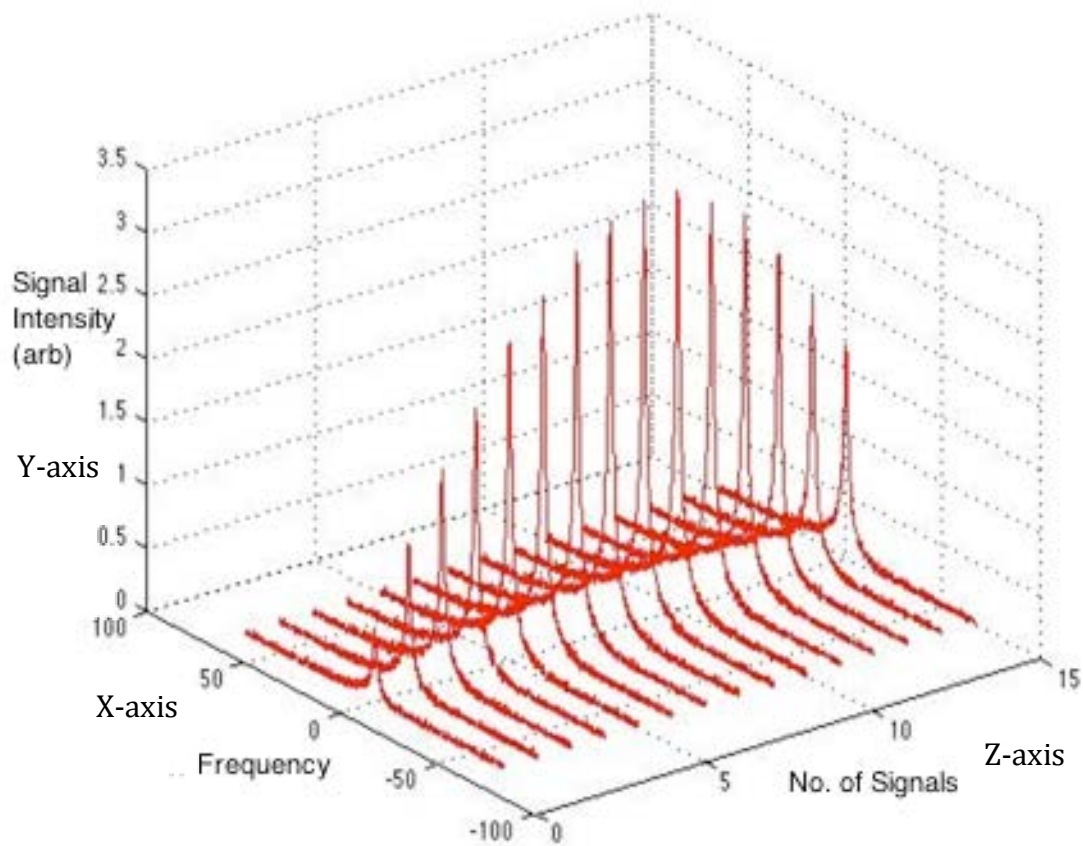


**Figure 4.7: The  $^{19}\text{F}$  coil calibration, showing the signal response as a function of increasing power, where the 90-degree RF pulse yields the highest possible signal.**

The x-axis in Figure 4.7 represents the frequency, the y-axis represents the signal intensity, and the z-axis represents the number of signals where each pulse is excited until the maximum signal achieves a 90-degree excitation pulse. Figure 4.8 (a) shows the FID

signal, which decays as expected due to transverse relaxation. Figure 4.8 (b) shows the Fourier transform of the FID signal, and the center peak indicates the  $^{19}\text{F}$  resonance.

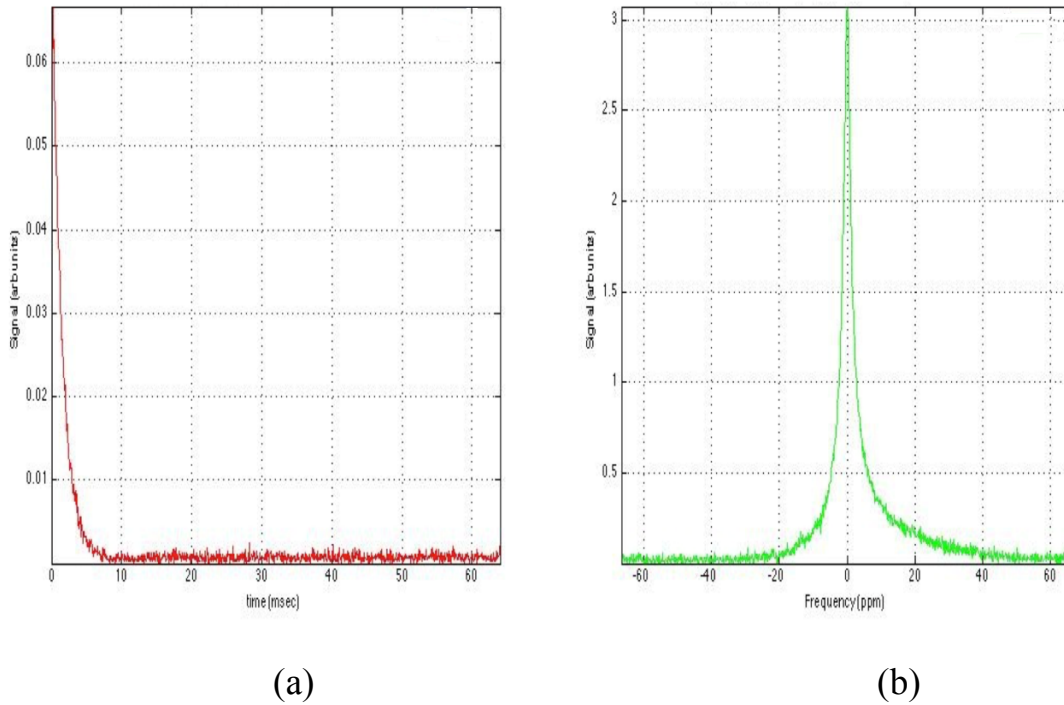


**Figure 4.8: (a) FID signal (b) Spectrum response of the coil.**

#### 4.4.2 Phantom Imaging Scan Results

Phantom scans were performed using the linear birdcage coil for  $^1\text{H}$  and  $^{19}\text{F}$ . A 2D gradient echo pulse sequence was used to acquire transverse and coronal images. Table 4.2 shows all the different parameters used to achieve  $^1\text{H}$  and  $^{19}\text{F}$  phantom images and transverse and coronal phantom images for  $^1\text{H}$  and  $^{19}\text{F}$  are shown in Figure 4.9.

**Table 4.3: Pulse sequence parameters used for  $^1\text{H}$  and  $^{19}\text{F}$  phantom imaging.**

<b>Nucleus</b>	<b>FOV (mm x mm)</b>	<b>TR (ms)</b>	<b>TE (ms)</b>	<b>NSA</b>	<b>B<sub>1</sub></b>	<b>Matrix Size</b>	<b>SNR</b>
$^{19}\text{F}$	75 x 75	4	0.85	30	70	64 x 64	167
$^1\text{H}$	75 x 75	2000	55.19	1	70	256 x 256	474

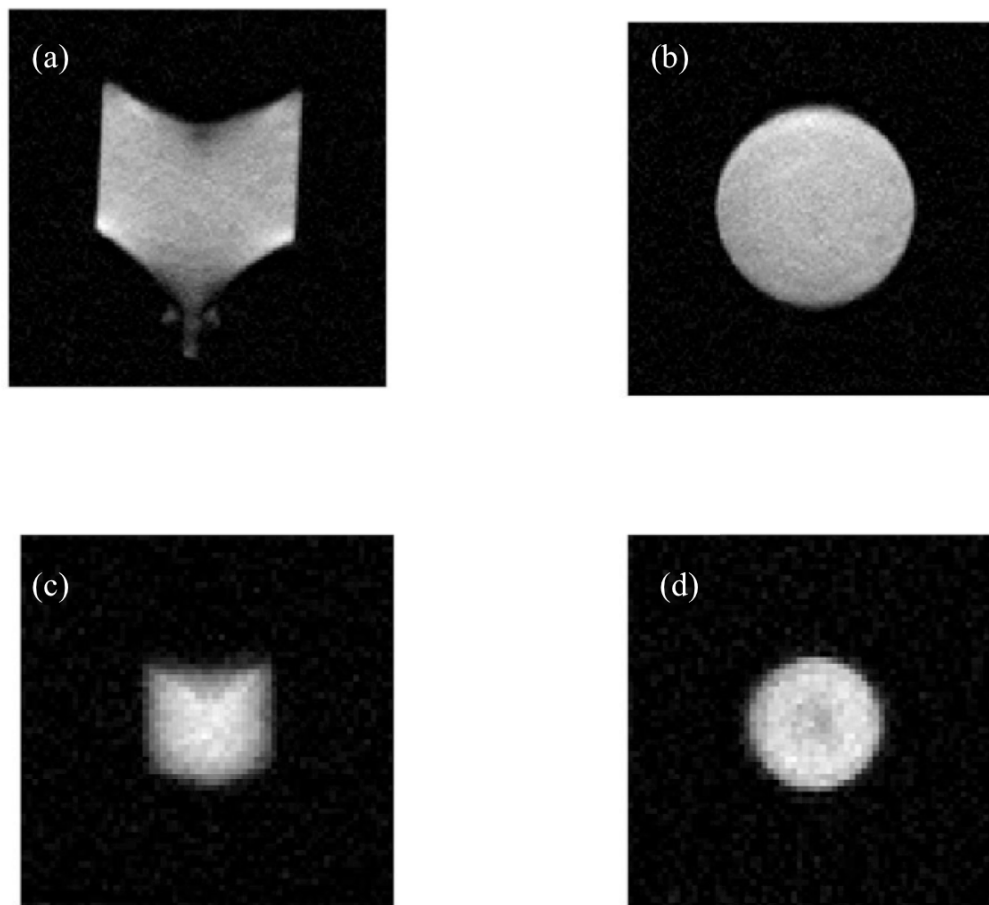


**Figure 4.9 : (a)  $^1\text{H}$  Coronal image with Mineral oil.  
(b)  $^1\text{H}$  Transverse image with Mineral oil.  
(c)  $^{19}\text{F}$  Coronal image with  $\text{SF}_6$ .  
(d)  $^{19}\text{F}$  Transverse image with  $\text{SF}_6$ .**

### 4.4.3 B<sub>1</sub> Field Mapping and Field Homogeneity

The B<sub>1</sub> field homogeneity is the most essential measurement to check the performance of a transmit coil. B<sub>1</sub> field can be measured and mapped using several NMR techniques. In this study, <sup>1</sup>H B<sub>1</sub> field mapping was performed using dual-TR method using a 30 mL syringe of mineral oil, and <sup>19</sup>F B<sub>1</sub> field mapping<sup>[45][46][47]</sup> was performed using dual angle method (DAM)<sup>[48][49F]</sup> with a 30 mL syringe of sulfur hexafluoride (SF<sub>6</sub>). To excite the magnetization, two RF pulse are used with a flip angle of  $\alpha$  and  $2\alpha$ . Two FID signals are acquired by a set of long repetition time (TR>>T<sub>1</sub>) between two scans.

B<sub>1</sub> mapping for <sup>1</sup>H and <sup>19</sup>F are performed individually by placing a phantom of mineral oil for <sup>1</sup>H, and SF<sub>6</sub> for <sup>19</sup>F. The <sup>19</sup>F B<sub>1</sub> mapping scan was performed on a slice thickness of 30mm at the center of the coil with a flip angle of  $\alpha$  of 45 degrees and  $2\alpha$  of 90 degrees using SF<sub>6</sub>. A B<sub>1</sub> field map was obtained by selecting a region 15x15mm at the center. The mean normalized B<sub>1</sub> for <sup>19</sup>F channels ( $\pm$  standard deviation) was calculated as  $0.80 \pm 0.13$ . Figure 4.10.1 shows the normalized B<sub>1</sub> plot of the birdcage coil and Figure 4.9.2 shows the B<sub>1</sub> histogram and B<sub>1</sub> field graph at the center of the coil.

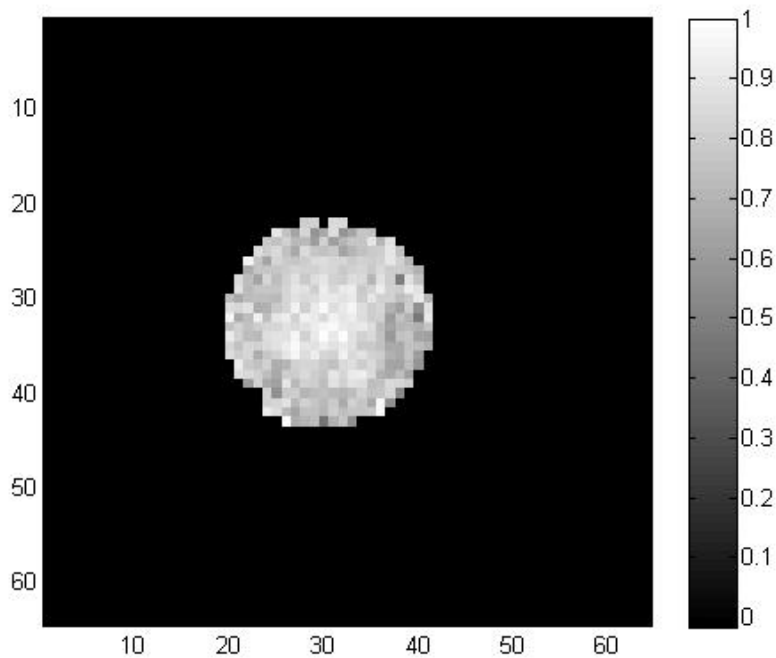
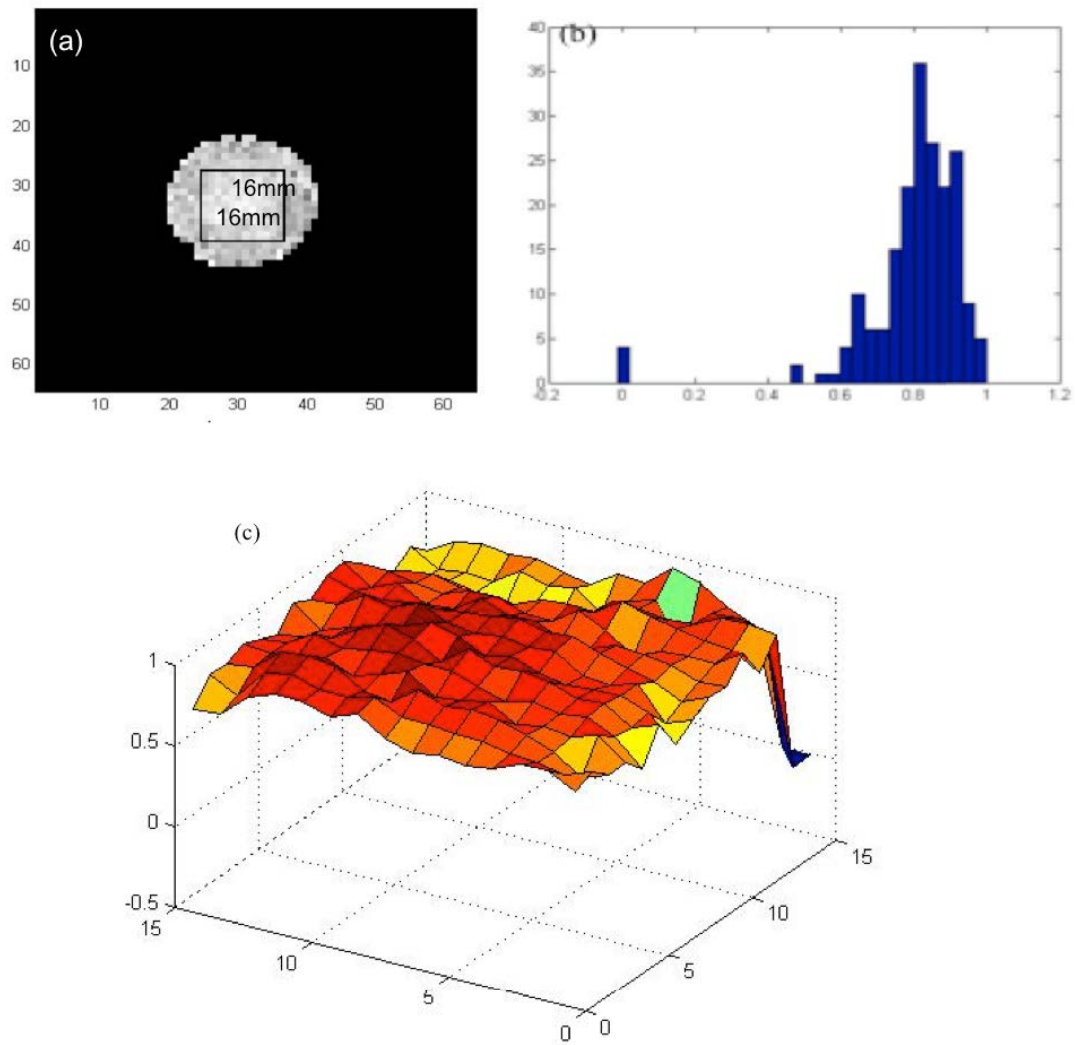
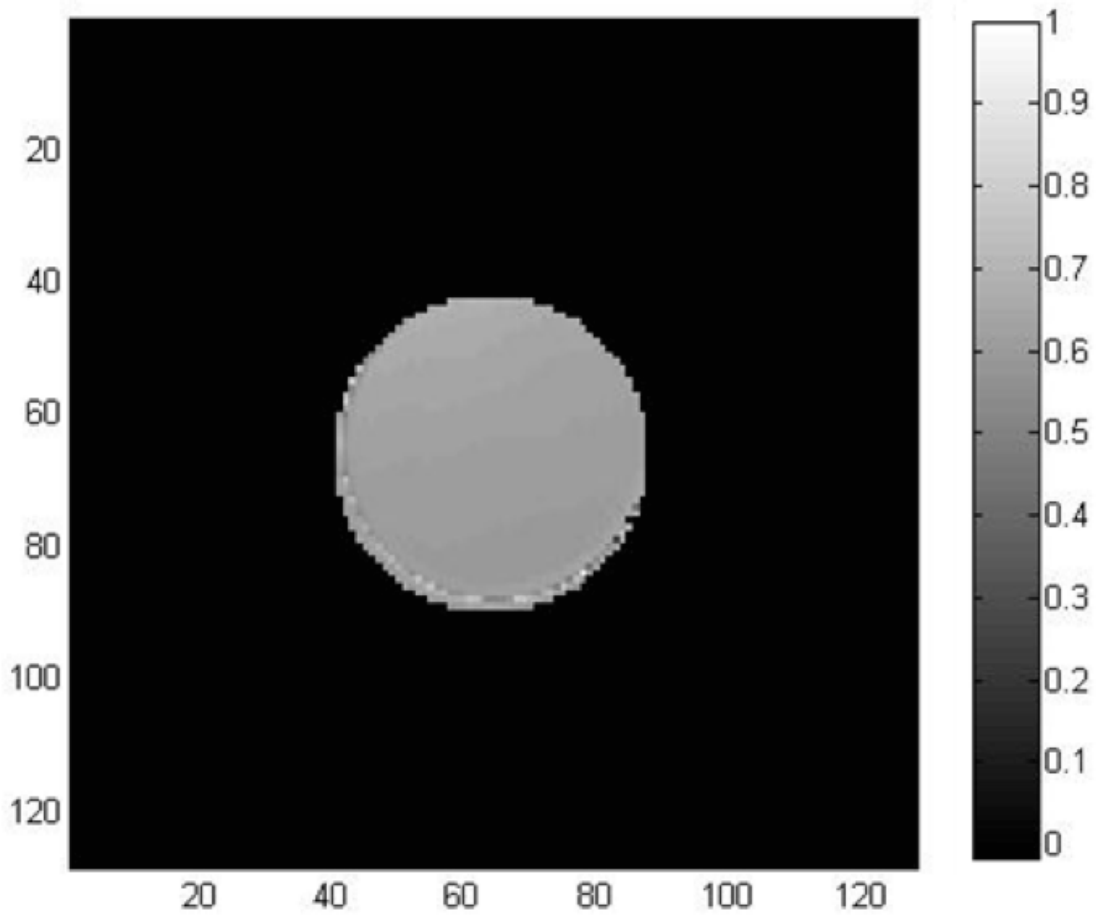


Figure 4.10.1 shows the normalized B<sub>1</sub> for <sup>19</sup>F



**Figure 4.10.2 : (a)  $B_1$  map with the area of 15x15x30mm of  $^{19}\text{F}$ .  
 (b) Histogram of the  $B_1$  of the coil generated by (a).  
 (c)  $B_1$  field graph for  $^{19}\text{F}$ .**

The  $^1\text{H}$   $B_1$  mapping scan was performed on a slice thickness of 20mm at the center of the coil with a  $\text{TR}_1$  of 150 ms and a  $\text{TR}_2$  of 300 ms. The mean normalized  $B_1$  for  $^1\text{H}$  channels ( $\pm$ standard deviation) was calculated as  $0.94 \pm 0.19$ . Figure 4.10.3 shows the normalized  $B_1$  of the birdcage coil.



**Figure 4.10.3 : Normalized  $B_1$  map for  $^1\text{H}$ .**

An area of 16 x 16 mm was selected at the center of the coil to generate the  $B_1$  histogram and  $B_1$  map at the center of the coil. Figure 4.10.4 represents the  $B_1$  histogram and  $B_1$  map.

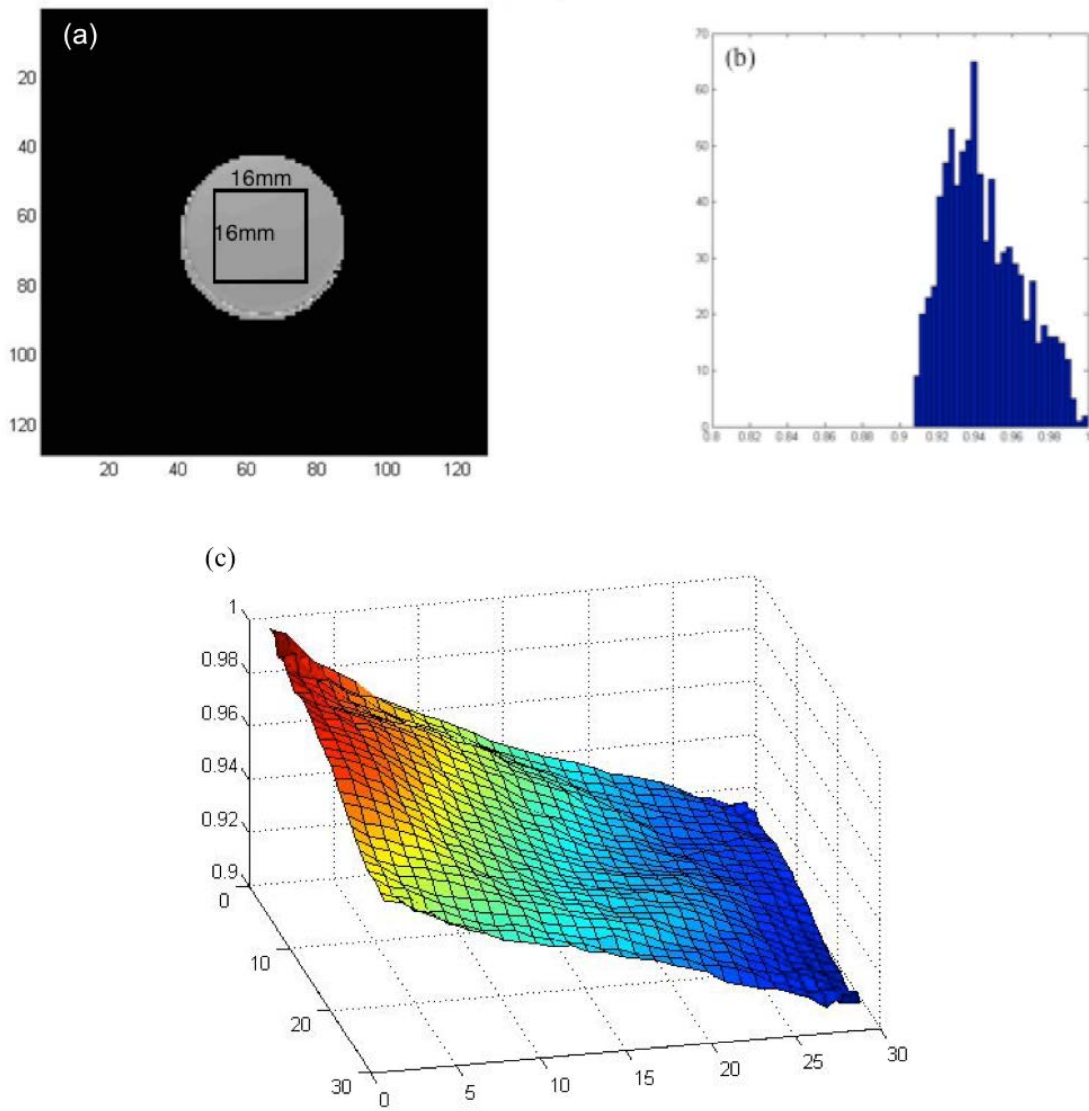


**Figure 4.10.4 : (a)  $B_1$  map with the area of 16x16x20 of  $^1\text{H}$ .  
(b) Histogram of the  $B_1$  of the coil generated by (a).  
(c)  $B_1$  field graph for  $^1\text{H}$ .**

#### 4.4.4 Animal *in vivo* Results

*In vivo*, rat lung imaging was performed under an animal approved by the animal care committee (ACC) of Lakehead University. A healthy male Sprague-Dawley rat was anesthetized and imaged using the Philips 3T Achieva scanner. Using a home built ventilator, the rat was continuously ventilated with a mixture 80% SF<sub>6</sub> and 20% O<sub>2</sub>. The <sup>1</sup>H images were acquired during a 5 minute scan and <sup>19</sup>F images were acquired during a 3.41 minute scan using a 3D gradient echo pulse sequence.

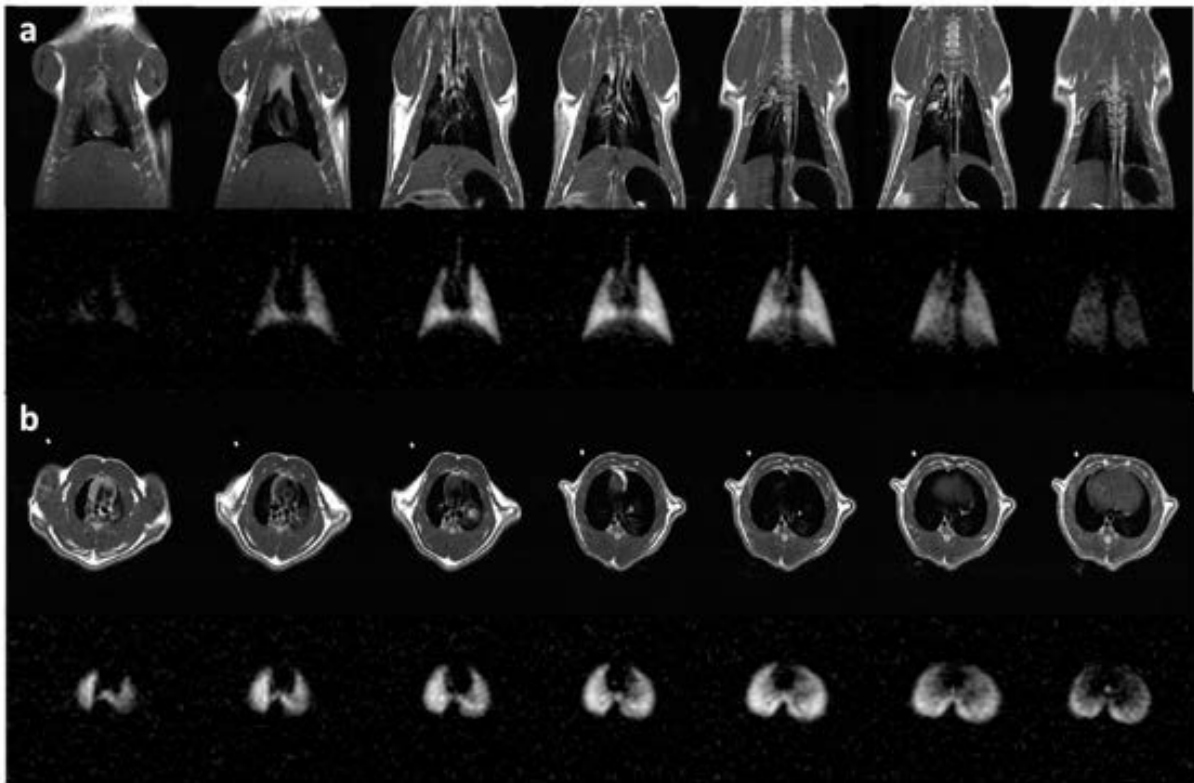


**Figure 4.11 : (a) First row of images represents the coronal images on <sup>1</sup>H and second row represents coronal images of <sup>19</sup>F. (b) First row of images represents the transverse images on <sup>1</sup>H and second row represents transverse images of <sup>19</sup>F.**

## 4.5 Discussion

The completed linear dual tuned  $^{19}\text{F}$  and  $^1\text{H}$  birdcage coil has exhibited satisfactory electrical performance as well as good  $B_1$  field homogeneity for both nuclei. Coil sensitivity and field homogeneity were quantitatively measured. The spectroscopy scans show the sensitivity of the coil. The SNR for both the nuclei was obtained.

Sufficient isolation was achieved between the two channels to minimize the coupling effect. This coil structure eliminates the need for active decoupling of components and circuits, and greatly reduces the complexity of dual-tuned coil construction.  $B_1$  field mapping shows the homogeneity of the coil and the  $B_1$  field mapping shows the homogeneous field is at the center of the coil.

*In vivo* rat lung imaging was performed and the coil showed very good suitability in terms of dimensions and the filling factor. The rat was placed in the coil such that its lungs were at the center of the coil with the most homogeneous field.

## Chapter 5

### A $^{19}\text{F}$ - $^1\text{H}$ Quadrature Dual Switch Tuned Birdcage Coil

#### 5.1 Introduction

The scope of this thesis is to ultimately build a quadrature birdcage coil for  $^{19}\text{F}$  &  $^1\text{H}$  which gives higher SNR with good  $B_1$  field homogeneity. Chapter 4, showed that a birdcage coil with two resonant frequencies can be built, however, the disadvantage of that coil is that it is only a linear mode dual tuned birdcage coil. From Chapter 2 it is evident that SNR can be increased by factor of root two by building the birdcages coils to quadrature modes.

In our final approach, a switch-tuned quadrature coil was built that can be switched to resonant at either the  $^1\text{H}$  or  $^{19}\text{F}$  frequencies. PIN diodes are used to actively control the switching between the two frequencies. Theoretically this method enables to achieve a higher SNR by a factor of  $\sqrt{2}$ . The dual tuned coils have the advantage of switching frequencies on the fly without having to physically change of coils and move samples, animals, or patients from their anatomically localized positions.

In this chapter, the construction of the coils,  $B_1$  field homogeneity, phantom results and comparison of linear dual tuned to quadrature dual tuned are presented.

#### 5.2 Coil Construction and Switching Circuit

##### 5.2.1 Coil Construction

On a machined acrylic tube, an 8-rung birdcage coil was built with copper tape on the surface of it. The overall diameter of the acrylic tube that used was 88.3 mm with an overall length of 193mm. A high pass birdcage coil was made by placing 16 capacitors between the 8 units on the end rings of the coil. The width of the end rings and rungs of the coil were 6.3 mm. The initial coil was constructed to be a proton coil, by placing 4-switched circuits consisting of capacitors and a diodes the coil was switched to fluorine.

Section 5.2.2 discusses the switching circuit. The detailed dimensions and materials of  $^1\text{H}$  coil are shown in the table 5.1. The values of the capacitor are shown in the Figure 5.2

**Table 5.1 Coil dimensions and materials**

Leg Length (mm)	Copper Tape Width (mm)	Coil Diameter (mm)
97.4	0.64	44.2

The four circuits are placed on the coil at  $0^\circ$ ,  $90^\circ$ ,  $180^\circ$ , and  $270^\circ$ . Along with these capacitors a PIN diode is placed to actively switch between the two frequencies. Figure 5.1 shows the structure of the quad coil.

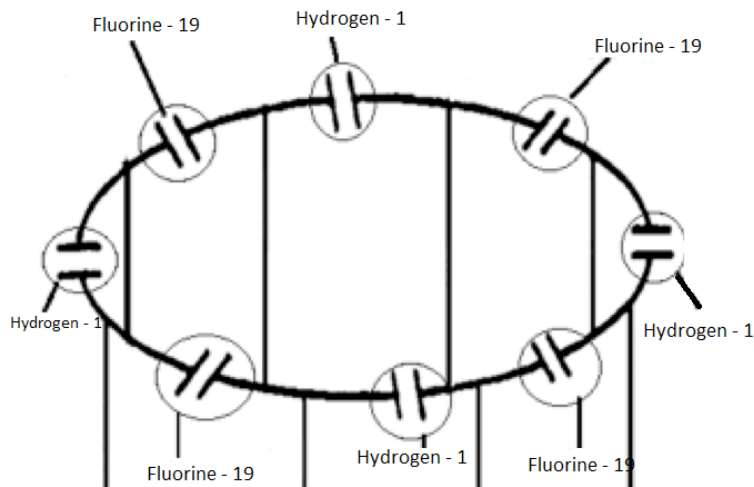


**Figure 5.1 Structure of the quadrature coil.**

Figure 5.2 is an illustration of the coil circuit with the  $^{19}\text{F}$  circuits. Figure 5.3 shows a  $^1\text{H}$ - $^{19}\text{F}$  constructed quadrature dual tuned coil.

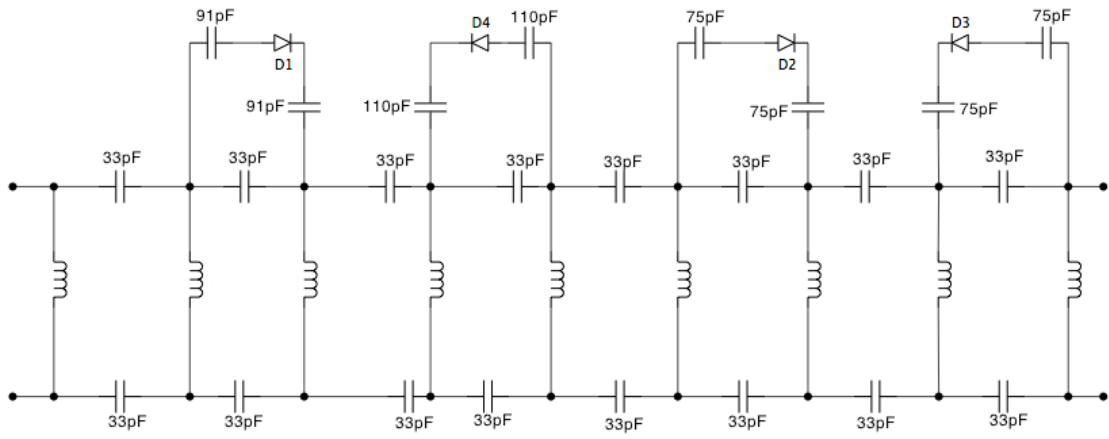
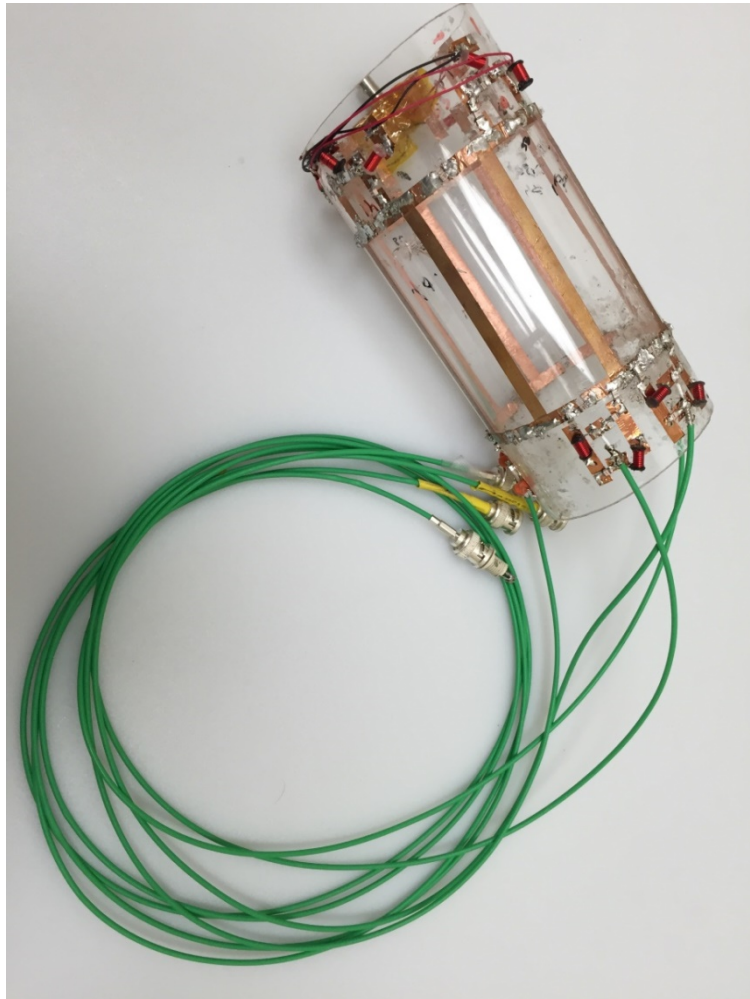
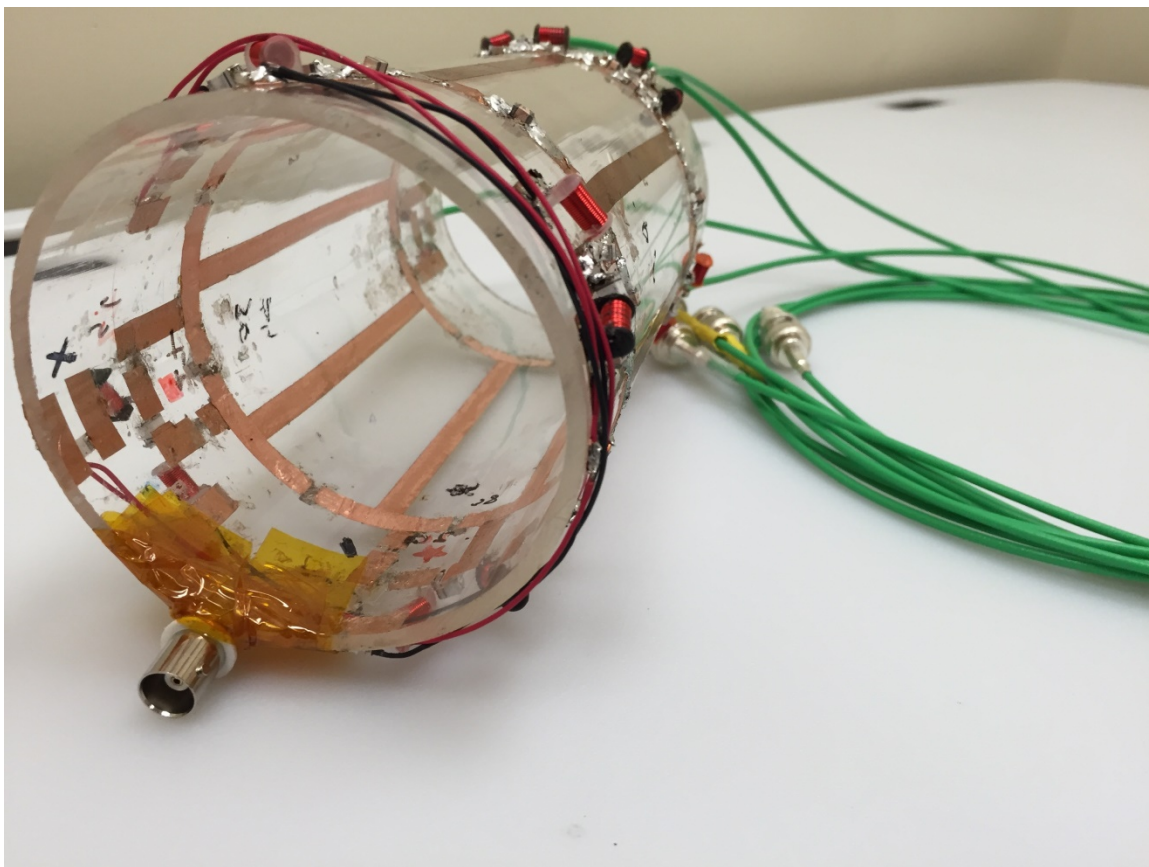


**Figure 5.2 Illustration circuit of the coil.**



**(a)**



(b)

**Figure 5.3 (a) Top view and (b) Front view of  $^1\text{H}$ - $^{19}\text{F}$  constructed quadrature dual tuned birdcage coil.**

### 5.2.2 Switching Circuit

From Figure 5.2, capacitors from C1 to C6 are added in series with capacitors on the coil ( $^1\text{H}$  capacitors) making the coil  $^{19}\text{F}$  sensitive. PIN diodes (D1 to D4) are used to actively switch the coil from  $^1\text{H}$  to  $^{19}\text{F}$ . Figure 5.4 shows the switching circuit.

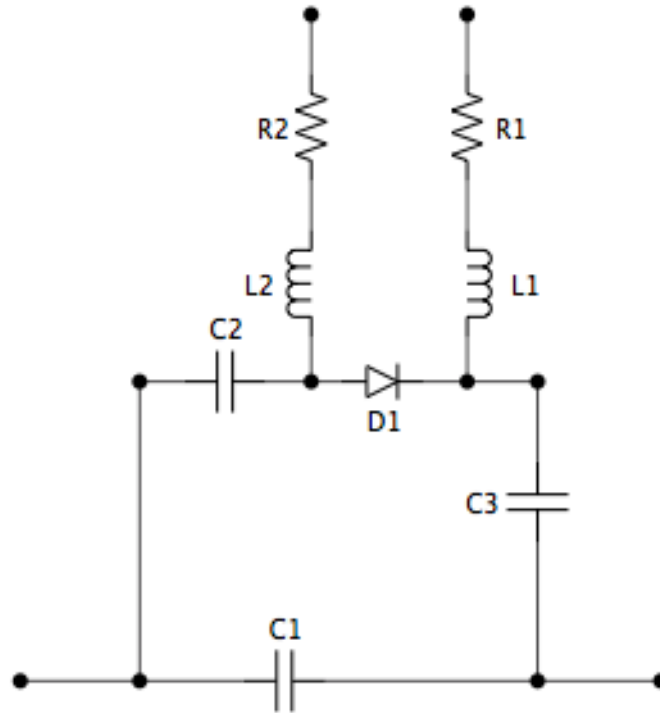
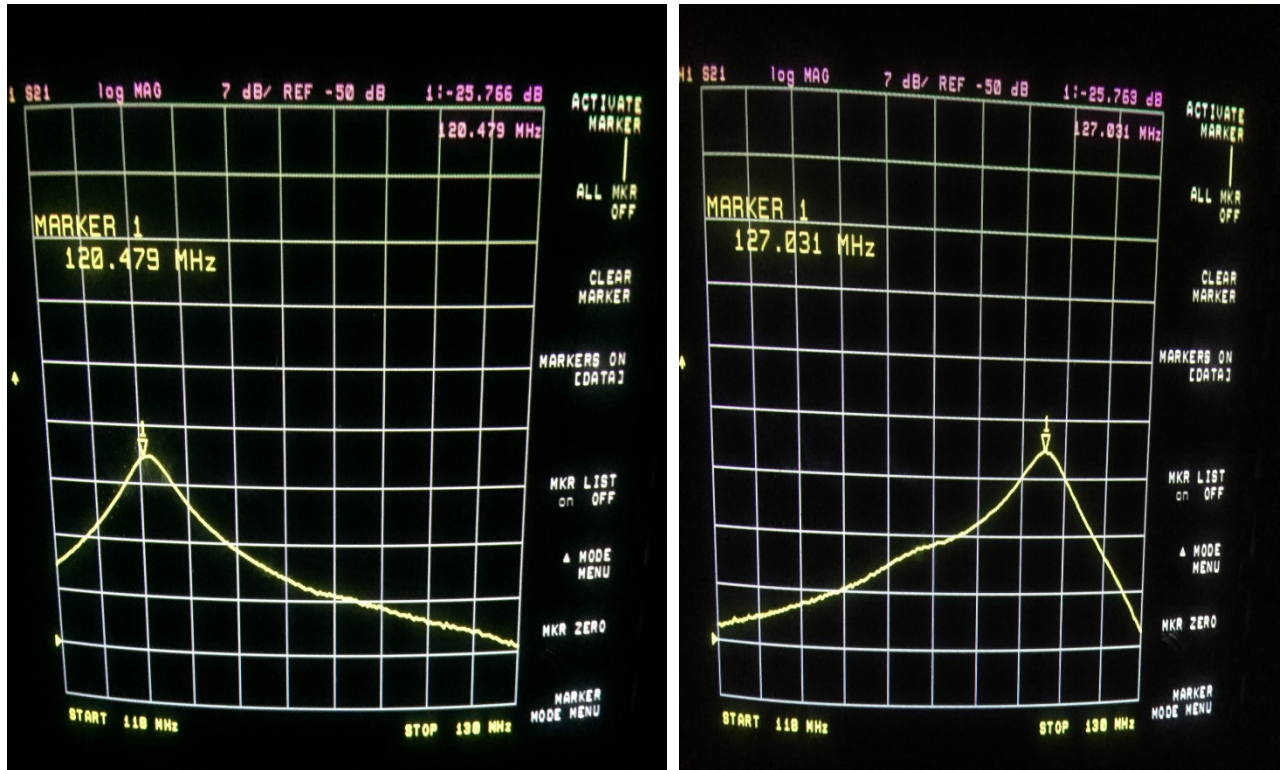


**Figure 5.4 Illustrated switching circuit used to switch from  $^1\text{H}$  to  $^{19}\text{F}$**

From Figure 5.4, C1 is the capacitor on the coil for  $^1\text{H}$ . C2 and C3 are the capacitors added to switch to  $^{19}\text{F}$ . C3 isolates the circuit from the coil (ground from the DC is not connected to the  $^1\text{H}$  resulting in change of impedance while placing a BALUN) while the diodes are at OFF state. D1 is the PIN Diode used to actively switch the coil between  $^1\text{H}$  to  $^{19}\text{F}$ . 1000 nH inductors L1 and L2 are used to suppress any RF signal while supplying voltage to the diodes. R1 and R2 are 100 $\Omega$  resistors used as current limiting resistors. 92mA of current is supplied to ON each diode. An overall current of 367 mA is used to turn ON four diodes on the capacitor switching  $^1\text{H}$  to  $^{19}\text{F}$ .

A voltage of -100V is applied to turn OFF the diodes while working with  $^1\text{H}$ . This high negative voltage is required to turn OFF the diodes, since the RF pulses and gradients from the MRI may introduce voltage across the PIN diodes which could turn ON the diodes. A voltage of 10 V is applied to turn ON the diodes while working with  $^{19}\text{F}$ . Figure 5.5 shows the  $S_{21}$  represents the resonance mode and also the RF switching between  $^1\text{H}$  and  $^{19}\text{F}$  when the diodes are at ON and OFF state. .



(a)

(b)

Figure 5.5 : (a)  $S_{21}$  response for  $^{19}\text{F}$  when diodes are at ON state.

(b)  $S_{21}$  response for  $^1\text{H}$  when diodes are at OFF state.

### 5.3 Quadrature Mode

Earlier RF-coils for MRI were built using a linear modality. In this configuration, both transmission and reception took place along a single axis. When the RF pulse is fed through a single port in linear mode, a linear polarized  $B_1$  field is generated. The linear oscillating field can be decomposed into two counter-rotating circular fields, one in the same direction and frequency as the NMR spin system, and the other in the opposite direction. The opposite rotating field does not contribute at all with the spins, leading to wastage of power. In the transmit mode linear polarized coils are inefficient such that half their power is wasted, and thus while receiving, they are incapable of extracting full phase information from the MR signal.

Alternatively, in the quadrature mode, a coil can be fed with two signals that have a  $90^\circ$  phase shift, creating a circular polarized magnetic field. During the excitation, the field rotates in the same direction with the spin precessions. The quadrature coil will have half the power requirement for the excitation compared to the linearly polarized field generated by linear mode.

While receiving the signal, the two outputs from the quadrature mode will be combined, resulting in an increase of the signal intensity by a factor of square root two. Figure 5.6 shows the linear and quadrature modes.

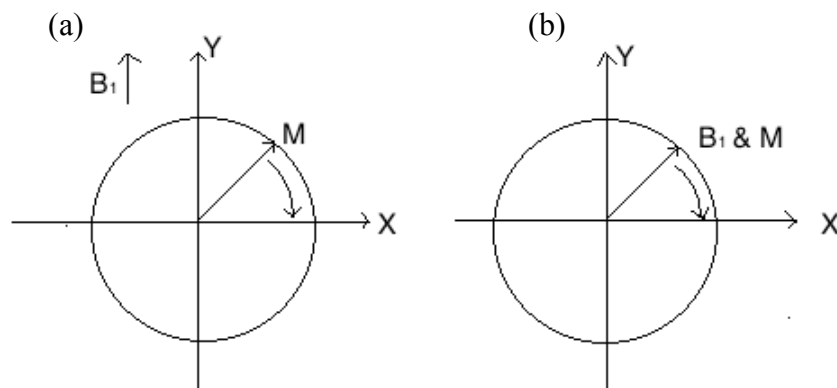


**Figure 5.6 (a) linear mode where  $B_1$  field pointing in one direction (b) Quadrature mode where  $B_1$  field rotating in the same direction.**

## 5.4 Impedance Matching

Impedance matching was performed as discussed in the chapter 3. In the quadrature dual tuned coil, four balun's were used. The reactance (imaginary part) is eliminated by placing an inductor between the coil and balun. On this dual tuned coil the reactance is eliminated by placing a high capacitors of 1000 pF between the coil and balun such that the coil is isolated from ground. The  $^{19}\text{F}$  balun's were placed at  $0^\circ$  and  $90^\circ$ . The  $^1\text{H}$  balun's were placed at  $45^\circ$  and  $135^\circ$ . Figure 5.7 shows a schematic of a dual switch tuned birdcage coil with  $^1\text{H}$  and  $^{19}\text{F}$  channels.

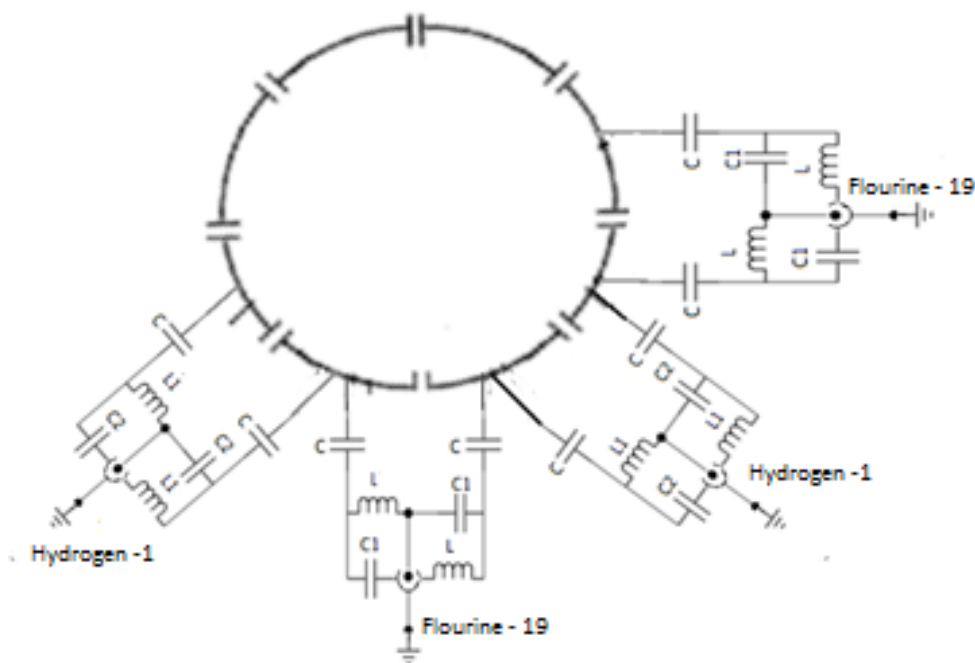


**Figure 5.7 Schematic of dual switch tuned birdcage coil with  $^1\text{H}$  and  $^{19}\text{F}$  channels.**

The performance of the coil was investigated by connecting the two ports to the network analyzer and  $S_{11}$  measurements were performed to check the nuclei at resonance, while checking the performance of  $^1\text{H}$  nuclei the  $^{19}\text{F}$  cables on balun were shorted (as the lattice balun is quarter wavelength, transforming its presence as an infinite high impedance between the coil and the balun when shorting the other end). This was done to keep the

impedance from varying.  $^1\text{H}$  cables were shorted while checking the performance of  $^{19}\text{F}$  channel. Measured impedances from both the channels of  $^1\text{H}$  and  $^{19}\text{F}$  are presented in the Table 5.2. Figure 5.4 and Figure 5.5 shows the S11 response  $^1\text{H}$  and  $^{19}\text{F}$ .

**Table 5.2: Measured impedance for both channels of  $^{19}\text{F}$  and  $^1\text{H}$ .**

Nucleus	Channel -1	Channel -2
$^1\text{H}$	237.3 - j40.5	387.5 - j38
$^{19}\text{F}$	282.7-j41	155-j40

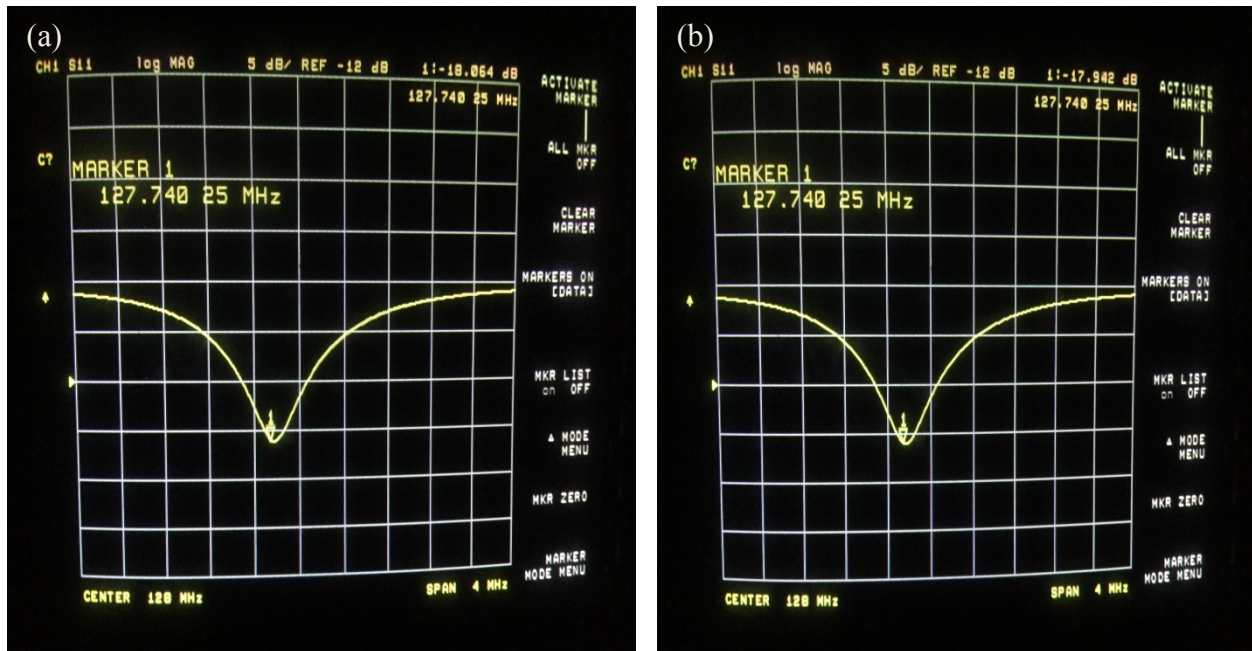


**Figure 5.4 : (a) Channel-1, S11 response for  $^1\text{H}$ .**

**(b) Channel-2, S11 response for  $^1\text{H}$ .**

The S<sub>11</sub> response for channel-1 for  $^1\text{H}$  had a sensitivity of -18 dB and the S<sub>11</sub> response for channel-2 for  $^1\text{H}$  had a sensitivity of -17 dB at 127.74 MHz.

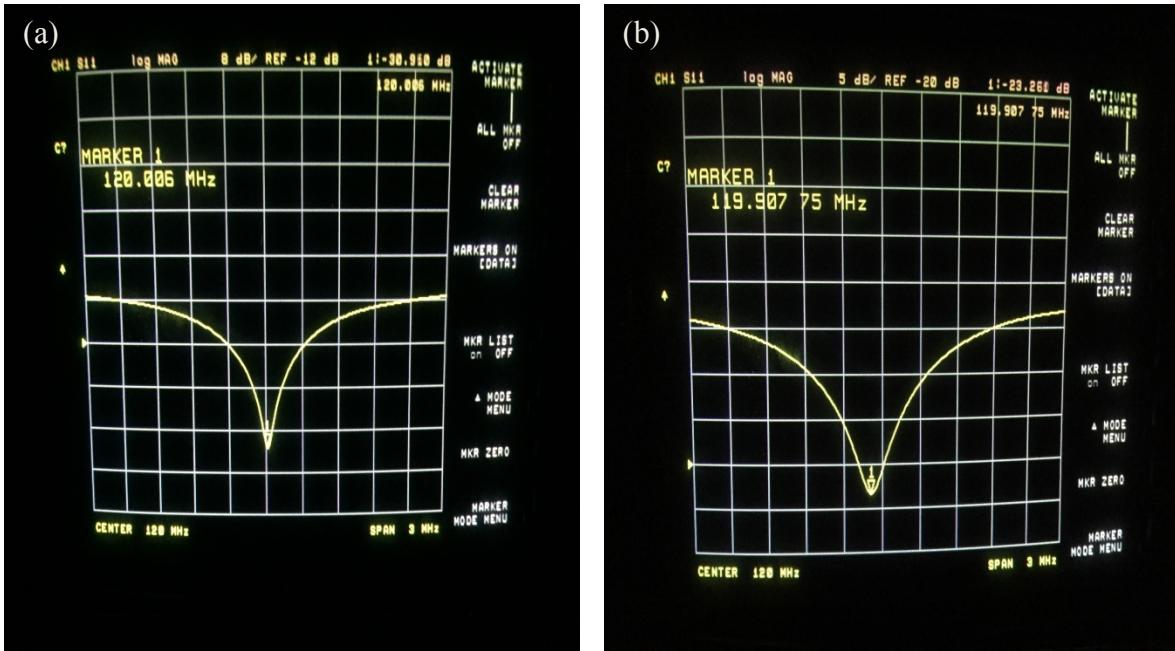


**Figure 5.4 : (a) Channel-1, S<sub>11</sub> response for <sup>19</sup>F.  
(b) Channel-2, S<sub>11</sub> response for <sup>19</sup>F.**

The S<sub>11</sub> response for channel-1 for <sup>19</sup>F had a sensitivity of -30 dB at 120.06 MHz and the S<sub>11</sub> response for channel -2 for <sup>19</sup>F has a sensitivity of -23 dB at 119.9 MHz.

## 5.5 Results

An initial bench test was performed to measure the impedance and the Q factor for both the channels. Loaded Q for <sup>19</sup>F and <sup>1</sup>H was measured as 104 and 85 and unloaded Q for <sup>19</sup>F and <sup>1</sup>H was measured as 118 and 116 (Refer to equation 2-11). The impedance for the <sup>1</sup>H and <sup>19</sup>F channels was measured. After the bench test was performed and it was determined that the coil met the basic requirements, it was placed inside a Philips Achieva 3T scanner to check the response of S<sub>11</sub>. A fine re-tuning was performed as the magnetic field shifts the resonance frequency. MR spectroscopy and imaging scans were performed using a phantom. The coil was calibrated by performing various multi flip angle spectroscopic scans for getting a 90-degree excitation pulse by adjusting the scanner output power.

### 5.5.1 Phantom Spectroscopic Scan Results

A 60ml syringe filled with 11ml of mineral oil is used as a phantom for  $^1\text{H}$ . A 60ml syringe filled with 11ml of sulfur hexafluoride ( $\text{SF}_6$ ) was used as a phantom to test  $^{19}\text{F}$ . While performing the scans these syringes were placed inside a hollow foam cylinder, which was placed in the middle of the coil, such that the sample is at the center of the coil with most homogenous field. Figure 5.5 shows the phantoms used for testing the coil.

The coil was connected to a dual frequency gateway (DFG) for  $^1\text{H}$  phantom test. While performing  $^1\text{H}$  test,  $^{19}\text{F}$  channel cables were shorted such that the balun's of the  $^{19}\text{F}$  are isolated from the coil due to shorting. A home built  $^{19}\text{F}$  quadrature hybrid coupler was used to integrate the coil with the scanner to perform  $^{19}\text{F}$  scans. While  $^{19}\text{F}$  scans are performed  $^1\text{H}$  balun's are shorted isolating it from the coil. A non-selective pulse sequence was performed for a spectroscopic scan using TR of 131 ms and TE of 140 ms. Total power of 392 W was required to calibrate the  $^1\text{H}$  and 288watts of power used to calibrate  $^{19}\text{F}$  channels using the phantoms. Figure 5.6 shows the coil calibration for  $^{19}\text{F}$ .

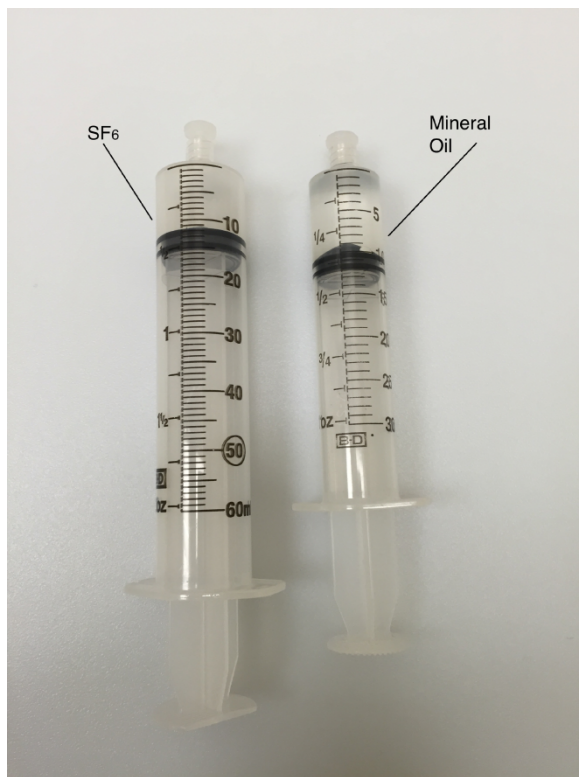


**Figure 5.5: Two syringe phantoms filled with sulfur hexafluoride ( $\text{SF}_6$ ) and mineral oil.**

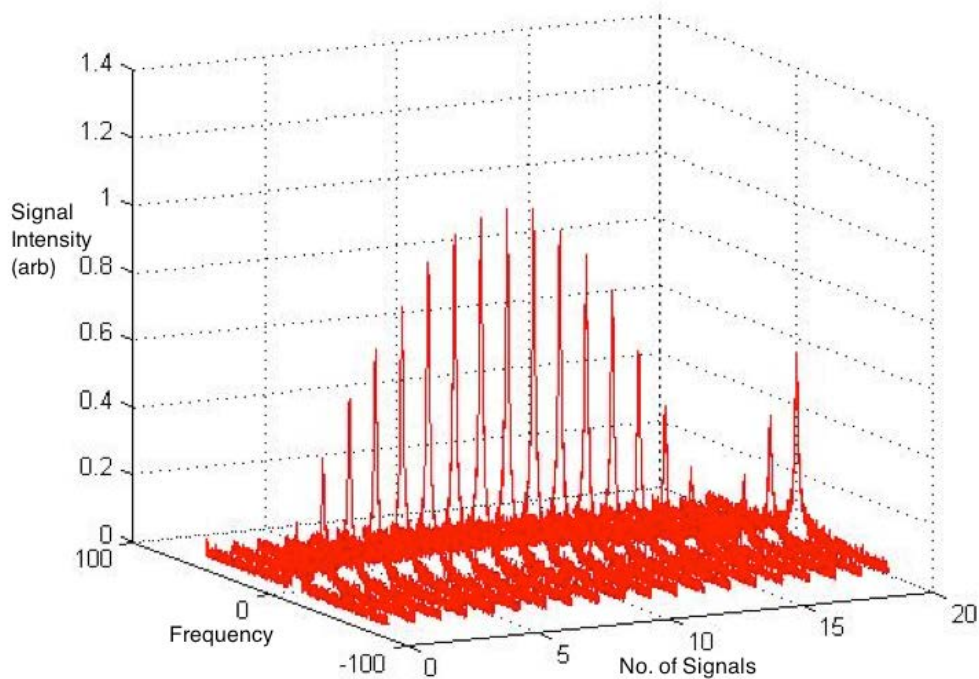


**Figure 5.6: The  $^{19}\text{F}$  coil calibration, showing the signal response as a function of increasing power, where the 90-degree RF pulse yields the highest possible signal.**

The x-axis in Figure 5.6 represents the frequency shift, the y-axis represents the signal intensity in arb values, and the z-axis represents the number of signals where each pulse is excited until the maximum signal achieves a 90-degree excitation pulse. Figure 5.7 shows the spectroscopic results for  $^{19}\text{F}$  using  $\text{SF}_6$ . Figure 5.7 (a) shows the FID signal, which decays as expected due to transverse relaxation. Figure 5.7 (b) shows the Fourier transform of the FID signal, and the center peak indicates the  $^{19}\text{F}$  resonance.

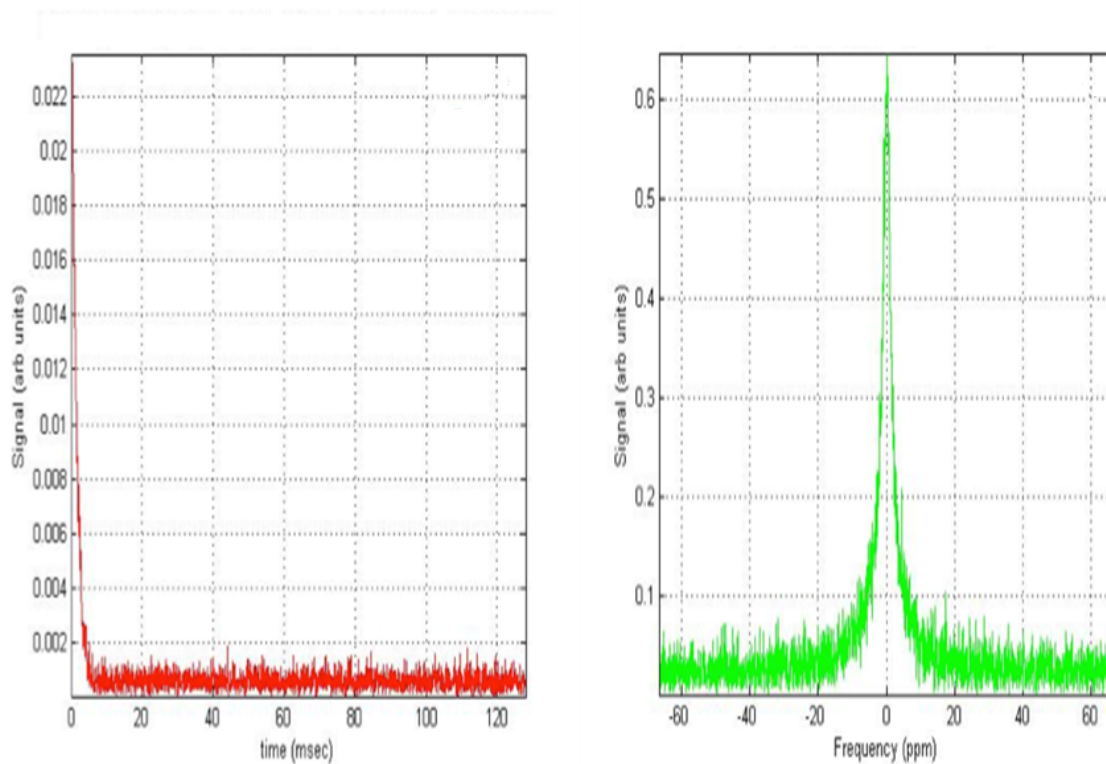


**Figure 5.7 : Spectroscopic results for  $^{19}\text{F}$  using  $\text{SF}_6$ .**

### 5.5.2 Phantom Imaging Scan Results

Phantom scans were performed using the linear birdcage coil for  $^1\text{H}$  and  $^{19}\text{F}$ . A 2D FFE sequence was used to acquire transverse and coronal images. Table 5.3 shows all the different parameters used to achieve  $^1\text{H}$  and  $^{19}\text{F}$  phantom images.

**Table 5.3: Pulse sequence parameters used for  $^1\text{H}$  and  $^{19}\text{F}$  phantom imaging.**

Nucleus	FOV (mm x mm)	TR (ms)	TE (ms)	NSA	$B_1$	Matrix Size	SNR
$^{19}\text{F}$	75 x 75	4	1.19	40	70	64 x 64	23
$^1\text{H}$	50 x 50	100	3.01	4	70	128 x 128	64

The transverse and coronal phantom images for  $^1\text{H}$  and  $^{19}\text{F}$  are shown in Figure 5.8.

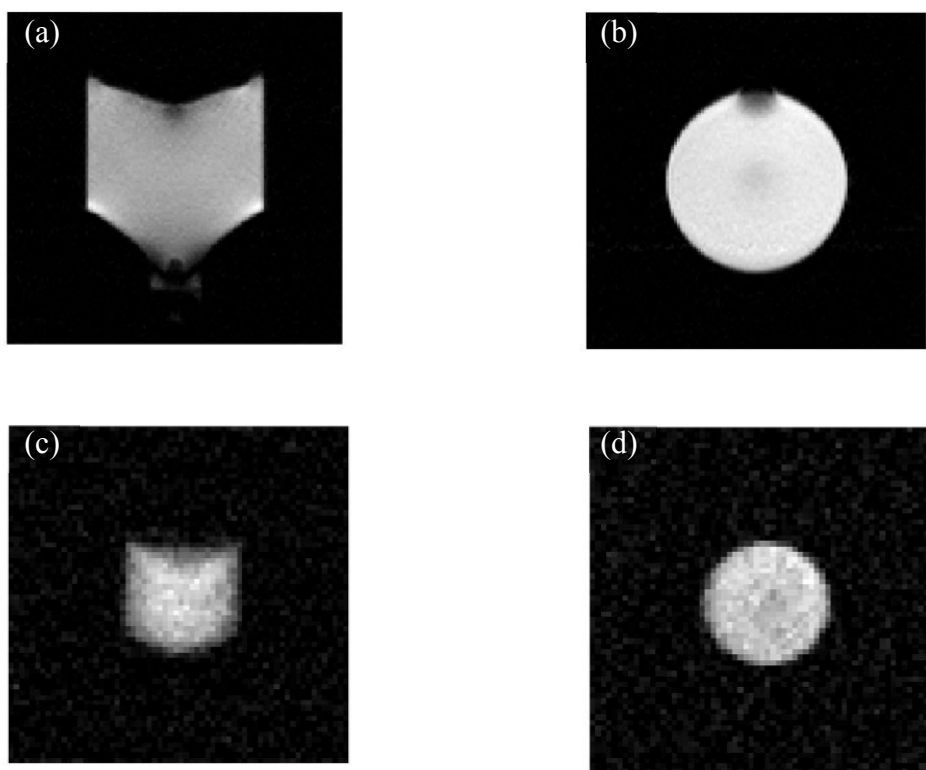


**Figure 5.8 :** (a)  $^1\text{H}$  Coronal image with Mineral oil.

(b)  $^1\text{H}$  Transverse image with Mineral oil.

(c)  $^{19}\text{F}$  Coronal image with  $\text{SF}_6$ .

(d)  $^{19}\text{F}$  Transverse image with  $\text{SF}_6$ .

### 5.5.3 $B_1$ Field Mapping and Field Homogeneity

As discussed in 4.4.3,  $B_1$  mapping and  $B_1$  field homogeneity was performed to check the performance of the coil.  $B_1$  field can be measured and mapped using several NMR techniques. In this study,  $^1\text{H}$   $B_1$  field mapping was performed using dual-TR method using a 60 mL syringe of mineral oil, and  $^{19}\text{F}$   $B_1$  field mapping was performed using dual angle method (DAM) with a 60 mL syringe of sulfur hexafluoride ( $\text{SF}_6$ ).  $B_1$  mapping was performed by selecting an area of 18x18mm with 30mm slice thickness at the center of the coil. Mean value and standard deviations for  $^{19}\text{F}$  was calculated as  $0.70 \pm 0.13$ . The quadrature coil has slightly worst field homogeneity compared to the linear dual

tuned coil, this might be due to the presence of PIN diodes on the coil. Figure 5.9.1 and Figure 5.9.2 shows the normalized  $B_1$  plot of the birdcage coil,  $B_1$  histogram and  $B_1$  field graph at the center of the coil using sulfur hexafluoride ( $\text{SF}_6$ )  $^{19}\text{F}$ .

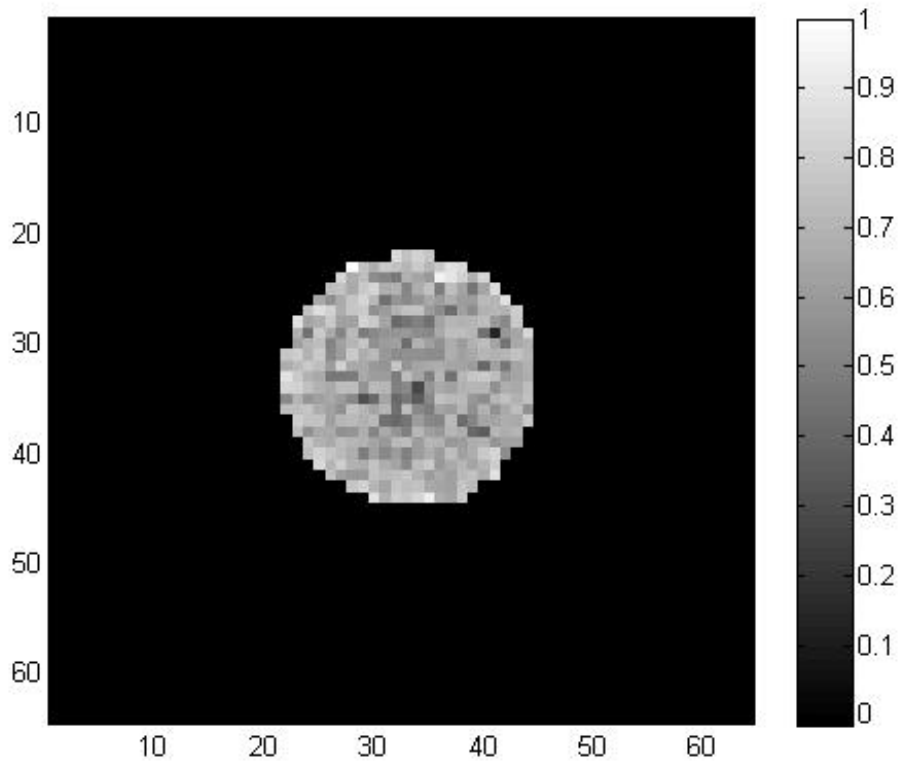


**Figure 5.9.1 :  $B_1$  field map for  $^{19}\text{F}$ .**

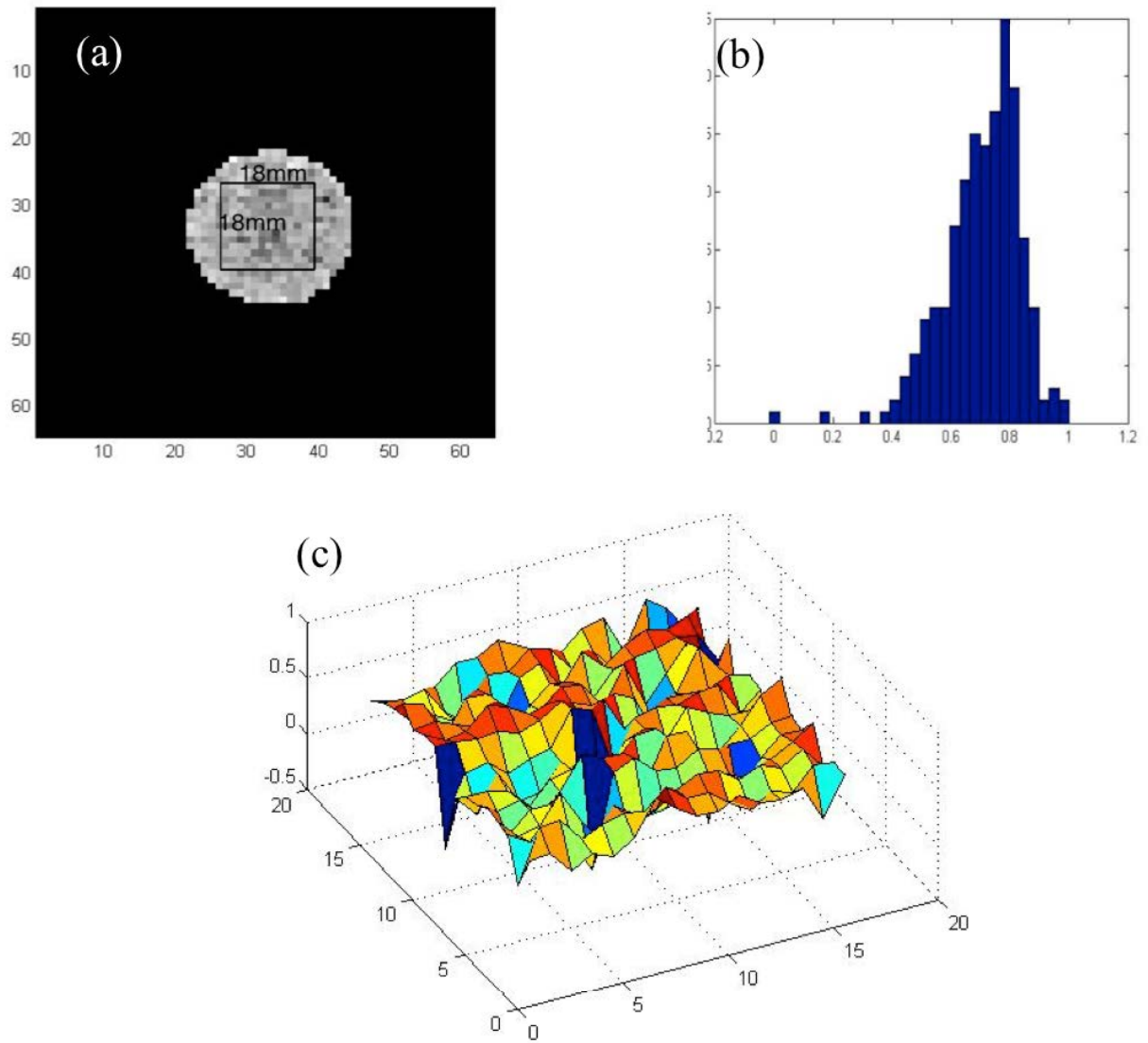


**Figure 5.9.2 : (a)  $B_1$  map with the area of 18x18x30mm of  $^{19}\text{F}$ .**

**(b) Histogram of the  $B_1$  of the coil generated by (a).**

**(c)  $B_1$  field graph for  $^{19}\text{F}$ .**

The  $^1\text{H}$   $B_1$  mapping scan was performed on a slice thickness of 20 mm at the center of the coil with a  $\text{TR}_1$  of 200 ms and a  $\text{TR}_2$  of 1 s. Figure 5.9.3 shows the normalized  $B_1$  of the birdcage coil.

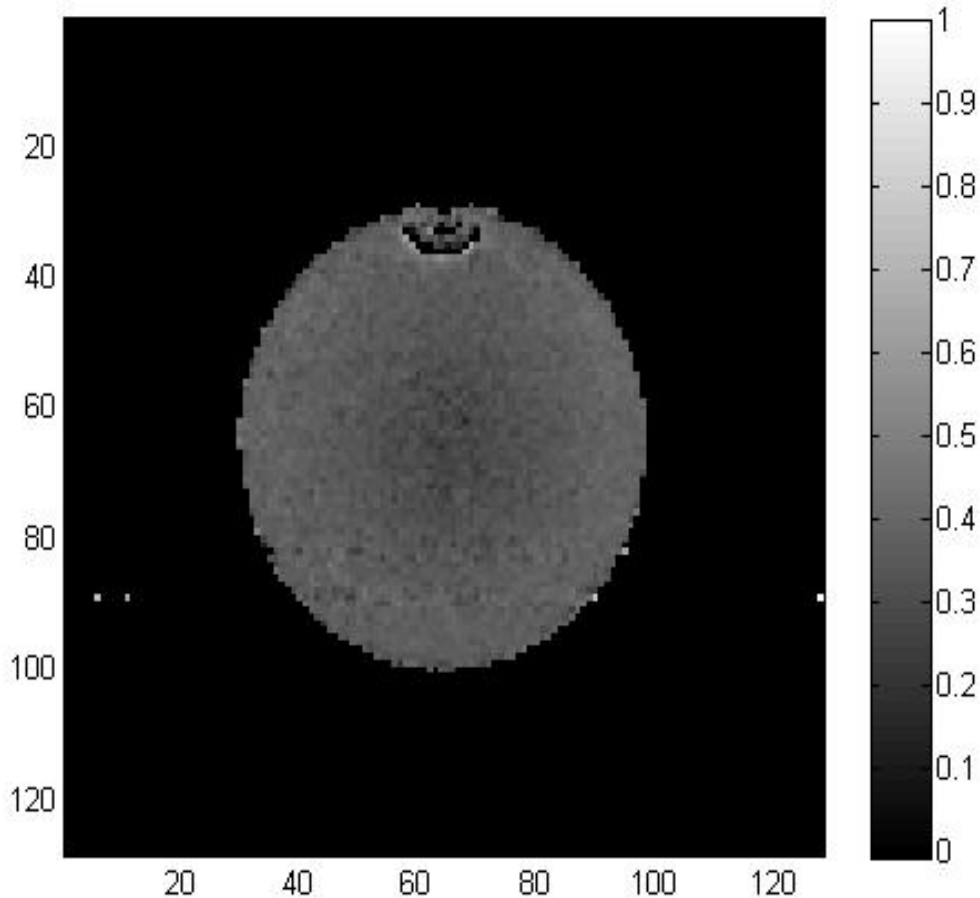


**Figure 5.9.3 : Normalized  $B_1$  map for  $^1\text{H}$ .**

An area of 16 x 16 mm with a slice thickness of 30 mm was selected at the center of the coil to generate the  $B_1$  histogram and  $B_1$  map at the center of the coil. The mean value and standard deviations for  $^1\text{H}$  was calculated as  $0.72 \pm 0.074$ . Figure 5.9.4 represents  $B_1$  histogram and  $B_1$  map. The quadrature coil has slightly worst field homogeneity compared to the linear dual tuned coil, this might be due to the presence of PIN diodes on the coil.

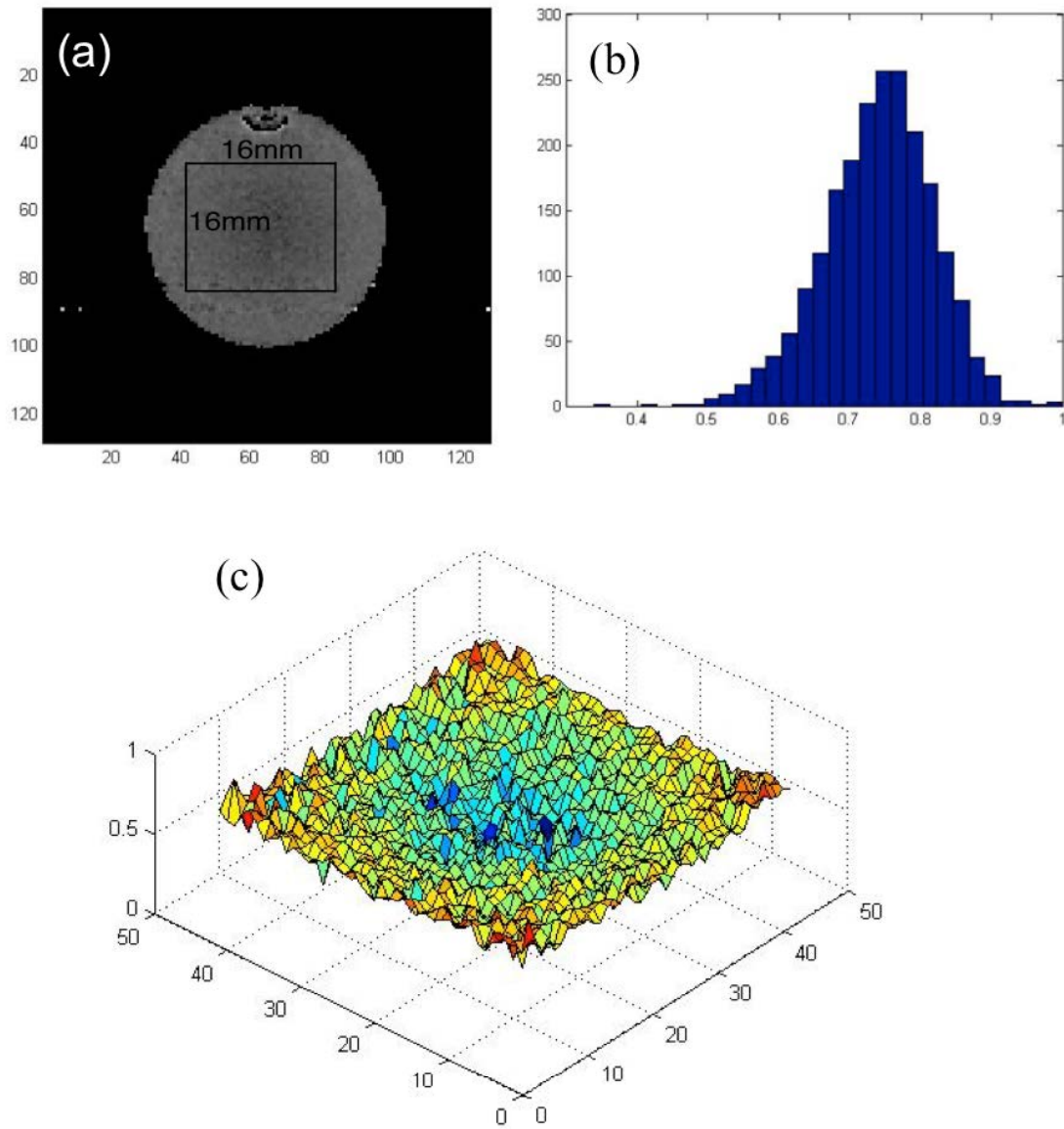


**Figure 5.9.4 : (a)  $B_1$  map with the area of 16x16x30mm of  $^1\text{H}$ .  
 (b) Histogram of the  $B_1$  of the coil generated by (a).  
 (c)  $B_1$  field graph for  $^1\text{H}$ .**

### 5.5.4 Comparison Between Linear Dual Tuned and Quadrature Dual Tuned

For comparing the linear dual tuned and quadrature dual tuned coils, same phantoms and scan parameters are used. Table 5.4 shows the obtained SNR (From Section 2.10) values for linear and quadrature.

**Table 5.4: SNR obtained from linear and quadrature dual tuned coils**

Frequency	$^1\text{H}$	$^{19}\text{F}$
Linear dual tuned coil	30.2	30.1
Quadrature dual tuned coil	63.9	23.8

For comparison of SNR, coronal phantom images from linear dual tuned  $^1\text{H}$  coil and coronal images of  $^1\text{H}$  quadrature dual tuned coils are used. Figure 5.10 represents the coronal images of  $^1\text{H}$  obtained from linear and quadrature dual tuned coils.

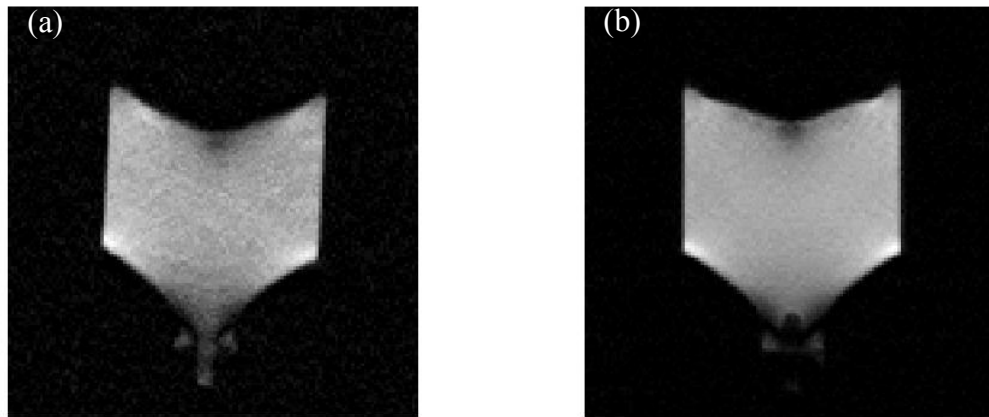


**Figure 5.10: (a) Coronal image of  $^1\text{H}$  from linear dual tuned coil.**

**(b) Coronal image of  $^1\text{H}$  from quadrature dual tuned coil.**

According to the theory described above, quadrature coils should achieve an SNR that is a factor of  $\sqrt{2}$  higher than linear coils. From the Table 5.4, it is evident that the quadrature  $^1\text{H}$  coils has an SNR twice than the linear showing satisfactory results.

The SNR for the  $^{19}\text{F}$  linear and quadrature dual tuned coils were also compared. Coronal images were used for comparison of  $^{19}\text{F}$  nuclei. Figure 5.11 represents the coronal images of  $^{19}\text{F}$  obtained from linear and quadrature dual tuned coils.

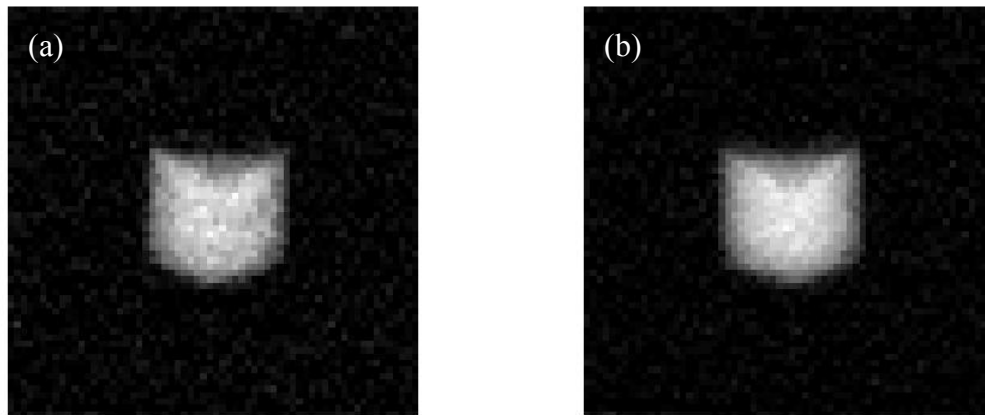


**Figure 5.11: (a) Coronal image of  $^1\text{H}$  from quadrature dual tuned coil.  
(b) Coronal image of  $^1\text{H}$  from linear dual tuned coil.**

From the Table 5.4 it is evident that the linear dual tuned coil has higher  $^{19}\text{F}$  SNR than quadrature dual tuned coil, which was an unexpected result. Further investigating SNR for the coil, the noise in the quadrature coil was found to be higher compared to linear coil. Higher noise levels will naturally lead to a lower SNR. The two main factors resulted that introduced noise were diodes and the other one was the DC power supply line passing through the center of the MRI bore introducing noise.

## 5.6 Discussion

In this chapter, a quadrature dual tuned coil for  $^1\text{H}$  and  $^{19}\text{F}$  was constructed. The coil exhibited satisfactory results. The important point from this chapter shows that active decoupling of  $^1\text{H}$  and  $^{19}\text{F}$  can be achieved by using PIN diodes. Bench test results, phantom results and  $B_1$  field mapping results were presented.

$B_1$  field mapping shows the homogeneity of the coil and the  $B_1$  field mapping shows very homogeneous field is at the center of the coil. For the  $^1\text{H}$  side the SNR was demonstrated to be higher when compared to linear. But  $^{19}\text{F}$  showed a lower SNR than expected due to higher noise introduced by the diodes and the DC supply cable.

## Chapter 6

### Discussions

#### 6.1 Summary

The goal of this thesis was to develop an optimized  $^1\text{H}/^{19}\text{F}$  dual tuned coil for rodent lung imaging and disease model investigation. In order to determine the optimal decoupling approach for frequencies that are close to each other, three RF coils were built: geometrically decoupled coils, a linear dual-tuned birdcage, and a quadrature dual-tuned birdcage.

Chapter 3 discussed geometrical decoupling using the coil inside coil approach for frequencies that are close to each other (i.e.  $^1\text{H}$  and  $^{19}\text{F}$ ). This technique was not successful, because the  $^{19}\text{F}$  frequency shifted away from resonance by 1.5 MHz and  $^1\text{H}$  frequency shifted away from resonance by 3.5 MHz, due to the strong coupling effect. The linear dual-tuned coil for  $^{19}\text{F}$  and  $^1\text{H}$  showed better results by overcoming geometrical decoupling as presented in Chapter 4. The  $B_1$  field mapping, phantom, and rat imaging demonstrated that the coil was working properly. In the field of MRI, there is a demand for high quality images, and further improvements can potentially be made through the development of quadrature coil designs.

Later in Chapter 5, a quadrature switch-tuned coil was built with the goal of achieving a higher SNR by a factor of  $\sqrt{2}$ . A total of 4 switching circuits were used to switch from the  $^1\text{H}$  frequency to the  $^{19}\text{F}$  frequency using PIN diodes. This chapter summarized that effective switching between  $^1\text{H}$  and  $^{19}\text{F}$  frequencies can be achieved.  $^1\text{H}$  phantom imaging demonstrated an increase of SNR by more than a factor of  $\sqrt{2}$ , however, unexpected results for  $^{19}\text{F}$  were observed due to the noise introduced by the PIN diodes and DC power supply cable. This technique demonstrates that decoupling for two close frequencies can be achieved by active switching.

## 6.2 Future Work

This thesis demonstrated that decoupling using PIN diodes introduced high noise levels, which resulted in a decreased SNR. One major factor that might help to achieve higher SNR would be extending the DC power cables, such that the cables are outside the bore. In the future, *in vivo* animal lung imaging will be performed to validate the quadrature switch-tuned coil.

This coil design will be used in future studies involving animal models of respiratory diseases. For example, a model of elastase-induced emphysema has been studied in rat lungs using hyperpolarized  $^3\text{He}$  MRI. The results of this study demonstrate that ventilation function was impaired in rats that had been instilled with elastase <sup>[50]</sup>. Hyperpolarized  $^3\text{He}$  MRI has also been used to study models of pulmonary inflammation in rat lungs using instilled lipopolysaccharide (LPS) <sup>[51]</sup>. The results of these studies are promising, since  $^3\text{He}$  imaging can detect functional changes in the lungs due to the instilled agents. As discussed in Chapter 1, hyperpolarized gas MRI is a very expensive technique, and therefore similar animal studies will need to be performed using inert fluorinated gas MRI in order to help translate this developing technique to routine clinical diagnostic imaging.

This thesis focused on the development of birdcage coils for animal imaging. In general, volume coils have advantages over surface coils in terms of  $B_1$  homogeneity. The small animal switch-tuned coil that was developed in this thesis showed satisfactory results which can be translated to the development of a human lung sized birdcage coil. On the other hand, when scaling up to human imaging, surface coils are extensively used, which result in a better SNR. Since surface coils are inherently inhomogeneous, human coils often use an array of surface coils in order to ensure good coverage of the anatomy of interest. Future developments in inert fluorinated gas MRI will make use of these concepts to develop optimized dual-tuned  $^{19}\text{F}$ - $^1\text{H}$  coil designs for human lung imaging.

### 6.3 Conclusions

From this thesis, it was determined that linear dual tuned and quadrature dual tuned birdcage coil can be constructed for resonant frequencies that are close to each other. From this we can also conclude that dual tuned quadrature coils can be constructed using PIN diodes for a cheaper price for small animal imaging.. In the past, single tuned coils for imaging have been developed, and image registration was a huge limitation because two independent coils need to be used to image different nuclei within the same subject. Image registration is needed to combine  $^{19}\text{F}$  ventilation images with their conventional  $^1\text{H}$  analogues. The development of dual-tuned  $^{19}\text{F}$ - $^1\text{H}$  RF coils greatly facilitate image registration, as well as to provide the opportunity to acquire both structural and functional information from the lungs using inert fluorinated gas MRI.

For the coil inside coil technique, larger diameters of the coil can be used to tune them to be on resonance and also checking for filling factor. But this technique will only limit to a linear mode and the B1 field profile for the  $^1\text{H}$  will be different when compared to  $^{19}\text{F}$  because of the increase in size of the  $^1\text{H}$  coil.

The quadrature dual switch tuned coil was initially tuned to  $^1\text{H}$  and active switching was performed to switch it to  $^{19}\text{F}$ . To also enhance the  $^{19}\text{F}$  signal and achieve higher SNR the coil can be initially tuned to  $^{19}\text{F}$  and active switching can be performed to switch it to  $^1\text{H}$  as  $^1\text{H}$  SNR is not as important as  $^{19}\text{F}$ .

<b>Type of Coil Design</b>	<b>Pros</b>	<b>Cons</b>	<b>Next steps</b>
<b>A Linear <math>^{19}\text{F}</math> - <math>^1\text{H}</math> Double Birdcage Coil (Coil Inside Coil)</b>	<ul style="list-style-type: none"> <li>• Simple Design</li> <li>• Pin diodes are not required</li> </ul>	<ul style="list-style-type: none"> <li>• Works only on a linear mode</li> <li>• Coil had a poor isolation</li> <li>• Tuning the coil to resonance wasn't achieved</li> </ul>	<ul style="list-style-type: none"> <li>• <math>^1\text{H}</math> coil with a bigger coil diameter can be used to tune the coil to resonance</li> </ul>
<b>A <math>^{19}\text{F}</math>-<math>^1\text{H}</math> Linear Dual Tuned Birdcage Coil</b>	<ul style="list-style-type: none"> <li>• Simple design</li> <li>• B1 fields for both nuclei will be same</li> <li>• Pin diodes are not required</li> </ul>	<ul style="list-style-type: none"> <li>• The coil works on a linear mode</li> <li>• Requires more power to calibrate the coil.</li> <li>• Adverse tissue heating due to more power required for calibration</li> </ul>	<ul style="list-style-type: none"> <li>• Achieved SNR was satisfactory</li> <li>• Build quadrature coils as they give higher SNR by a factor of root two.</li> </ul>
<b>A <math>^{19}\text{F}</math>-<math>^1\text{H}</math> Quadrature Dual Switch Tuned Birdcage Coil</b>	<ul style="list-style-type: none"> <li>• Gives higher SNR and requires less power to operate.</li> <li>• This can be done for both the nuclei</li> <li>• B1 fields for both nuclei will be same</li> </ul>	<ul style="list-style-type: none"> <li>• Complex Design</li> <li>• Noise introduced by PIN diodes resulting in lower SNR</li> <li>• Lower SNR when compared to linear coil</li> <li>• DC cables were passing through the bore introducing more noise</li> </ul>	<ul style="list-style-type: none"> <li>• Needs an alternative design such that the DC cables are outside the bore</li> <li>• Use lower resistance PIN diodes</li> </ul>

From the quadrature dual, the coil was initially tuned to  $^1\text{H}$  and by adding the switching circuits the coil was switched to  $^{19}\text{F}$  as a result lower SNR was achieved for  $^{19}\text{F}$  compared to linear dual tuned coil. A better coil can be designed to get higher SNR but tuning the coil to  $^{19}\text{F}$  initially and then switched to  $^1\text{H}$  by adding switching circuits as  $^1\text{H}$  SNR is not as important as  $^{19}\text{F}$ .

## References

- [1]. E. M. Purcell, H. C. Torrey, and R. V. Pound. Resonance absorption by nuclear magnetic moments in a solid. *Physical Review*, 69:37–38, 1946.
- [2]. F. Bloch. Nuclear induction. *Physical Review*, 70:460–474, 1946.
- [3]. P. C. Lauterbur. Image formation by induced local interactions: Examples employing nuclear magnetic resonance. *Nature*, 242:190–191, 1973.
- [4]. P. Mansfield and P. K. Grannell. NMR ‘diffraction’ in solids? *Journal of Physics C: Solid State Physics*, 6:L422–426, 1973.
- [5]. Albert, M.S. et al. (1994) Biological magnetic resonance imaging using laser polarized  $^{129}\text{Xe}$ . *Nature*, 370, 199-201.
- [6]. Heidelberg E, Lauterbur PC. Gas Phase  $^{19}\text{F}$ -NMR Zeugmatography: A New Approach to Lung Ventilation Imaging. Proc 1st Annual Meeting Society of Magnetic Resonance in Medicine, 1982; 70- 71.
- [7]. Kuethe DO, Behr VC, Begay S. Volume of rat lungs measured throughout the respiratory cycle using  $^{19}\text{F}$  NMR of the inert gas  $\text{SF}_6$ . *Magn Reson Med*. 2002; 48(3):547-9.
- [8]. Couch MJ, Ball IK, Li T, Fox MS, Littlefield SL, Biman B, Albert MS. Pulmonary ultrashort echo time  $^{19}\text{F}$  MR imaging with inhaled fluorinated gas mixtures in healthy volunteers: feasibility. *Radiology*. 2013; 269: 903-909.
- [9]. Halaweish AF, Moon RE, Foster WM, Soher BJ, McAdams HP, MacFall JR, Ainslie MD, MacIntyre NR, Charles HC. Perfluoropropane gas as a magnetic resonance lung imaging contrast agent in humans. *Chest*. 2013; 144: 1300-1310.
- [10]. Kuethe DO, Caprihan A, Fukushima E, Waggoner RA. Imaging lungs using inert fluorinated gases. *Magn Reson Med*. 1998; 39(1):85-8.
- [11]. Schreiber WG, Eberle B, Laukemper-Ostendorf S, Markstaller K, Weiler N, Scholz A, et al. Dynamic  $^{19}\text{F}$ -MRI of pulmonary ventilation using sulfur hexafluoride ( $\text{SF}_6$ ) gas. *Magn*

*Reson Med.* 2001;45(4):605-13.

- [12]. Kuethe DO, Behr VC, Begay S. Volume of rat lungs measured throughout the respiratory cycle using  $^{19}\text{F}$  NMR of the inert gas  $\text{SF}_6$ . *Magn Reson Med.* 2002; 48(3):547-9.
- [13]. Adolphi NL, Kuethe DO. Quantitative mapping of ventilation-perfusion ratios in lungs by  $^{19}\text{F}$  MR imaging of T1 of inert fluorinated gases. *Magn Reson Med.* 2008; 59(4):739-46.
- [14]. Aktham Asfour. Design and development of a new dedicated RF sensor for the MRI of rat brain. *J. Biomedical Science and Engineering*, 2010, 3, 167-180
- [15]. Tao Li, RF Coils Design for Small Animal MRI Lung Imaging at 3T Using Hyperpolarized  $^{129}\text{Xe}$  and Inert Fluorinated Gases. Lakehead University Master's Thesis.
- [16]. Lingzhi Hu et al., A Generalized Strategy for Designing  $^{19}\text{F}/^1\text{H}$  Dual-Frequency MRI Coil for Small Animal Imaging at 4.7 Tesla. *Journal of Magnetic Resonance Imaging* 34:245–252 (2011).
- [17]. Dennis W.J. Klomp et al., Optimization of Localized  $^{19}\text{F}$  Magnetic Resonance Spectroscopy for the Detection of Fluorinated Drugs in the Human Liver. *Magnetic Resonance in Medicine* 50:303–308 (2003).
- [18]. Ouriadov AV, Fox MS, Couch MJ, Li T, Ball IK, Albert MS. In vivo regional ventilation mapping using fluorinated gas MRI with an x-centric FGRE method. *Magn Reson Med* 2014:DOI:10.1002/mrm.25406
- [19]. Y. Otake. In-vivo  $^{19}\text{F}$  Imaging of 5-Fluorouracil and its Metabolites in Rat by Two-Element Phased-Array Coil. International Society for Magnetic Resonance in Medicine conference 2011
- [20]. John Cavanagh, Protein NMR Spectroscopy: Principles and Practice
- [21]. Stephen G. Odaibo et al., A Quantum Mechanical Review of Magnetic Resonance Imaging textbook.
- [22]. Ray H. Hashemi et al., MRI: The Basics textbook.
- [23]. E. Mark Haacke, Magnetic Resonance Imaging Physical principles and sequence design.

- [24]. Donald B. Twieg. The k-trajectory formulation of the NMR imaging process with applications in analysis and synthesis of imaging methods. *Medical Physics* 10, 610 (1983); doi: 10.1118/1.595331.
- [25]. C. E. Hayes et al., “An efficient, highly homogenous radiofrequency coil for whole-body NMR imaging at 1.5 T”, *Journal of Magnetic Resonance*, (63): 622-628; 1985.
- [26]. C.I.Chin et al., “Circular and Elliptical Birdcage Coil Design for Magnetic Resonance Imaging”, *IEEE 10.1109/NEBC.1998.664866*
- [27]. Grover FW. Inductance calculation. New York: VanNostrand; 1946.
- [28]. Feynman et al., Lectures on physics volume -2 text book
- [29]. D.I.Hoult., “The principal of reciprocity in signal strength calculations: A mathematical Guide”, *Conc. Magn. Reson. 12(4) :173-178,2000*.
- [30]. Nishimura DG. Principles of Magnetic Resonance Imaging. lulu.com; 2010.
- [31]. J. Mispelter, M. Lupu and A. Briguet, “NMR Probeheads for Biophysical and Biomedical Experiments: Theoretical Experiments and Practical Guidelines.” *Imperial Collage press 2006*.
- [32]. Seunghoon Ha. A PIN diode controlled dual-tuned MRI RF coil and phased array for multi nuclear imaging. *Phys. Med. Biol. 55 (2010) 2589–2600*.
- [33]. Dustin D et al., “Practical Exercises for Learning to Construct NMR/MRI Probe Circuits”, *Concepts in Magnetic Resonance Part A, Vol. 40A(1) 1-13(2012)*.
- [34]. K. OCEGUEDA et al., “A Simple Method to Calculate the Signal-to Noise Ratio of a Circular Shape Coil for MRI Concepts”, *Magn. Reso. Part A 28(A) :422-426,2006*.
- [35]. K. OCEGUEDA et al., “A Simple Method to Calculate the Signal-to Noise Ratio of a Circular Shape Coil for MRI Concepts”, *Magn. Reso. Part A 28(A) :422-426,2006*.
- [36]. Heeseung Lim, Kundan Thind. Construction and Evaluation of a Switch-Tuned  $^{13}\text{C}$  -  $^1\text{H}$  Birdcage Radiofrequency Coil for Imaging the Metabolism of Hyperpolarized  $^{13}\text{C}$ -Enriched Compounds. *Journal of Magnetic Resonance Imaging* 00:00–00 (2014).
- [37]. J-X. Wang, E. B. Boskamp. An Efficient Switched Double-Frequency Birdcage Coil for

- $^3\text{He}$  and  $^1\text{H}$  Imaging. International Society for Magnetic Resonance in Medicine conference 2008.
- [38]. M. Alecci et al., Practical design of a 4 Tesla double-tuned RF surface coil for interleaved  $^1\text{H}$  and  $^{23}\text{Na}$  MRI of rat brain. *Journal of Magnetic Resonance* 181 (2006) 203–211.
- [39]. Yiyi Ji et al., Eight-channel transceiver RF coil array tailored for  $^1\text{H}/^{19}\text{F}$  MR of the human knee and fluorinated drugs at 7.0 T. *NMR in Biomedicine* 2015; 28: 726–737
- [40]. Jesus Ruiz-cabello, “Diffusion-weighted  $^{19}\text{F}$ -MRI of lung periphery: Influence of pressure and air– $\text{SF}_6$  composition on apparent diffusion coefficients”, *Respiratory Physiology & Neurobiology* 148 (2005) 43–56.
- [41]. G. X. Shen et al., “Dual-frequency, dual-quadrature, birdcage RF coil design with identical  $B_1$  pattern for sodium and proton imaging of the human brain at 1.5 T”, *Magnetic Resonance in Medicine*, (38): 717- 725, 1997.
- [42]. J.R. Fitzsimmons et al. “Double Resonant quadrature birdcage”, *Magnetic Resonance in Medicine (MRM)*, (30): 107-114, 1993.
- [43]. T. Lanz et al., “Double tuned  $^{23}\text{Na}$   $^1\text{H}$  nuclear magnetic resonance birdcage for application on mice in vivo”, *Review of Scientific Instruments*, 72(5): 2508-2510; 2001.
- [44]. C. L. Chin et al., “BirdcageBuilder: Design of specified-geometry birdcage coils with desired current pattern and resonance frequency”, *Concepts in Magnetic Resonance*, 15(2): 156-163, 2002.
- [45]. Morrell GR. A phase-sensitive method of flip angle mapping. *Magn Reson Med* 2008; 60:889-894.
- [46]. Sacolick LI, Wiesinger F, Hancu I, and Vogel MW.  $B_1$  mapping by Bloch-Siegert shift. *Magn Reson Med* 2010; 63:1315-1322.
- [47]. Insko E and Bolinger L. Mapping of the radiofrequency field. *J Magn Reson A* 1993; 103:82-85.
- [48]. Hornak JP, Szumowski J, and Bryant RG. Magnetic field mapping. *Magn Reson Med* 1988; 6:158-163.

- [49]. Pauly J, Nishimura D, and Macovski A. A k-space analysis of small-tip-angle excitation. *J Magn Reson* 1989; 81:43-56.
- [50]. Emami k et al., Early changes of lung function and structure in an elastase model of emphysema--a hyperpolarized  $^3\text{He}$  MRI study. Journal of applied Physics 2008 Mar;104(3):773-86.
- [51]. Thomas et al., Ventilation Defects Observed with Hyperpolarized  $^3\text{He}$  Magnetic Resonance Imaging in a Mouse Model of Acute Lung Injury. *Am J Respir Cell Mol Biol.* 2011 May; 44(5): 648–654
- [52]. Dregely et al., 32-Channel Phased-Array Receive with Asymmetric Birdcage Transmit Coil for Hyperpolarized Xenon-129 Lung Imaging. *Magnetic Resonance in Imaging* 2013 Aug;70(2):576-83
- [53]. Rao et al., RF Instrumentation for Same-Breath Triple Nuclear Lung MR Imaging of  $^1\text{H}$  and Hyperpolarized  $^3\text{He}$  and  $^{129}\text{Xe}$  at 1.5T. *Magnetic Resonance in Medicine* 00:00–00 (2015).
- [54]. Rinck PA, Petersen SB, Lauterbur PC. NMR-Imaging von fluorhaltigen Substanzen. 19Fluor-Ventilations- und -Perfusionsdarstellungen. *Fortschr Röntgenstr.* 1984; 140: 239-243.
- [55]. J-X Wang. An Efficient Switched Double-Frequency Birdcage Coil for  $^3\text{He}$  and  $^1\text{H}$  Imaging , *Proceedings of the 16th Annual Meeting ISMRM; ISMRM, 2008*
- [56]. M.C. Leifer, “Resonant modes of the birdcage coil”, *Journal of Magnetic Resonance*, vol. 124,(no.1), pp. 51-60, 1997.
- [57]. N. Chen, D. I. Hoult, and V. I. Sank. Quadrature detection coils – a further improvement in sensitivity. *J. Magn. Reson.*, 54:324-327, 1983.
- [58]. R. K. Mongia, I.J. Bahl, P. Bhartia, J. Hong. *RF and Microwave Coupled-Line Circuits.* Artech House, Incorporated, 2007.
- [59]. Oh C, Hilal S, Cho Z, and Mun I. Radio frequency field intensity mapping using a composite spin-echo sequence. *Magn Reson Imaging* 1990; 8:21-25.
- [60]. R. Rath, “Design and performance of a double-tuned birdcage coil”, *Journal of Magnetic*

*Resonance*, (86): 488-495; 1990.

- [61]. Pablo J. Prado; Bruce J. Balcom; Igor V. Mastikhin; Albert R. Cross; Robin L. Armstrong; Alan Logan. Magnetic Resonance Imaging of Gases: A Single-Point Ramped Imaging with T1 Enhancement (SPRITE) Study. *J. Magn. Reson.*, (137): 324-332, 1999.
- [62]. Jacob RE, Chang YV, Choong CK, Bierhals A, Hu DZ, Yablonskiy DA, Woods JC, Gierada DS, Conradi MS. 19F MR imaging of ventilation and diffusion in excised lungs. *Magn Reson Med* 2005; 54:577–585.
- [63]. Chih-Liang Chin, BirdcageBuilder: Design of Specified-Geometry Birdcage Coils with Desired Current Pattern and Resonant Frequency. *Concepts in Magnetic Resonance (Magnetic Resonance Engineering)*, Vol.15(2) 156–163 (2002).
- [64]. J. Haase. Double Resonance Probes for Close Frequencies. *JOURNAL OF MAGNETIC RESONANCE* 135, 273–279 (1998).

## Appendix: Animal Care Committee Approval



Office of Research

(807) 343-8283  
(807) 346-7749

### MEMORANDUM

Date: July 8, 2013

To: Dr. Mitchell Albert, Dr. Matthew Fox, TBRR

From: Dr. Brian McLaren, Acting Chair, Animal Care Committee

Subject: Approval for AUP #04 2013 / Romeo #1463130

Thank you for providing the Lakehead University Animal Care Committee the amendments requested at the March 19, 2013 ACC meeting for your research study titled, "Magnetic Resonance Imaging of Dissolved and Gas Phase Xenon in Rat Lungs".

The project has received positive peer review with no requested amendments from reviewers.

On behalf of the Committee, I am pleased to inform you that the project has been **approved**.

If any amendments are required throughout the life of the project, please complete a Protocol Modification Form for submission to the ACC. Annually the ACC will request you renew your protocol as needed.

Once your project has been completed, please inform Sue Wright ([swright@lakeheadu.ca](mailto:swright@lakeheadu.ca)) so that your file can be closed.

Animal Care Committee forms are available through the Romeo Research Portal at:

<http://romeo.lakeheadu.ca>

Best wishes for success with your project.

Sincerely,

A handwritten signature in black ink that reads "Brian McLaren".

Dr. B. McLaren  
Acting Chair, Animal Care Committee

/scw